UNIVERSITY OF ALBERTA

MODELING AND FABRICATION OF RARE-EARTH-DOPED INTEGRATED OPTICAL WAVEGUIDE AMPLIFIERS

BY

Madhu Krishnaswamy ©

A thesis submitted to the faculty of Graduate Studies and Research in partial fulfillment of the requirements for the degree of **Doctor of Philosophy**

DEPARTMENT OF ELECTRICAL ENGINEERING

EDMONTON, ALBERTA, CANADA

SPRING, 1998

National Library
of Canada

Acquisitions and
Bibliographic Services

395 Wellington Street
Ottawa ON K1A 0N4
Canada

Bibliothèque nationale
du Canada

Acquisitions et
services bibliographiques

395, rue Wellington
Ottawa ON K1A 0N4
Canada

Your file Votre référence

Our file Notre référence

The author has granted a non-exclusive licence allowing the National Library of Canada to reproduce, loan, distribute or sell copies of this thesis in microform, paper or electronic formats.

L'auteur a accordé une licence non exclusive permettant à la Bibliothèque nationale du Canada de reproduire, prêter, distribuer ou vendre des copies de cette thèse sous la forme de microfiche/film, de reproduction sur papier ou sur format électronique.

The author retains ownership of the copyright in this thesis. Neither the thesis nor substantial extracts from it may be printed or otherwise reproduced without the author's permission.

L'auteur conserve la propriété du droit d'auteur qui protège cette thèse. Ni la thèse ni des extraits substantiels de celle-ci ne doivent être imprimés ou autrement reproduits sans son autorisation.

0-612-29057-3

Canada

UNIVERSITY OF ALBERTA

FACULTY OF GRADUATE STUDIES AND RESEARCH

The undersigned certify that they have read, and recommend to the Faculty of Graduate Studies and Research for acceptance, a thesis entitled **Modeling and Fabrication of Rare-Earth-Doped Integrated Optical Waveguide Amplifiers** submitted by Madhu Krishnaswamy in partial fulfillment of the requirements for the degree of **Doctor of Philosophy**.

J. N. McMullin (Supervisor)

R. I. MacDonald

H. J. J. Seguin

F. Hegmann

B. Ventrudo
(External Examiner)

Date : April 17, 98

For my parents:

Sunder and Padma Krishnaswamy

Abstract

This thesis addresses modeling and fabrication issues related to erbium/ytterbium-doped glass waveguide amplifiers. Compact optical waveguides which amplify light in the 1.55 μm wavelength window will play an important role in complementing other integrated optic devices such as modulators and switches. In designing waveguide amplifiers, two features are of utmost importance : 1) high signal gain over short distances. 2) compatibility for integration with other devices. The requirement for gain over a short distance necessitates the use of rare-earth dopant levels two orders of magnitude higher than currently employed in fiber amplifiers.

A numerical model to simulate the gain and noise characteristics of waveguide amplifiers doped heavily with rare-earth ions is described. Deleterious effects associated with high doping, such as ion-ion interaction, are included in the model. The model is validated by comparing simulation results with experimental and numerical results found in the literature. Based on modeling results, an attempt was made to fabricate compact ridge waveguides from thin films of sputter-deposited erbium-doped glass. In response to various spectroscopic and micromachining impediments encountered with this process, alternative waveguide configurations were explored. The design and fabrication of strip-loaded waveguides using two dielectric glass films in conjunction is discussed. In this configuration, micromachining impediments inherent to the active glass film can be circumvented. Experimental and simulation results for this device are shown to be in close agreement. Improvements are forecast by the model.

Optical waveguides were also formed directly on rare-earth-doped bulk glasses. In one approach, a passive polymer waveguide was dispensed on top of a bulk glass. The evanescent field of light propagating in the polymer layer was seen to penetrate the bulk substrate and interact with rare-earth ions. Experimental and simulation results associated with this novel approach are discussed. Finally, an Er/Yb-doped optical waveguide amplifier yielding 3.5 dB of net signal gain over 4.2 cm with 120 mW of pump power is demonstrated. This singlemode device was formed on a bulk glass using a field-assisted, silver-sodium ion-exchange process.

Acknowledgements

I would like to express my deepest gratitude and appreciation to Dr. James N. McMullin for supervising my tenure as graduate student and for maintaining a pleasant working atmosphere. I am also indebted to Dr. Barrie Keyworth and Dr. R. Ian MacDonald for their valuable suggestions and guidance during this research.

I would like to thank all of my fellow researchers at TRLabs and the University of Alberta for their support and encouragement. In particular, I would like to acknowledge Rajkumar Nagarajan, Dino Corraza, David Boertjes, Sing Cheng, Rajashree Narendra, David Olsen, Reza Paiam, and Alan Hnatiw. I would like to thank David Clegg and Jason Lamont for a variety of technical assistance over the years.

My sincere thanks to the staff at The Alberta Microelectronic Centre, in particular Dr. James Broughton and Yan Loke for their contributions to this project. I would also like to thank the efforts of Graham McKinnon, Dr. Kevin Kornelson, Glen Fitzpatrick, Tran Tran and countless others who have shared their expertise with me.

I thank other professors at the Department of Electrical Engineering, University of Alberta, particularly Dr. V. Gourishankar, Dr. M. Brett, Dr. S. Dew, Dr. R. Lawson and Dr. R. Fedosejevs for academic and personal guidance. Many thanks to Dr. J. Hayden of Schott Glass Technologies for providing rare-earth-doped glasses. A tip of the hat to George Braybrook at the Department of Geology for some superb SEM photographs, five of which are featured in this thesis. I am grateful for the opportunity provided by Seastar Optics and Dr. Brian Ventrudo to conduct experiments at their research facility in Victoria, B.C in January of 1995. I am also appreciative of services rendered by the Westaim Corporation in Fort Saskatchewan and the National Research Council in Ottawa.

I would like to thank TRLabs and Dr. J. McMullin for their generous financial support over the years. Finally, I will forever be grateful to my parents and brothers, who have been an unwavering source of support and inspiration.

Table of Contents

Chapter Page

1. **Introduction** 1

2. **Review of Fundamental Concepts Relevant to the Study of Optical Waveguide Amplifiers** 6

  2.1 Light Propagation in Dielectric Waveguides 6

    2.1.1 Ray Optics 6

    2.1.2 Electromagnetic Optics 7

      2.1.2.1 Electromagnetic Analysis of a Planar Slab Waveguide 8

      2.1.2.2 Electromagnetic Analysis of Two-Dimensional Waveguides 10

      2.1.2.3 Intensity and Optical Power 11

    2.1.3 Photon Optics 12

  2.2 Energy Levels of Atoms 13

  2.3 Photon-Atom Interaction 14

    2.3.1 Absorption, Stimulated Emission and Spontaneous Emission: 14

    2.3.2 Pumping and Population Inversion 16

    2.3.3 Signal and Pump Propagation in an Amplifier 16

3. **Numerical Model for Rare-Earth-Doped Waveguide Amplifiers** 19

  3.1 Energy Levels for Er^{3+} and Yb^{3+} in Glass Hosts 19

  3.2 Pair-Induced and Co-operative Upconversion 22

  3.3 Ytterbium Sensitization 23

  3.4 Amplified Spontaneous Emission (ASE) Spectrum 24

  3.5 Model Algorithm 25

  3.6 Validation of Model for Er-doped Waveguide Amplifier 30

  3.7 Validation of Model for Er/Yb co-doped Waveguide Amplifier 36

  3.8 Material Parameters 41

  3.9 Closer Examination of Model Equations 42

4. **Fabricating Optical Waveguides from Thin Films of Sputtered/ PECVD Glass** 48

  4.1 Introduction 48

  4.2 Thin-film Deposition and Micromachining: 48

    4.2.1 Sputtering: 48

    4.2.2 Plasma-Enhanced Chemical Vapour Deposition (PECVD): 50

    4.2.3 Photolithography 51

4.2.4 Wet-Etching 52
4.2.5 Reactive-Ion-Etching (RIE) 52
4.3 Sputtering Er-doped Glass Films 53
4.4 Wet-Etching Sputtered Er-doped Glass Films 54
4.5 Reactive-Ion-Etching Sputtered Er-doped Glass Films 57
4.6 Reactive-Ion-Etching SiON Films 59
4.7 Fabricating Composite Multiple-Layer Ridge Waveguides 60
5. Micromachining Circular Hollow Channels from Planar Rectangular Glass Films 63
5.1 Introduction 63
5.2 Formation of Hollow Microchannel - Run #1 63
5.3 Formation of Hollow Microchannel - Run #2 67
5.3.1 Testing 72
5.4 Formation of Hollow Microchannel - Run #3 73
5.5 Potential Applications of Hollow Microchannels 76
6. Rare-Earth-Doped Waveguides in Strip-Loaded Configurations: Fabrication and Modeling 78
6.1 Introduction 78
6.2 Experimental Results for Erbium-doped Strip-Loaded Waveguide 78
6.2.1 Fabrication and Spectroscopy 78
6.2.2 Passive Optical Properties 81
6.2.3 Active Optical Properties 85
6.3 Correlating Simulation and Experiment 90
6.4 Design Options for Rare-Earth-doped Strip-Loaded Waveguides 92
7. Evanescent Pumping of Rare-Earth-Doped Bulk Glass Using Dispensed Polymer Waveguides - Fabrication and Modeling 104
7.1 Introduction 104
7.2 Polymer Waveguide on top of Er/Yb-doped Bulk Glass: Experimental Results. 104
7.2.1 Fabrication 104
7.2.2 Passive Optical Properties 106
7.2.3 Active Optical Properties 108
7.3 Design Options for Evanescently-Pumped Waveguide Amplifiers 112
8. Er/Yb-doped Waveguide Amplifier Fabricated by Dry, Field-Assisted, Silver-Sodium Ion-Exchange 118
8.1 Introduction 118
8.2 Bulk Ag^+/Na^+ Ion-Exchange in TRL-A 119

8.3 Bulk Ag$^+$/Na$^+$ Ion-Exchange in IOG-10 123
8.4 Fabrication of Ion-Exchanged Multimode Channel Waveguides 129
8.5 Optical Properties of Ion-Exchanged Multimode Channel Waveguides 132
8.6 Fabrication and Testing of Ion-Exchanged Singlemode Channel Waveguide Amplifier 136
Conclusions 141
References 142
Appendix A : Newton-Raphson Method to Solve Rate Equations 149

List of Tables

Table #	Caption	Page
3.1	Summary of basic transitions in Er^{3+} / Yb^{3+} co-doped glass.	21
3.2	Transitions resulting from interaction of adjacent Er^{3+} ions.	23
3.3	Material parameters used for the simulation of Ridge Waveguide 1.	32
3.4	Material parameters used for the simulation of Ridge Waveguide 2 [20,24]	38
4.1	Etch rates and selectivity for reactive ion etching sputtered erbium-doped glass film, with chrome acting as mask.	57
4.2	Optical loss characteristics of SiON ridge waveguides.	59
4.3	Fiber-to-fiber throughput loss for composite ridge waveguide.	62
6.1	Composition of sputtered Er-doped glass film, obtained using EDX.	80
6.2	Waveguide labels, SiON index and corresponding modal properties.	94
6.3	Optimum amplifier lengths for Strip-loaded waveguides A, B, C, and Ridge waveguide for various $P_p(0)$. $N_{Erb} = 2 \times 10^{26}$ ions/m^3; $N_{Yb} = 10 \times 10^{26}$ ions/m^3.	100
6.4	Broad-band ASE Power, In-band ASE Power and Output SNR for Strip-loaded waveguides A, B, C, and Ridge waveguide. $L = 10$ cm; $P_p(0) = 500$ mW; $N_{Erb} = 2 \times 10^{26}$ ions/m^3; $N_{Yb} = 10 \times 10^{26}$ ions/m^3.	102
8.1	Bulk ion-exchange of 0.2 µm silver film into 1 cm x 2 cm x 0.7 mm IOG-10 glass samples. Samples 1, 2 and 3 were diffused under identical temperature settings (320°C) but different electric field strengths.	124
8.2	Bulk ion-exchange of 0.5 µm silver film into 1 cm x 2 cm x 0.7 mm IOG-10 glass samples. Two samples diffused under identical electric field strengths (E=58 V/mm) but different temperature settings.	126
8.3	The amplifier reported in this thesis is listed along with the best reported results from several research groups involved in erbium-doped planar waveguide amplifiers (as of March 1998).	140

List of Figures

Figure #	Caption	Page
2.1	Ray Optics Illustration.	6
2.2	Planar Slab Waveguide : TE Polarization.	8
2.3	Rectangular 2-D Waveguide : TE Polarization.	10
2.4	Absorption of photon energy by an atom.	14
2.5	Stimulated emission of photon.	15
2.6	Spontaneous emission of photon.	15
2.7	Change in photon flux densities due to photon-atom interaction	17
3.1	Energy level diagram for Er^{3+} and Yb^{3+} in glass hosts.	20
3.2	Emission and absorption transition cross-section for a typical Er-doped silicate glass.	25
3.3	Pictorial illustration of rare-earth-doped waveguide amplifier model	26
3.4	Ridge Waveguide 1. The shaded region is the Er-doped SiO$_2$ core with index n=1.53. The core is surrounded on all sides by SiO$_2$ cladding of index n=1.51164. The TE field contours for the signal (λ_s=1550nm) and pump (λ_s=980nm) mode are shown on the left and right, respectively. The contours represent 90% to 10% of peak amplitude.	30
3.5	Normalized intensity profile of signal and pump along the center of Ridge Waveguide 1, within the Er-doped SiO$_2$ core.	31
3.6	Signal Gain vs. Pump Power for Ridge Waveguide 1. Comparison of numerical model developed in this chapter and experimental results from [31]. $P_s(0)=1\mu W$; L = 19.4 cm; $N_{Erb} = 0.485 \times 10^{26}$ iosn/m^3.	33
3.7	Signal Gain vs. Waveguide Length for Ridge Waveguide 1; $P_s(0)=1\mu W$; $P_p(0) = 500$ mW; $N_{Erb} = 0.485 \times 10^{26}$ ions/m^3.	34
3.8	Pump Depletion vs. Input Pump Power for Ridge Waveguide 1; $P_s(0) = 1\mu W$; L = 19.4 cm; $N_{Erb} = 0.485 \times 10^{26}$ ions/m^3.	34
3.9	Signal Gain vs. Input Signal Power for Ridge Waveguide 1; $P_p(0) = 50, 500$ mW; L = 10 cm; $N_{Erb} = 0.485 \times 10^{26}$ ions/m^3.	35
3.10	Ridge Waveguide 2. The shaded region is the Er/Yb co-doped core with index n=1.55. The core is surrounded on all sides by cladding of index n=1.51. The TE mode field envelope for the signal (λ_s=1550nm) and pump (λ_s=980nm) are shown on the left and right, respectively.	36
3.11	Normalized intensity profile of signal and pump along the center of Ridge Waveguide 2, within the Er/Yb co-doped core.	37
3.12	Signal Gain vs. Pump Power for Ridge Waveguide 2; L = 5 cm; $N_{Erb} = 2 \times 10^{26}$ ions/m^3; $N_{Yb} = 0, 10 \times 10^{26}$ ions/m^3.	39
3.13	Signal Gain vs. Erbium Concentration for Ridge Waveguide 2;	

$P_p(0) = 200$ mW; L = 5 cm; $N_{Yb} = 0, 10 \times 10^{26}$ ions/m^3. 39

3.14 Pump Depletion vs. Erbium Concentration for Ridge Waveguide 2; $P_p(0) = 200$ mW; L = 5 cm; $N_{Yb} = 0, 10 \times 10^{26}$ ions/m^3. 40

3.15 Signal Gain vs. Waveguide Length for Ridge Waveguide 2; $P_p(0) = 150, 300$ mW; $N_{Erb} = 2 \times 10^{26}$ ions/m^3; $N_{Yb} = 10 \times 10^{26}$ ions/m^3. 41

3.16 Signal Gain vs. Erbium Concentration for Ridge Waveguide 1; $P_p(0) = 200$ mW; L = 5 cm; $N_{Yb} = 0, 2.47, 8.5 \times 10^{26}$ ions/m^3. 43

3.17 Signal Gain vs. Ytterbium Concentration for Ridge Waveguide 1; $P_p(0) = 200$ mW; L=2,3,4 and 5 cm; $N_{Erb} = 1.4 \times 10^{26}$ ions/m^3. 44

3.18 Pump Power vs. Waveguide Length for Ridge Waveguide 1; $P_p(0) = 200$ mW; $N_{Erb} = 1.4 \times 10^{26}$ ions/m^3; $N_{Yb} = 0, 8.5 \times 10^{26}$ ions/m^3. 45

3.19 Signal Power vs. Waveguide Length for Ridge Waveguide 1; $P_p(0) = 200$ mW; $N_{Erb} = 1.4 \times 10^{26}$ ions/m^3; $N_{Yb} = 0, 8.5 \times 10^{26}$ ions/m^3. 45

3.20 Gain Coefficient vs. Waveguide Length for Ridge Waveguide 1; $P_p(0) = 200$ mW; $N_{Erb} = 1.4 \times 10^{26}$ ions/m^3; $N_{Yb} = 8.5 \times 10^{26}$ ions/m^3. 46

3.21 Absorption Coefficient vs. Waveguide Length for Ridge Waveguide 1; $P_p(0) = 200$ mW; $N_{Erb} = 1.4 \times 10^{26}$ ions/m^3; $N_{Yb} = 8.5 \times 10^{26}$ ions/m^3. 46

3.22 ASE Power Spectrum for Ridge Waveguide 1; $P_p(0) = 200$ mW; L = 5cm; $N_{Erb} = 1.4 \times 10^{26}$ ions/m^3; $N_{Yb} = 8.5 \times 10^{26}$ ions/m^3. 47

4.1 Sputtering chamber (left) and collision cascade at the target (right). 49

4.2 Photolithographic steps : spin-coating of photo-resist (top), selective exposure to UV-light (middle), developing the exposed regions of the photo-resist (bottom). 51

4.3 Chemical wet-etching : Isotropic etch-profile and under-cut (left), non-rectangular optical waveguide (right). 52

4.4 Reactive Ion Etching: Anisotropic etch-profile of glass and mask erosion (left), rectangular optical waveguide (right). 53

4.5 Profilometer scan revealing build-up of etch residue adjacent to ridge. 54

4.6 SEM photograph of ridge waveguide fabricated by wet-etching 55

4.7 Stress induced on ridge waveguide by deposition of upper-cladding. 56

4.8 Change in ridge waveguide structure following reflow step. 56

4.9 Rib formed on sputtered Er-doped glass film using RIE : RF Power = 100W. 58

4.10 Rib formed on sputtered Er-doped glass film using RIE : RF Power = 250W. 58

4.11 Rib formed on SiON film using RIE : RF Power of 80W. 59

4.12 Design of composite SiON/Er-doped ridge waveguide. 60

4.13 SEM picture of composite SiON/Er-doped ridge waveguide. 61
4.14 "Grass" pattern on sidewall of composite ridge waveguide. 61
4.15 Near-field image of 975nm light in composite ridge waveguide. 62
5.1 A 0.7μm x 7μm rib wet-etched on sputtered Er-doped film. 63
5.2 One hour anneal at 600°C in H_2O vapour. 64
5.3 Two hour anneal at 600°C in H_2O vapour. 65
5.4 Three hour anneal at 600°C in H_2O vapour; 7μm wide rib. 65
5.5 Three hour anneal at 600°C in H_2O vapour; 2 μm wide rib. 66
5.6 One hour anneal of a planar sputtered film. 67
5.7 1.0μm x 6μm rib etched on a 1.3μm-thick sputtered film. 68
5.8 Cleaved edge of a sample annealed for 60 minutes. 69
5.9 Multiple microchannels on the same substrate. 69
5.10 Uncleaved edge of a sample annealed for 60 minutes. 70
5.11 Cleaved edge of a sample annealed for 30 minutes. 71
5.12 Near-field image showing light propagating within the hollow microchannel. 72
5.13 Water entering the hollow microchannel through capillary action. 72
5.14 Shallow etch fails to produce well-defined hollow microchannels. 73
5.15 A deeper etch produces a well-defined hollow microchannel. The cross-section of this microchannel differs from earlier runs due to adhesion effects. 74
5.16 A 12 μm high, 50 μm wide microchannel. 75
5.17 Water inside one arm of a Y-branch microchannel. 75
5.18 Existing technology to fabricate hollow microchannels. 76
5.19 Formation of circular microchannels through selective accumulation of gas and de-adherence. 77
6.1 Transmission spectrum for TRL-A bulk glass. 78
6.2 X-ray Photon Intensity vs. Electron Bombarding Energy - EDX scan of sputtered Er-doped glass film. 79
6.3 SEM photograph showing cross-section of strip-loaded waveguide. 80
6.5 Strip-loaded Waveguide A. The dark-shaded layer is the erbium-doped sputtered film, with index n=1.59; the un-shaded layer is the SiON rib, with index n=1.56; the light-shaded layer is the SiO_2 cladding with index n=1.46. The TE field contours for the fundamental signal and pump mode are shown on the left and right, respectively. The contours represent 90% to 10% of peak amplitude. The device was 1.2 cm long. 81
6.6 Normalized signal and pump intensity profiles along the center of strip-loaded waveguide A, within the sputtered erbium-doped film. 82
6.7 Image of near-field intensity for strip-loaded waveguide A, showing

90% to 10% contours for the 975nm pump beam. X and Y axes represent pixel numbers. 10 pixels ~ 1.3 μm. 83

6.8 Cut-back throughput loss measurements for erbium-doped strip-loaded waveguide A and a comparison passive strip-loaded SiON waveguide. The measurements indicate strong absorption by erbium at 975 nm and 1547 nm. Measurements on the passive waveguide indicate excess propagation losses of 0.8 dB/cm. 84

6.9 Spontaneous emission spectrum observed in strip-loaded waveguide A. The excitation source was 23 mW, launched from a single 975nm laser diode. 85

6.10 Luminescence lifetime measurement for strip-loaded waveguide A. Oscilloscope reading $\Delta T = 148\ \mu s$ corresponds to the time taken for the intensity to decay to 1/e of its peak value ($\Delta V = 0.248$ V). 86

6.11 Light exiting strip-loaded waveguide A resolved on an optical spectrum analyser. Multiple signal cavity-modes in the absence of pump (above) and in the presence of 45 mW of launched pump power (below). 88

6.12 Enhancement in Signal Throughput vs. Waveguide Length. Experimental result for second batch of erbium-doped, strip-loaded waveguide A. 89

6.13 Enhancement of Signal Throughput vs. Launched 975nm Pump Power. Experimental result for second batch of erbium-doped, strip-loaded waveguide A. 89

6.14 Enhancement of Signal Throughput vs. Launched 975 nm Pump Power. Comparison of experimental results and simulation for strip-loaded waveguide A. $P_s(0) = -8$ dBm; $N_{Erb} = 3 \times 10^{26}$ ions/m^3; $\tau_{21} = 148\ \mu s$; $l_s = l_p = 0.8$ dB/cm. 90

6.15 Signal Gain vs. Waveguide Length : Simulation of strip-loaded waveguide A. $P_p(0) = 0$, 50mW; $N_{Erb} = 3 \times 10^{26}$ ions/m^3; $\tau_{21} = 148\ \mu s$; $l_s = l_p = 0.8$ dB/cm. 91

6.16 Signal Gain vs. Waveguide Length : Simulation of strip-loaded waveguide A. $P_p(0) = 200$mW; $\tau_{21} = 10$ms; $N_{Erb} = 3 \times 10^{26}$ ions/m^3; $N_{Yb} = 10 \times 10^{26}$ ions/m^3. 92

6.17 Signal Gain vs. Waveguide Length for strip-loaded waveguide A (simulation). $P_p(0) = 500$mW; $N_{Erb} = 2{,}3 \times 10^{26}$ ions/m^3; $N_{Yb} = 10 \times 10^{28}$ ions/m^3. 93

6.18 Signal Gain vs. Pump Power for strip-loaded waveguide A (Simulation). L = 10cm, Optimized; $N_{Erb} = 2 \times 10^{26}$ ions/m^3; $N_{Yb} = 10 \times 10^{26}$ ions/m^3. 93

6.19 Ridge Waveguide. The un-shaded layer is the rare-earth-doped sputtered film, with index n=1.59; the shaded layer is the SiO_2 cladding with index n=1.46. The TE field contours for the fundamental signal and pump mode are shown on the left and right, respectively. The contours represent 90% to 10% of peak amplitude. 95

6.20 Normalized signal and pump intensity profiles along the center of Ridge Waveguide, within the sputtered film. 95

6.21 Strip-loaded Waveguide B. The dark-shaded layer is the rare-earth -doped sputtered film, with index n=1.59; the un-shaded layer is the SiON, with index 1.59; the light-shaded layer is the SiO_2 cladding with index n=1.46. The TE field contours for the fundamental signal and pump mode are shown on the left and right, respectively. The contours represent 90% to 10% of peak amplitude. 96

6.22 Normalized signal and pump intensity profiles along the center of Strip-loaded Waveguide B, within the sputtered film. 96

6.23 Strip-loaded Waveguide C. The dark-shaded layer is the rare-earth-doped sputtered film, with index n=1.59; the un-shaded layer is the SiON, with index 1.62; the light-shaded layer is the SiO_2 cladding with index n=1.46. The TE field contours for the fundamental signal and pump mode are shown on the left and right, respectively. The contours represent 90% to 10% of peak amplitude. 97

6.24 Normalized signal and pump intensity profiles along the center of Strip-loaded Waveguide C, within the sputtered film. 97

6.25 Signal Gain vs. Waveguide Length : Comparison between Ridge, Strip-loaded waveguides A, B, and C. $P_p(0) = 200$ mW; $N_{Erb} = 2 \times 10^{26}$ ions/m^3. 98

6.26 Signal Gain vs. Waveguide Length : Comparison between Ridge, Strip-loaded waveguides A, B, and C. $P_p(0) = 200$ mW; $N_{Erb} = 3 \times 10^{26}$ ions/m^3. 98

6.27 Signal Gain vs. Waveguide Length : Comparison between Strip-loaded waveguides A, B, C and Ridge Waveguide. $P_p(0)$=500mW; $N_{Erb} = 2 \times 10^{26}$ ions/m^3. 99

6.28 Signal Gain vs. Waveguide Length : Comparison between Strip-loaded waveguides A, B, C and Ridge Waveguide. $P_p(0)$=500mW; $N_{Erb} = 3 \times 10^{26}$ ions/m^3. 100

6.29 Signal Gain vs. Pump Power : Theoretical comparison between Strip-loaded waveguides A, B, C, and Ridge waveguide. Length Optimized. 101

6.30 Conceptual schematic of an integrated combiner/WSC/ amplifier/WSC module 103

7.1 Schematic of polymer waveguide dispensed on bulk glass. 105

7.2 Fundamental pump (above) and signal (below) mode-profile for dispensed polymer waveguide shown in Figure 7.1. 107

7.3 Experimental set-up to study active properties of polymer waveguides dispensed on QX/ER bulk glass. 108

7.4 Spontaneous emission spectrum observed in polymer waveguide dispensed on QX/ER bulk glass. 109

7.5 Lifetime of spontaneous emission for polymer waveguide dispensed atop QX/ER bulk glass. 110

7.6 Enhancement in Trasmitted Signal vs. Residual Pump Power for polymer waveguide dispensed atop QX/ER bulk glass. 111

7.7 Evansescent A - Shaded region is 5 µm x 2.5 µm passive rib with n=1.55; un-shaded region is 2mm thick rare-earth-doped bulk substrate (n=1.53). 112

7.8 Evansescent B - Shaded region is 5µm x 0.7µm passive rib (n=1.62); un-shaded region is 2mm-thick rare-earth-doped bulk substrate (n=1.53). 113

7.9 Signal Gain vs. Waveguide Length for Evanescent waveguide A: $P_p(0)$ = 500 mW; N_{Yb}= 10 x 10^{26} ions/m^3; N_{erb}=varies. 114

7.10 Signal Gain vs. Waveguide Length for Evanescent waveguide A: $P_p(0)$ = 500 mW; N_{Erb}= 1x 10^{26} ions/m^3; N_{yb}=varies. 114

7.11 Signal Gain vs. Waveguide Length for Evanescent waveguide B: $P_p(0)$ = 500 mW; N_{Yb}= 1x 10^{26} ions/m^3; N_{erb}=varies. 115

7.12 Signal Gain vs. Waveguide Length for Evanescent waveguide B: $P_p(0)$ = 500 mW; N_{Erb}= 1x 10^{26} ions/m^3; N_{yb}=varies. 116

7.13 Signal Gain vs. Pump Power - Comparison of Evanescent waveguides A & B : $P_p(0)$ = 500 mW; N_{Erb}= 1x 10^{26} ions/m^3; N_{Yb}=10x 10^{26} ions/m^3. 116

8.1 Experimental set-up for field-assisted silver-film ion-exchange into glass. 119

8.2 Current flow (Voltage/800 Ohms) through TRL-A upon the application of a 143 V/mm electric field at 320°C. 120

8.3 SEM photograph showing cross-section of TRL-A after ion-exchange. The diffusion depth can be approximated by the intensity of back-scattered electrons, which is brighter wherever highly reflective silver ions are present. 121

8.4 Pictorial illustration of prism-coupler. 121

8.5 Prism-coupler analysis of TRL-A after ion-exchange. Seven TE modes with N_m ranging from 1.7095 to 1.6996 were found at λ=633 nm. 122

8.6 Refractive index (@λ=633 nm) as a function of depth (in Angstroms) after silver ion-exchange into TRL-A. 123

8.7 SEM photograph : Cross-section of sample 2 after ion-exhange. 124

8.8 Refractive index (@λ=633nm) as a function of depth for Samples 1, 2 and 3. Diffusion Temp = 320°C; Anode = 0.2 µm silver. 125

8.9 SEM photograph showing cross-section of Sample 4 after ion-exchange. The diffusion depth is ~ 12 µm. 126

8.10 Refractive index (@λ=633nm) as a function of depth after ion-exchange. Samples 4 and 5 - E = 58 V/mm;Anode = 0.5 µm silver. 126

8.10 Contour plots showing fundamental signal (left) and pump (right) TE mode in graded-index sample 2. 127

8.11 Contour plots showing fundamental signal (left) and pump (right) TE mode in graded-index sample 5. 128

8.12 Steps involved in fabricating ion-exchanged channel waveguides. Top : Narrow openings are exposed on the chrome mask and silver is deposited. Middle : Ion-exchange occurs wherever chrome is absent. Bottom : Metal films are stripped, revealing channel waveguides. 129

8.13 Current flow (Voltage/800 Ohms) through IOG-10 during ion-exchange. E = 58 V/mm; Temp = 320°C; Anode = 0.5 μm silver. 130

8.14 Profilometer scan reveals surface expansion in diffused regions of the glass due to stress. 130

8.15 Cross-section of ion-exchanged multimode channel waveguide in IOG-10 glass, observed through an optical microscope. 131

8.16 Electric-field lines connecting a narrow anode source to a wide cathode sink. 131

8.17 Lateral compression of electric field lines due to closely spaced mask openings. 132

8.18 Decay of luminescence intensity as a function of time in ion-exchanged channel waveguide. Chopping frequency was 25 Hz. 132

8.19 Enhancement in transmitted signal as a function of residual pump power in 1.5 cm-long ion-exchanged multimode waveguide. Signal transparency (0 dB gain) was achieved for a maximum input pump power of 66 mW. The input signal power was -13 dBm. 133

8.20 Pump loss as a function of input pump power in ion-exchanged multimode waveguide. 134

8.21 Enhancement in transmitted signal as a function of input signal power in ion-exchanged multimode waveguide. The input pump (976.3 nm) power was 66 mW. 134

8.22 Enhancement in transmitted signal as a function of input pump power for two different pump wavelengths. 135

8.23 Enhancement in transmitted signal as a function of input pump power in 0.5 cm-long ion-exchanged multimode waveguide. Signal transparency (0 dB gain) was achieved for an input pump power of 25 mW. The input signal power was -15 dBm. 136

8.24 Prism-coupler analysis of ion-exchanged slab waveguide sample 1 (from Section 8.3). One TE mode was found at λ=1550 nm. 137

8.25 Cross-section of ion-exchanged singlemode channel waveguide. 138

8.26 Net signal gain as a function of input pump power in a 4.2 cm-long ion-exchanged singlemode waveguide. Signal transparency (0 dB gain) occurs for an input pump power of ~48 mW. The pump was a 976.3 nm laser diode introduced into one end of the waveguide. 138

8.27 Net signal gain as a function of pump power in a dual-pumped, 4.2 cm-long ion-exchanged singlemode waveguide. Signal transparency occurs for a combined input pump power of ~30 mW. The co-propagating pump was a 976.3 nm laser diode and the counter-propagating pump was a 983.8 nm laser diode. 139

Chapter 1 : Introduction

The development of semiconductor lasers and low-loss silica fibers in the 1960's made it possible to transmit information using carriers at optical frequencies. The advantages of transmitting information in this fashion are numerous : increased bandwidth, signal security, low cost, etc. The past three decades have seen a succession of improvements in the speed and bandwidth of fiber optic communication systems. However, optical carrier bandwidths have yet to be fully utilized due to the bottlenecks created by electronic devices. In the next generation of optical communication systems, integrated optic devices are expected to reduce electrical-optical-electrical interfaces which limit the bandwidth and speeds achievable in the current system. Compact optical devices which amplify light in the 1.55 μm wavelength window will play an important role in complementing other integrated optic devices such as modulators and switches.

Erbium (Er^{3+}) doped glasses are known to amplify light at a wavelength of 1.55 μm through stimulated emission of radiation. An optical source, typically operating at 0.98 μm, provides the population inversion required for stimulated emission. Fiber waveguides doped with small amounts of erbium (Erbium-doped Fibre Amplifiers or EDFAs) have been extensively researched and are now being used in long-haul optical communication systems as repeaters, power amplifiers etc. This decade has seen research activity aimed at creating a small-scale version of the EDFA for application in integrated optics. The primary requirements for an integrated optic waveguide amplifier are : 1) high signal gain over short distances. 2) compatibility for integration with other integrated optic devices. Since the operating length of optical amplifiers has an inverse dependence on erbium dopant concentration, amplification over short distances requires erbium dopant levels two orders of magnitude higher than currently used in fiber amplifiers. The requirement for compatibility limits the fabrication options to silica-based thin-film technology or bulk-glass technology.

The solubility of erbium in silica is limited to about 10^{18} ions/cm^3, beyond which erbium ions tend to form clusters and are unproductive. Network modifiers like sodium and lanthanum can create additional sites in the glass which can then host larger amounts of erbium (>10^{20} ions/cm^3 or 1 wt%). Chemical Vapour Deposition (CVD) and Flame Hydrolysis Deposition (FHD), both of which are vapour-phase deposition processes, yield high-quality glass films with 95% silica content. However, it isn't possible to introduce network modifiers using these processes. Thus, the incorporation of rare-earth ions is limited to a fraction of a weight percent. Erbium-doped waveguide amplifiers have been successfully demonstrated using CVD and FHD silica films, but at operating lengths around 20 cm. This is an unavoidable consequence of the low erbium content. To scale down the device even further, multi-component glasses with appropriate network modifiers and large amount of erbium (2-3 wt%) are required. Optical waveguides can be formed either directly on such multi-component glasses (ion-exchange) or on a thin-film replica of the bulk glass (sputter-deposition). Both approaches will be investigated during the course of this thesis. In addition to demonstrating a rare-earth-doped waveguide amplifier, the goals of this thesis are to investigate novel waveguide amplifier configurations which could be fabricated and potentially integrated with ease.

In Chapter 2, some of the fundamental concepts relevant to the study of optical waveguide amplifiers (electromagnetic theory and laser theory, in particular) are discussed. Selected expressions and derivations are presented from the numerous textbooks and manuscripts available on these topics. In Chapter 3, a numerical model which simulates the gain and noise characteristics of erbium/ytterbium-doped waveguide amplifiers is described. The model considers most of the important radiative and non-radiative transitions between four energy levels of erbium and two energy levels of ytterbium. The model also accounts for energy transfer between erbium ions in close proximity (co-operative upconversion), a phenomenon which adversely affects the efficiency of an amplifier. Amplified Spontaneous Emission (ASE) over a 113 nm wavelength range is acounted for. The model is validated by comparing simulation results with other published numerical and experimental work.

In Chapter 4, the sequence of steps involved in the fabrication of optical waveguides from sputtered and PECVD glass is described. Using an erbium-doped (3wt%) lanthanum sodium silicate glass as a target, thin films of glass were sputter-deposited on a silicon wafer. Fabricating deep-trench, low-loss ridge waveguides by selectively etching away the sputtered material proved impossible due to the complex chemistry of the glass. However, the micromachining properties of silicon oxynitride (SiON) were found to be more suitable for fabrication of such waveguides.

Chapter 5 is a short detour describing the investigation of an unexpected and intriguing phenomenon. When annealing sputtered erbium-doped glass, it was observed that the films did not adhere well to the underlying silicon dioxide layer, often peeling or buckling at random. However, it was noticed that geometrical patterns etched on the film (for the purposes of making an optical waveguide) gave shape to this random process. The de-adherence resulted in hollow microchannels with strikingly circular cross-sections. From further observations, it was inferred that selective accumulation of gas and the accompanying build-up of pressure were responsible for this structural transformation. References in the literature support this explanation, which remains empirical and incomplete. Potentially, hollow micro-channels fabricated using this concept of "miniaturized glass-blowing" could prove useful in micro-fluidic applications. The work described in this chapter was initially reported in *Electronics Letters* ("Formation of hollow glass microcylinders on silicon", Vol. 32, No.22, Oct. 1996) and then expanded on in *Conference on Rare-earth-doped Devices,* SPIE Photonics West '97 ("Formation of hollow microcylinders from sputtered erbium-doped glass films", 2996-12).

Returning to optical waveguide amplifiers, the impediments encountered while attempting to micromachine ridges on multicomponent glass films spurred a search for alternative structures. Chapter 6 describes a strip-loaded waveguide configuration, formed by depositing and patterning a passive SiON rib on top of the sputtered glass. Spontaneous emission in the 1520-1570 nm band was observed in this device when pumped at 975 nm. Signal (λ=1535 nm) loss in the device was seen to improve by up to 3 dB upon pumping, indicating an accumulation of erbium ions in the metastable state. These experimental results were in close agreement with simulation. Poor spectroscopic properties and co-operative upconversion combined to limit the performance of this device. The results obtained in connection with this work were published in *The Journal of Optical Materials* ("Optical Properties of Strip-Loaded Er-doped Waveguides", vol. 6, Nov. 1996, pp. 287-292). For the purposes of integration, the refractive-index variation and etching options available with SiON make it an ideal candidate as the index-loading layer. The SiON index can be lowered to allow for significant light penetration into the sputtered film (and hence, stimulated emission). Alternatively, the index of the SiON can be made very high (up to n=2.0) in selected regions of the wafer, thus reducing the underlying erbium-doped film to a cladding layer wherever passive devices are desired. Using the numerical model, design options for rare-earth-doped strip-loaded waveguides are explored in Chapter 6.

Chapter 7 continues the investigation of atypical waveguide structures for potential use as amplifiers. Passive polymer waveguides were formed on top of a 2mm-thick erbium/ytterbium-doped bulk glass. The higher-index polymer provided lateral light confinement, similar to the function of the SiON rib in the strip-loaded waveguide. Unlike the strip-loaded device, the active layer is not a thin film; in this configuration, the entire substrate contains rare-earth ions. A relatively high index difference between the polymer layer and the active substrate was required to sustain a guided mode. Consequently, only the evanescent portion of the light penetrated into the substrate to stimulate emission. Signal enhancement of 1.7 dB was observed with more than 200 mW of input pump power. This was barely adequate to compensate for the erbium-induced absorption loss in this device. According to simulations, the gain coefficient and power efficiency of evanescently-pumped amplifiers will be poor given the weak overlap between light and erbium ions. However, the fabrication does not require any micro-machining or clean-room processing, a trade-off worth exploring further. Experimental results were reported in *The IEEE Journal of Selected Topics in Quantum Electronics* ("Optical Properties of Polymer Waveguides Dispensed on an Er/Yb co-doped Glass", vol. 2, June, 1996).

In Chapter 8, optical waveguides were formed just below the surface of a rare-earth-doped bulk glass using a field-assisted, silver-sodium ion-exchange process. Thin films of metallic silver were used as the source for diffusion. Owing to a larger ionic radii, the silver ions (which replace sodium ions) densify the glass and raise its refractive index. Optical waveguides with graded-index profiles were formed near the surface of a bulk erbium(1wt%)/ytterbium(3wt%)-doped glass. Signal transparency (or 0 dB gain) was achieved in a 1.5 cm-long, multimode ion-exchanged waveguide with 66 mW of input pump power. Net signal gain of 3.5 dB was achieved in a 4.2 cm-long, singlemode ion-exchanged waveguide with 120 mW of input pump power. The excess propagation losses in this device at 1.533 μm were estimated to be below 0.2 dB/cm.

Chapter 2 : Review of Fundamental Concepts Relevant to the Study of Optical Waveguide Amplifiers

In an optical amplifier, the optical power of light varies as it propagates along a rectangular dielectric waveguide doped with active atoms. The following aspects of engineering play a role in the study of optical amplifiers : 1) electromagnetic theory and photon optics, relevant to studying the propagation characteristics of light in a given dielectric structure; 2) quantum atomic theory, relevant to understanding energy level distributions of atoms; and 3) laser theory, relevant to examining atomic transition probabilities, population inversion rates, etc. These three topics are given an introductory review in Sections 2.1-2.3 and then considered together in the next chapter for the specific case of rare-earth-doped optical waveguide amplifiers.

2.1 Light Propagation in Dielectric Waveguides

2.1.1 Ray Optics

Ray optics offers the most basic perspective of light propagation in dielectric waveguides. The location and direction of light is represented by geometrical rays, as shown in Figure 2.1.

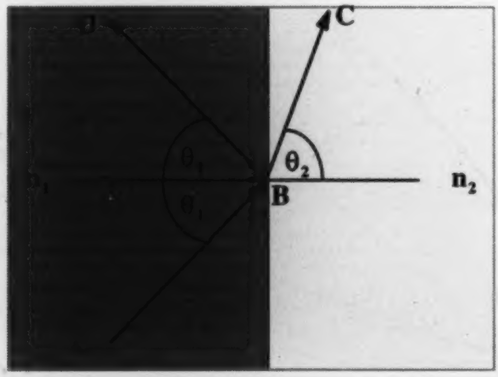

Figure 2.1 Ray Optics Illustration

Fermat's Principle states that the optical ray travelling between points A and B follows a path such that the time of travel is a minimum relative to alternate paths [1]. When the ray is incident upon another medium (with refractive index $n_2 < n_1$), the incident ray is split into a reflected ray BD (which remains in the original medium) and a refracted ray BC (which enters the new medium). The geometrical path of the refracted ray obeys Snell's Law (proved by applying Fermat's Principle between points A and C):

$$n_1 \operatorname{Sin} \theta_1 = n_2 \operatorname{Sin} \theta_2 \tag{2.1}$$

When θ_1 reaches a critical angle such that $\theta_2 = 90$ degrees, the refracted ray BC lies along the interface between the two media. Beyond the critical angle, θ_2 is imaginary and the incident ray is totally reflected, thus remaining within the original medium. This concept of *total internal reflection* is the basis for confining light within a desired medium and creating an *optical waveguide* [2].

2.1.2 Electromagnetic Optics

The electromagnetic properties of light have to be considered when optical power distribution is of interest, as is the case with lasers and amplifers. The electromagnetic radiation of light is described by two vectors : the electric field E(r, t) and the magnetic field H(r, t). In a medium in which there are no free electric charges or currents, such as in an optical waveguide, two additional vector fields are defined : the electric flux density D(r,t) and the magnetic flux denisty B(r,t). In this thesis, the medium in which light propagates will be assumed to be linear, homogenous, non-dispersive and isotropic [1]. In such a medium, E, H, D and B are all continuous functions of position and time and are related through the following expressions :

$$\overline{D} = \varepsilon \overline{E} \tag{2.2}$$

$$\overline{B} = \mu_o \overline{H} \tag{2.3}$$

where ε = electric permittivity and μ_0 = magnetic permeability.

E and H must satisfy a set of coupled partial differential equations (Maxwell's equations)

$$\nabla \times \bar{E} = -\frac{\partial \bar{B}}{\partial t} \tag{2.4}$$

$$\nabla \times \bar{H} = \frac{\partial \bar{D}}{\partial t} \tag{2.5}$$

$$\nabla \cdot \bar{D} = 0 \tag{2.6}$$

$$\nabla \cdot \bar{B} = 0 \tag{2.7}$$

subject to the condition that the tangential components of E and H and the normal components of D and B be continuous across the boundary separating two dielectric media. Taking the curl of Eqn. 2.4 and using a vector identity leads to the vector *wave equation :*

$$\nabla^2 \bar{E} - \mu_o \varepsilon \frac{\partial^2 \bar{E}}{\partial t^2} = 0 \tag{2.8}$$

A similar expression holds for H. In rectangular cartesian coordinates, the scalar components of the wave equation can be de-coupled and written as follows :

$$\frac{\partial^2 E_i}{\partial x^2} + \frac{\partial^2 E_i}{\partial y^2} + \frac{\partial^2 E_i}{\partial z^2} - \mu_o \varepsilon \frac{\partial^2 E_i}{\partial t^2} = 0 \qquad i = x, y, z \tag{2.9}$$

2.1.2.1 Electromagnetic Analysis of a Planar Slab Waveguide

A planar slab waveguide consists of a high index (n_1) dielectric core layer surrounded on either side by lower index (n_2) dielectric cladding layers. Light is confined within the core in one dimension through total internal reflection. The structure is infinite in width (y-axis) and invariant along its length (z-axis).

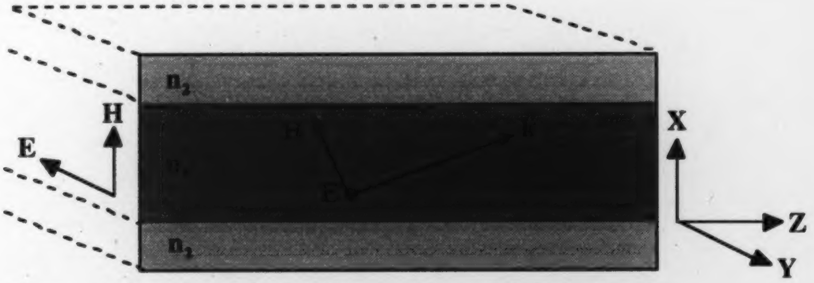

Figure 2.2 Planar Slab Waveguide : TE Polarization

In this thesis, the field polarization will always be assumed to be transverse electric (TE). Hence, E_x, E_z and $H_y = 0$ but E_y, H_x and $H_z \neq 0$. The wavevector k points in the direction of propagation and has magnitude :

$$k = n\, k_o = n\, \frac{2\pi}{\lambda_o} \tag{2.10}$$

To find the electric field distribution for this waveguide, the scalar wave equation (Eqn. 2.9) must be solved in each of the three layers and linked together using the boundary conditions. When the electromagnetic wave is monochromatic, the field solution can be expressed as sinusoidal functions of time (of frequency ω) :

$$E_y(x,z,t) = E_y(x,z)\, e^{j\omega t} \tag{2.11}$$

The structural invariance along z suggests that the field solution takes a spatially sinusoidal form along z as well :

$$E_y(x,z,t) = E_y(x)\; e^{-j\beta z} e^{j\omega t} \tag{2.12}$$

If the trial solution (Eqn. 2.12) is inserted into Eqn. 2.9, the wave equation simplifies to :

$$\frac{\partial^2 E_y(x)}{\partial x^2} + (k_o^2 n_i^2 - \beta^2) E_y(x) = 0 \qquad \text{where i=layer 1,2,3} \tag{2.13}$$

β is the longitudinal (z-axis) component of the k vector. The solution for 2.13 depends on the relative magnitudes of $k_o n_i$ and β :

$$E_y(x) = E_o \exp(\pm\sqrt{\beta^2 - k_o^2 n_i^2}\;\, x) \qquad \text{when } \beta > k_o n_i \tag{2.14}$$

$$E_y(x) = E_o \left\{ Cos(\sqrt{k_o^2 n_i^2 - \beta^2}\;\, x) + Sin(\sqrt{k_o^2 n_i^2 - \beta^2}\;\, x) \right\} \qquad \text{when } \beta < k_o n_i \tag{2.15}$$

E_o is the field amplitude at x=0. The structure is said to sustain a *guided mode* when $E_y(x)$ takes the sinusoidal form of Eqn. 2.15 within the core and the exponential (or *evanescent*) form of Eqn. 2.14 within the cladding layers. A necessary condition for a guided mode is :

$$k_o n_2 \; < \; \beta \; < \; k_o n_1 \tag{2.16}$$

When the boundary conditions at the core/cladding interface are enforced on Eqns. 2.14 and 2.15, only certain values of β (within the bounds of Eqn. 2.16) emerge as allowed solutions. These discrete values of β are called the eigenvalues of the waveguide and the corresponding solutions are called the eigenmodes or modes of the waveguide.

2.1.2.2 Electromagnetic Analysis of Two-Dimensional Waveguides

A rectangular waveguide (Figure 2.3) differs from a planar slab waveguide in one respect : the high-index core is now surrounded on all four sides by a lower index cladding. This configuration confines light in two dimensions (x and y) as it propagates along the z-axis. Consequently, the electromagnetic field is now a function of x and y.

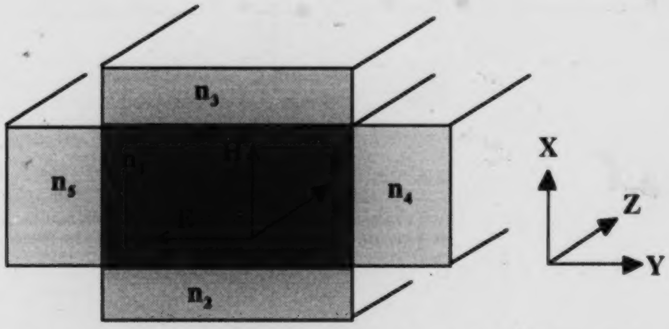

Figure 2.3 Rectangular 2-D Waveguide : TE Polarization

The scalar wave equation for the rectangular waveguide is given by :

$$\frac{\partial^2 E_y(x,y)}{\partial x^2} + \frac{\partial^2 E_y(x,y)}{\partial y^2} + (k_o^2 n_i^2 - \beta^2)E_y(x,y) = 0 \qquad i=1,2,\ldots 5 \tag{2.17}$$

The guided mode solutions of Eqn. 2.17 will have a sinusoidal form in both x and y within layer 1, sinusoidal in y and exponential in x within layers 2 and 3, and sinusoidal in x and exponential in y within layers 4 and 5. By applying the boundary conditions, the discrete eigenmodes of the structure and the corresponding electric field distributions $E_y(x,y)$ can be obtained. Eqn. 2.17 has to be solved in five layers and the solutions linked across four boundaries. The reader is referred to several pioneering text books and publications which deal at length with analytical and numerical analysis of rectangular dieletric waveguides [3-

15]. In this thesis, modal analysis of dielectric waveguides is a means to an end. Therefore, a public-domain software package was used to generate the required information. FWAVE [16] is a numerical analysis tool which relies on a finite-difference algorithm to calculate the modal properties of rectangular waveguides. For most of the waveguides considered in this thesis, the modal properties and electric field distributions were obtained using FWAVE.

2.1.2.3 Intensity and Optical Power

The instantaneous intensity of an electromagnetic wave at a point x,y within the waveguide cross-section is described by the *Poynting vector* :

$$I_z(x,y) = E_y(x,y) \times H_x(x,y) \tag{2.18}$$

It is easy to show (from Maxwell's Eqn. 2.4) that in the TE case, E_y and H_x are related by :

$$H_x(x,y) = \frac{\beta}{\mu_o \omega} E_y(x,y) \tag{2.19}$$

Hence, the magnitude of the local intensity is proportional to the squared absolute value of the envelope of the local electric field :

$$I_z(x,y) \propto \left| E_y(x,y) \right|^2 \tag{2.20}$$

To calculate the total power of the electromagnetic radiation contained within the waveguide, the local intensity has to be integrated over the waveguide cross-section S :

$$P(z) = \iint_S I_z(x,y)\ dx\ dy \tag{2.21}$$

For the application discussed in this thesis, the total optical power launched into the waveguide is a known input parameter but the local intensity is not. However, it is the local intensity which determines the extent of photon-atom interaction in an optical amplifier (as will be shown in Section 2.3). The following steps relate total optical power, local electric field and local intensity :

1) For a waveguide with a specific cross-sectional and refractive index profile, the wave

equation can be solved assuming an arbitrary amplitude E_o=1 (in Eqns. 2.14 and 2.15) to produce the *electric field envelope* $\psi_e(x,y)$ for a guided mode.

2) Squaring $\psi_e(x,y)$ yields the corresponding *mode intensity envelope* $\psi_i(x,y)$, as suggested by Eqn. 2.20.

3) The following expression relates $\psi_i(x,y)$ and P(z) to the local intensity I(x,y):

$$I(x,y) = P(z)\frac{\psi_i(x,y)}{\iint_S \psi_i(x,y)\ dx\ dy} \tag{2.22}$$

The *normalized mode intensity envelope*, a parameter invariant along z, is defined as:

$$\overline{\psi}_i(x,y) = \frac{\psi_i(x,y)}{\iint_S \psi_i(x,y)\ dx\ dy} \tag{2.23}$$

This procedure conveniently avoids having to solve the wave equation repeatedly along the waveguide amplifier to account for changes in optical power. Modal analysis of the waveguide is thus effectively separated from optical power analysis of the amplifier. The latter is the focus of the model developed in the next chapter; the former is an essential but independent step which serves as an input parameter for the amplifier simulation.

2.1.3 Photon Optics

In addition to electromagnetic theory, the particle nature of light completes the basic requirements to study optical amplifiers. Stated simply, light of frequency ν consists of streams of particles called *photons*, each with energy :

$$E = h\nu \tag{2.24}$$

where h=Planck's constant, named in honour of the physicist who originated the concept of quantizing radiant energy. The following definitions relate photon energy to electromagnetic intensity and power discussed in the previous section. The mean photon-flux density associated with monochromatic light of frequency ν is:

$$\phi(x,y) = \frac{I(x,y)}{h\nu} \qquad \text{(photons/sec-m}^2\text{)} \qquad (2.25)$$

The mean photon flux is :

$$\Phi = \iint_S \frac{I(x,y)}{h\nu}\,dx\,dy = \frac{P(z)}{h\nu} \qquad \text{(photons/sec)} \qquad (2.26)$$

2.2 Energy Levels of Atoms

Modern *quantum atomic theory* is also based on Planck's quantum hypothesis [17]. In Niels Bohr's model of the atom, electrons revolved in discrete orbits around the nucleus and electron transitions between orbits resulted in the emission or absorption of radiant energy in discrete units. In light of Heisenberg's Uncertainty Principle, which stated that it was impossible to establish the exact position of any particle, Max Born modified the atomic model by considering the wave nature of electrons. Born replaced the concept of discrete electron orbits with electron orbitals. The latter describes the probability of finding electrons in space. The behaviour of an electron of mass m and potential energy V is described by the complex wavefunction ψ, satisfying the time-independent Schrödinger equation [1]:

$$-\frac{\hbar^2}{2m}\nabla^2\psi(r) + V(r)\psi(r) = E\psi(r) \qquad \text{Eq. 2.27}$$

When applied to a real system (such as a hydrogen atom), solutions to the Schröndinger equation are obtained only at discrete values of energy E. For a system of multiple electrons, a generalized form of Eqn 2.27 is used and solutions result in energy levels which form densely packed bands. The lower energy levels are filled by core electrons but higher energy levels are only partially occupied, allowing for electron transitions and exchange of energy with the outside world (such as a photon). It is this photon-atom interaction that forms the basis for optical amplification.

2.3 Photon-Atom Interaction

2.3.1 Absorption, Stimulated Emission and Spontaneous Emission:

Atoms in a patricular energy level can absorb the energy of an incoming photon and move to higher energy level if the energy of the photon matches the difference in atomic energy levels : $E_2 - E_1 = h\nu = \frac{hc_o}{\lambda}$. The process is illustrated in Figure 2.4.

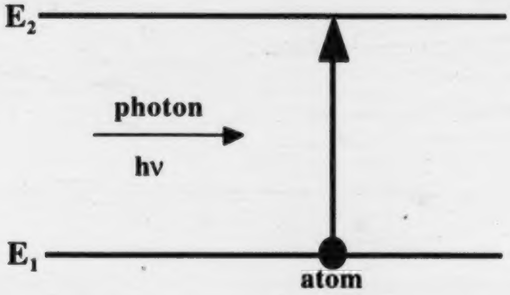

Figure 2.4 Absorption of photon energy by an atom

In the presence of light of wavelength λ_s (henceforth referred to as the "*signal*") and photon-flux density ϕ_s (photons/m^2-s), the probability density (1/s) for absorption is $W_{12} = \phi_s\, \sigma_{12}(\lambda_s)$. The parameter $\sigma_{12}(\lambda_s)$, defined as the *absorption transition cross-section*, is the effective area of the atom that is available to interact with photons. W_{12} is a measure of the rate at which photon-flux is intercepted by the atom. If the density of atoms in the lower energy level is N_1 (ions/m^3), the rate of absorption is $N_1 W_{12}$ (ions/m^3-sec).

Atoms could undergo downward transitions from level 2 to level 1 and release their energy in the form of photons. This event could either be triggered (*stimulated*) by the presence of existing signal photons or it may occur spontaneously. If stimulated, the emitted photons are clones of the original and have the same frequency and polarization characteristics. If spontaneous, the emitted photons have random characteristics. The two processes are illustrated in Figures 2.5 and 2.6, respectively.

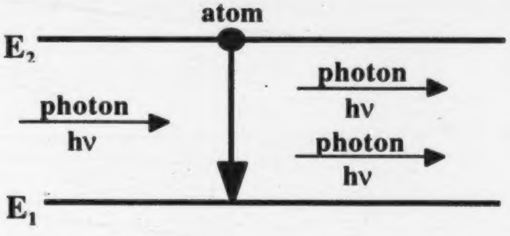

Figure 2.5 Stimulated emission of photon

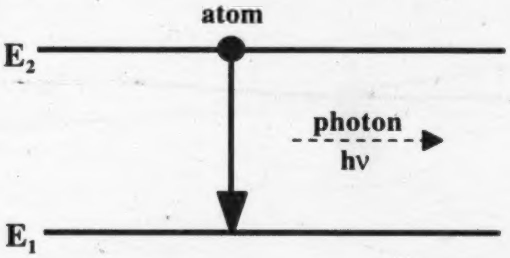

Figure 2.6 Spontaneous emission of photon

Stimulated emission results in a cascade of newly generated photons which add to the optical power of the signal. Spontaneous emission results in noise. The probability density for stimulated emission is $W_{21} = \phi_s\, \sigma_{21}(\lambda_s)$. If there are N_2 atoms/m^3 in the upper energy level, the rate of emission is N_2W_{21}. The emission cross-section $\sigma_{21}(\lambda_s)$ is typicaly lower than $\sigma_{12}(\lambda_s)$ but not significantly so. However, in thermal equilibrium, atoms are more likely to occupy the lower energy state than the higher energy state. This arises from the exponential Boltzmann Distribution for the probability of occupancy of energy levels [1]:

$$P(E_m) \propto e^{-E_m/k_B T} \qquad \text{for m=1,2....,} \tag{2.27}$$

where k_B=Boltzmann's constant, T=temperture, and the coefficient of proportionality is such that $\sum_m P(E_m) = 1$. In the absence of an external excitation source, N_1 is greater than N_2 at any given time. Thus, the probability of absorption is greater than emission, even though the probability density of the two events is almost the same.

The probability density for spontaneous emission is $A_{21} = 1/\tau_{21}$. The parameter τ_{21} (*metastable state or luminescence lifetime*) is the time-constant for the exponential decay of atoms from the upper level to the lower level. If there are N_2 atoms/m^3 ions in the upper level, the rate of spontaneous emission is given by N_2A_{21}.

2.3.2 Pumping and Population Inversion

An optical excitation source operating at a shorter wavelength λ_p (henceforth referred to as the "*pump*") can create a non-equilibrium condition by populating the higher energy states. In a three-energy-level laser system, atoms in the ground state absorb the energy of pump photons and are excited to level 3. In the presence of pump photon-flux density ϕ_p, the pumping rate is $R_{13} = \phi_p \sigma_{13}(\lambda_p)$. If there are N_1 atoms/m^3 in the ground state, the pumping rate is N_1R_{13}. The lifetime τ_{32} of level 3 is typically a few microseconds; so atoms in that level decay rapidly and non-radiatively down to level 2. The lifetime of level 2 is in the order of a few milliseconds (hence the name *metastable*), allowing for significant accumulation of atoms. In effect, the pump depletes the ground state and populates the metatable state, causing a *population inversion*. Under these non-equilibrium conditions, N_2 is greater than N_1 and the probability of stimulated emission of signal photons is higher than absorption.

2.3.3 Signal and Pump Propagation in an Amplifier

As light propagates in an amplifier, the photon flux densities change as a consequence of the photon-atom interactions discussed in Sections 2.3.1 and 2.3.2. To derive expressions for photon flux density as a function of position, consider an incremental cylinder of length dz inside an amplifier (three-energy-level) of finite length d and unit area, as shown in Figure 2.7. The signal photon flux density entering and exiting the cylinder is ϕ_s and $\phi_s+d\phi_s$, respectively. The pump photon flux density entering and exiting the cylinder is ϕ_p and $\phi_p-d\phi_p$, respectively.

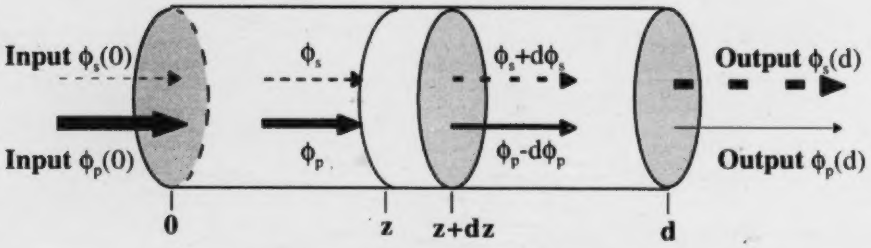

Figure 2.7 Change in photon flux densities due to photon-atom interaction

Hence, $d\phi_s$ and $d\phi_p$ are the incremental signal and pump photon flux densities emitted and absorbed inside dz, respectively. Since the transitions rates are known (from Section 2.3.2), $d\phi_s$ and $d\phi_p$ are given by :

$$d\phi_s = (N_2W_{21} - N_1W_{12})\, dz = (N_2\sigma_{21} - N_1\sigma_{12})\, \phi_s\, dz \qquad (2.28)$$

$$d\phi_p = -(N_1R_{13})\, dz = -(N_1\sigma_{13})\, \phi_p\, dz \qquad (2.29)$$

The wavelength dependence of ϕ is implied through subscripts. Equations 2.28 and 2.29 can be put in the form of first order differential equations:

$$\frac{d\phi_s(z)}{dz} = \gamma_s\, \phi_s(z) \qquad \text{where } \gamma_s = N_2\sigma_{21} - N_1\sigma_{12} \qquad (2.30)$$

$$\frac{d\phi_p(z)}{dz} = -\alpha_p\, \phi_p(z) \quad \text{where } \alpha_p = N_1\sigma_{13} \qquad (2.31)$$

γ_s and α_p are the gain and absorption coefficients, respectively. The solutions to Eqns. 2.30 and 2.31 describe the photon flux density as a function of amplifier position z. As an aside, it is worth noting that the gain coefficient depends on the population densities, which in turn depend on the photon flux density of the signal that is to be amplified. This is a cause for gain saturation in amplifiers, as will be discussed in the next chapter.

It is customary to write the signal and pump propagation equations in terms of the total optical power rather than photon flux density. Expressions relating photon flux density and power were given in Section 2.1.3.

$$\frac{dP_s(z)}{dz} = \gamma_s \, P_s(\mathrm{z}) \tag{2.32}$$

$$\frac{dP_p(z)}{dz} = -\alpha_p \, P_p(\mathrm{z}) \tag{2.33}$$

The solution to Eqns. 2.32 and 2.33 have an exponential form when γ_s and α_p are constants, as is the case here :

$$P_s(\mathrm{z}) = \mathrm{e}^{(\gamma_s z)} \tag{2.34}$$

$$P_p(\mathrm{z}) = \mathrm{e}^{(-\alpha_p z)} \tag{2.35}$$

The net signal gain, pump depletion, gain efficiency and pump efficiency for the amplifier are given by :

$$\text{Net Signal Gain} = 10 Log_{10}\left(\frac{\mathrm{P}_s(\mathrm{d})}{\mathrm{P}_s(0)}\right) \qquad \text{(dB)} \tag{2.36}$$

$$\text{Net Pump Depletion} = 10 Log_{10}\left(\frac{\mathrm{P}_p(\mathrm{d})}{\mathrm{P}_p(0)}\right) \qquad \text{(dB)} \tag{2.37}$$

$$\text{Gain Efficiency} = \frac{10 Log_{10}\left({}^{\mathrm{P}_s(\mathrm{d})}\!/_{\mathrm{P}_s(0)}\right)}{d} \qquad \text{(dB/cm)} \tag{2.38}$$

$$\text{Pump Efficiency} = \frac{10 Log_{10}\left({}^{\mathrm{P}_s(\mathrm{d})}\!/_{\mathrm{P}_s(0)}\right)}{P_p(0)} \qquad \text{(dB/mW)} \tag{2.39}$$

The concepts outlined in this chapter provide a basic foundation for modeling optical amplifiers.

Chapter 3 : Numerical Model for Rare-Earth-Doped Planar Optical Waveguide Amplifiers

In this chapter, the general concepts and equations outlined in Chapter 2 will be applied to the specific case of erbium/ytterbium co-doped waveguides, with appropriate modifications. The algorithm required to run the simulation will be presented in step-by-step form. The model will be verified against published numerical and experimental results. Since this is in some sense a "beam propagation" simulation, some of the equation variables will be tracked individually along a waveguide to garner a better understanding of the equations at work and to aid in the design of subsequent waveguide structures.

3.1 Energy Levels for Er^{3+} and Yb^{3+} in Glass Hosts

In glass, rare-earths such as erbium, ytterbium, neodymium and praseodymium exist in the trivalent state (Er^{3+}, Yb^{3+}, Nd^{3+}, Pr^{3+}) due to the removal of three electrons from the outer shells. For each of these rare-earth ions, the energy associated with a transition between two levels (within the 4*f* shell) matches the photon energy corresponding to important telecommunication wavelengths : 1.55 µm for Er^{3+} , 0.9-1.0 µm for Yb^{3+} and 1.3 µm for Nd^{3+} and Pr^{3+} [18,19].

The energy level diagram for Er^{3+} and Yb^{3+} is given in Figure 3.1. The labelling of each energy level (such as $^5I_{15/2}$, $^4I_{13/2}$ etc.) follows from the quantum numbers assigned to electrons in a given shell. The energy levels are numbered for ease of reference. The wavelength of light corresponding to the various energy level transitions are also indicated. The 975-985 nm wavelength region is the only absorption band shared by erbium and ytterbium. Since all of the rare-earth-doped devices investigated in this thesis were pumped in the 975-985 nm wavelength band, other absorption bands of erbium (800 nm, 1480 nm) were not considered. Table 3.1 summarizes all possible interactions between individual erbium/ytterbium ions and signal (λ=1.55µm) and pump (λ=0.98µm) photons. The radiative (stimulated emission, spontaneous emission and absorption) and non-radiative transition rates associated with each interaction are also listed.

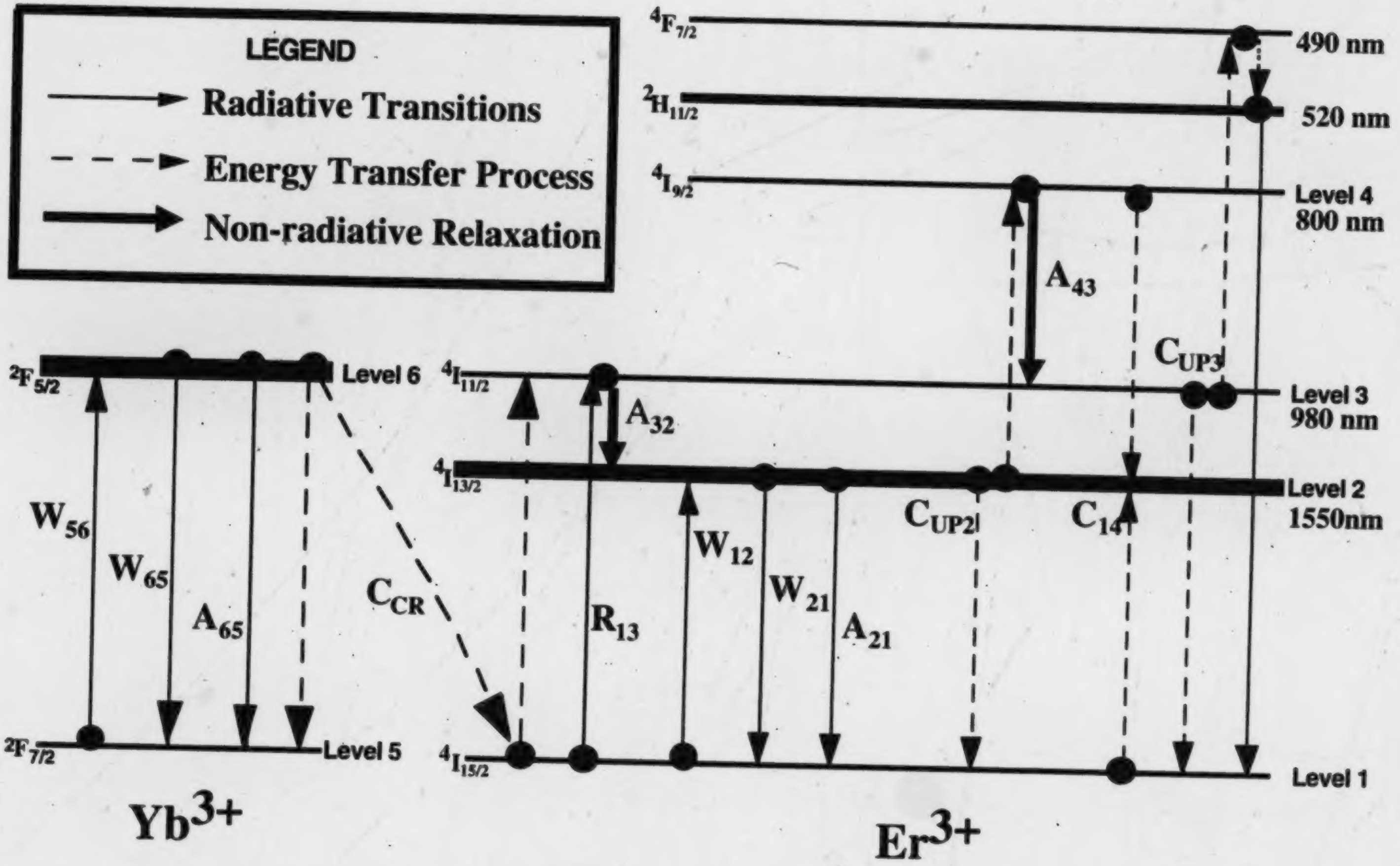
LEGEND
Radiative Transitions
Energy Transfer Process
Non-radiative Relaxation
$^4F_{7/2}$
$^2H_{11/2}$
$^4I_{9/2}$
490 nm
520 nm
Level 4
800 nm
A_{43}
C_{UP3}
$^2F_{5/2}$
Level 6
$^4I_{11/2}$
A_{32}
Level 3
980 nm
$^4I_{13/2}$
Level 2
1550nm
W_{56}
W_{65}
A_{65}
C_{CR}
R_{13}
W_{12}
W_{21}
A_{21}
C_{UP2}
C_{14}
$^2F_{7/2}$
Level 5
$^4I_{15/2}$
Level 1
Yb^{3+}
Er^{3+}

Figure 3.1 Energy Level Diagram for Er^{3+} and Yb^{3+} in glass hosts

From	To	Ion	$\lambda(\mu m)$	Nature of Transition	Rate of Transition $(1/s\text{-}m^3)$
Level 1	Level 2	Er^{3+}	1.55	Absorption	$N_1W_{12}=N_1\phi_s\sigma_{12}$
Level 2	Level 1	Er^{3+}	1.55	Stimulated Emission	$N_1W_{12}=N_2\phi_s\sigma_{21}$
Level 2	Level 1	Er^{3+}	1.55	Spontaneous Emission	$N_2A_{21}=N_2/\tau_{21}$
Level 1	Level 3	Er^{3+}	0.98	Absorption	$N_1W_{13}=N_1\phi_p\sigma_{13}$
Level 3	Level 2	Er^{3+}	N/A	Non-radiative Relaxation	$N_3A_{32}=N_3 / \tau_{32}$
Level 3	Level 1	Er^{3+}	0.98	Stimulated Emission	$N_3W_{31}=N_3\phi_p\sigma_{31}$
Level 5	Level 6	Yb^{3+}	0.98	Absorption	$N_5W_{56}=N_5\phi_p\sigma_{56}$
Level 6	Level 5	Yb^{3+}	0.98	Stimulated Emission	$N_6W_{65}=N_6\phi_p\sigma_{65}$
Level 6	Level 5	Yb^{3+}	0.98	Spontaneous Emission	$N_6A_{65}=N_6 / \tau_{65}$

Table 3.1 : Summary of basic transitions in Er^{3+} / Yb^{3+} co-doped glass.

Of the transitions listed in Table 3.1, only stimulated emission of pump photons from level 3 was assumed to be negligible (due to the short lifetime of that level). Table 3.1 summarizes transitions that occur between photons and individual rare-earth ions. In waveguides with high rare-earth dopant levels, energy transfer resulting from interaction between rare-earth ions becomes important. Energy transfer between two adjacent erbium ions, as well as between one erbium ion and one ytterbium ion, have to be accounted for. Another factor to consider is the broadening of the metastable state, which results in spontaneous emission of photons at wavelengths other than 1.55 µm. These issues are addressed in the next three sub-sections.

3.2 Pair-Induced and Co-operative Upconversion

Upconversion is the end result of energy transfer between erbium ions which are either physically paired or in close proximity. When the rare-earth dopant concentration in glass is high (> 10^{25} ions/m^3 or 0.1 wt%), erbium ions may pair up and form clusters of arbitrary size [20-23]. In hosts like silica, over 70% of erbium ions may belong to clusters at concentrations of 1 wt%. If two erbium ions within a cluster are excited to the metastable state, one ion (the donor) transfers its energy to the other (the acceptor). In that event, the donor relaxes non-radiatively to the ground state and the acceptor moves to an even higher energy state. The net result is the removal of both ions from the lasing level. The acceptor may return to the metastable state or it may undergo a downward transition from the higher state directly to the ground state, resulting in the spontaneous emission of a photon of shorter wavelength. In effect, a cluster of any size can sustain at most one ion in the metastable state. With proper choice of co-dopants, pair-induced upconversion can be neglected even for high erbium concentrations [24]. For the devices discussed in this thesis, clustering effects will not be considered.

Even if erbium ions are uniformly distributed in the host glass and are not physically paired, the distance between them may be short enough (< 0.4nm) to allow for ion-ion interaction and consequently, transfer of energy [25]. This form of co-operative upconversion increases linearly with erbium concentration and appears to place a fundamental limit to waveguide amplifier performance [26]. The extent of upconversion varies slightly for different rare-earth/host combinations. The following coefficients describe the rate of upconversion and are typically determined by fitting to experimental data: C_{UP2} (when donor and acceptor are in level 2), C_{UP3} (when donor and acceptor are in level 3), and C_{14} (cross-relaxation, when donor is in level 4 and acceptor is in level 1) [27]. Of the three, co-operative upconversion from level 2 is most prevalent, given the high density of ions in that level under conditions of strong pumping. Levels 3 and 4 are sparsely populated owing to their short lifetimes. Nevertheless, all three transitions will be considered in this model and are summarized in Table 3.2.

Donor		Acceptor		Nature of Transition	Transition rate (1/s-m^3)
From	To	From	To		
Level 2	Level 1	Level 2	Level 4	Upconversion	$C_{UP2}N_2N_2$
		Level 4	Level 3	Non-radiative Relaxation	N_4 / τ_{43}
Level 3	Level 1	Level 3	$^4F_{7/2}$	Upconversion	$C_{UP3}N_3N_3$
		$^2H_{11/2}$	Level 1	Spontaneous Emission (λ=520nm)	Not considered
Level 4	Level 2	Level 1	Level 2	Cross-relaxation	$C_{14}N_1N_4$

Table 3.2 - Transitions resulting from interaction of adjacent Er^{3+} ions

3.3 Ytterbium Sensitization

Ytterbium shares some of the transitions and energy transfer characteristics of erbium [18,20,24]. Ytterbium ions also absorb light of wavelength $\lambda = 0.98$ µm. In fact, the absorption transition cross-section $\sigma_{56}(\nu_p)$ for ytterbium can be up to a factor of eight higher that its erbium counterpart, yielding significantly higher pumping rates [28]. This advantage is tempered slightly by a shorter metastable state lifetime (< 2 ms). Once excited to its metastable state (Level 6), a ytterbium ion (donor) can transfer its energy to an erbium ion (acceptor) in Level 1. This results in the acceptor moving up to Level 3 (and then rapidly down to Level 2) and the donor relaxing to its ground state (Level 5). A cross-relaxation coefficient C_{cr} is defined (similar to the upconversion coefficients) to estimate the energy transfer rates between ytterbium and erbium [20]. If there are N_6 ytterbium ions/m^3 in level 6 and N_1 erbium ions/m^3 in level 1, the rate of cross-relaxation is $C_{cr}N_1N_6$. C_{cr} has been shown to increase linearly with ytterbium up to concentrations of 10 x 10^{26} ions/m^3. At higher concentrations, energy transfer between ytterbium ions becomes a factor [20].

Energy transfer also occurs in the reverse direction (where an erbium ion in level 3 is the donor and a ground-state ytterbium ion is the acceptor) but at much lower rates owing to the sparse population of level 3. Hence, the back-transfer of energy from erbium to ytterbium will not be considered in the model. The ability to indirectly pump erbium ions through ytterbium sensitization compliments the direct pumping scheme. This facilitates greater population inversion and consequently, amplification.

3.4 Amplified Spontaneous Emission (ASE) Spectrum

In glass hosts, the Stark effect splits the major energy levels into sublevels. For instance, the broadening of the Er^{3+} metastable state due to Stark effects can be significant enough to allow for spontaneous emission at wavelengths down to 1.48 μm. Hence, spontaneous emission of photons occurs over a spectral range of about 100 nm, centered at 1.55 μm. It should be noted that the presence of the sublevels does not invalidate the three energy level assumption. Thermal equilibrium ensures a constant population distribution (Boltzmann) within the sublevels [18].

To account for the full spectrum of amplified spontaneous emission (ASE), the model will consider 113 wavelength slots (from λ_1=1.475 μm to λ_{113}=1.587 μm, each 1nm in width) and compute the change in optical power within each slot. For all 113 wavelength slots, the normalized intensity envelope will be assumed to be the same as that of the signal (since $\overline{\psi}_k$ is weakly dependent on wavelength). However, the emission transition cross-section is a strong function of wavelength and has to be considered separately for each ASE wavelength slot. Determining the parameter $\sigma_{21}(\lambda_k; k=1,...,113)$ experimentally is beyond the scope of this thesis. Instead, transition cross-section data which is representative of a typical erbium-doped silicate glass will be used from the literature [25]. This data is plotted in Figure 3.2 and will be used for all following simulations.

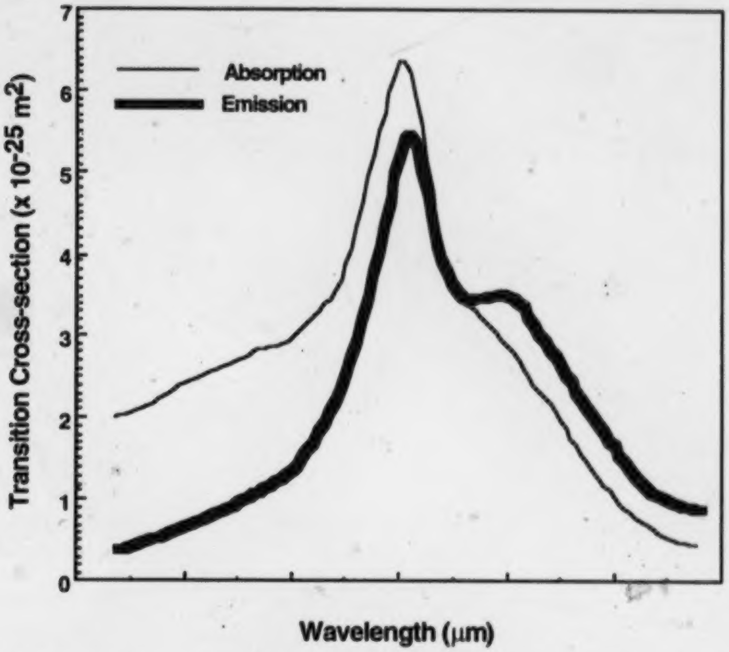

Figure 3.2 Emission and absorption transition cross-section for a typical Er-doped silicate glass [25].

3.5 Model Algorithm

The following steps are required to compute the change in signal, pump and ASE power along a waveguide amplifier. Figure 3.3 may serve as a useful pictorial guide. The equations used and the waveguide regions over which they are applicable are matched by a color code.

1) For a given waveguide structure, the wave equation is solved and the normalized signal and pump mode intensity envelopes $\overline{\psi}_s(x,y)$ and $\overline{\psi}_p(x,y)$ are generated (as described in Sections 2.1.2.2 and 2.1.2.3).

2) The optical signal power $P_s(0)$ and pump power $P_p(0)$ launched into the waveguide, length of the waveguide, concentration of rare-earth dopants in the waveguide and all material parameters (τ, σ and C) are provided as input to the model.

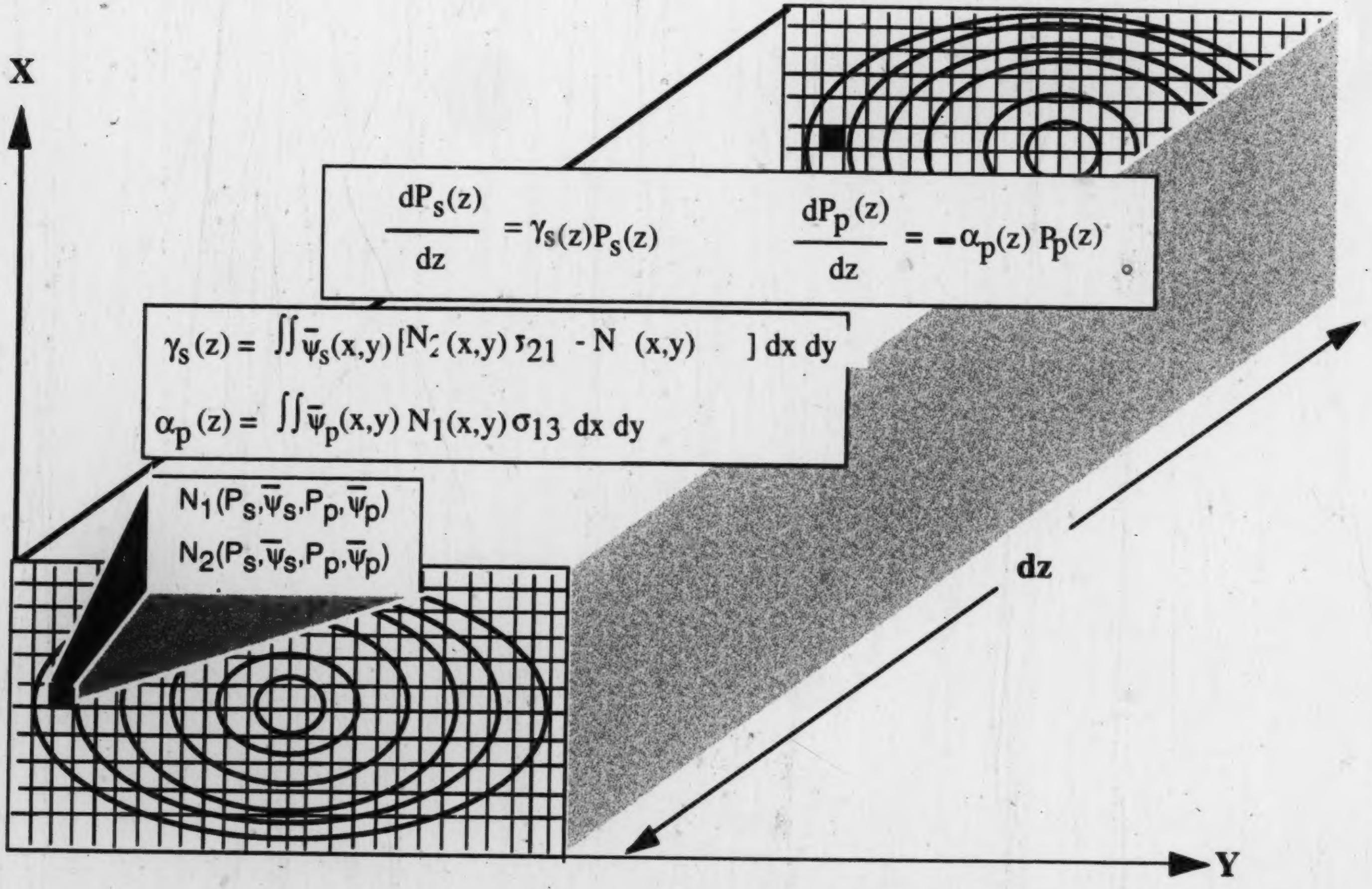

X
dPs(z)/dz = γs(z)Ps(z)
dPp(z)/dz = −αp(z) Pp(z)
γs(z) = ∬ψ̄s(x,y) [N2 (x,y) σ21 - N (x,y)] dx dy
αp(z) = ∬ψ̄p(x,y) N1(x,y) σ13 dx dy
N1(Ps,ψ̄s,Pp,ψ̄p)
N2(Ps,ψ̄s,Pp,ψ̄p)
dz
Y

Figure 3.3 Pictorial illustrationof rare-earth-doped waveguide amplifier model

3) The waveguide cross-section is divided and analysed in small rectangular elements of area $\Delta x \Delta y$. Waveguide symmetry may be taken advantage of by identifying and counting identical elements.

4) The local intensities $I_s(x,y)$ and $I_p(x,y)$ within each element are computed by inserting $P_s(z)$, $\overline{\psi}_s(x,y)$, $P_p(z)$ and $\overline{\psi}_p(x,y)$ into Eqn. 2.22.

5) Within each element, the probability densities for all atomic transitions (stimulated emission, spontaneous emission, absorption, and non-radiative relaxation) are evaluated by inserting $I_s(x,y)$ and $I_p(x,y)$ into the expressions for W's, A's and R (given in Sections 2.3.1 and 2.3.2). For the case of W_{12} and W_{21}, inclusion of the full spectrum of forward-travelling ASE requires the following modification [29]:

$$W_{12} = I_s(\lambda_s)\frac{\sigma_{12}(\lambda_s)}{h\nu_s} + \sum_{k=1}^{113} I_{ASE+}(\lambda_k)\,\frac{\sigma_{12}(\lambda_k)}{h\nu_k} \tag{3.1}$$

$$W_{21} = I_s(\lambda_s)\frac{\sigma_{21}(\lambda_s)}{h\nu_s} + \sum_{k=1}^{113} I_{ASE+}(\lambda_k)\,\frac{\sigma_{21}(\lambda_k)}{h\nu_k} \tag{3.2}$$

The second term on the right-hand side is the net contribution from forward-travelling ASE. The spatial (x,y) dependence of I_s, I_{ASE+}, W_{12} and W_{21} was not explicitly stated.

6) Within each element, the steady-state population densities (rare-earth ions/m^3) $N_1(x,y)$, $N_2(x,y)$,...,$N_m(x,y)$ are computed for each of the rare-earth energy levels 1,2,...,m. This is achieved by considering all of the transitions listed in Tables 3.1 and 3.2 together and writing a set of rate equations (Eqns. 3.3-3.8). These equations describe the rate at which ions are being added to and depleted from each of the energy levels (levels 1-4 for Er^{3+} and levels 5 & 6 for Yb^{3+}). A factor of two appears in some of the rate equations since two ions are removed from that energy level in the event of co-operative energy transfer. In steady-state, the time rate of change of population density is zero. Unlike a laser, an optical

amplifier does not require transient analysis.

$$\frac{\partial N_1}{\partial t} = -W_{12}N_1 + A_{21}N_2 + W_{21}N_2 - R_{13}N_1 + C_{UP2}N_2N_2 \\ - C_{14}N_1N_4 + C_{UP3}N_3N_3 - C_{CR}N_1N_6 = 0 \tag{3.3}$$

$$\frac{\partial N_2}{\partial t} = W_{12}N_1 - A_{21}N_2 - W_{21}N_2 + A_{32}N_3 - 2C_{UP2}N_2N_2 \\ + 2C_{14}N_1N_4 = 0 \tag{3.4}$$

$$\frac{\partial N_3}{\partial t} = R_{13}N_1 - A_{32}N_3 + A_{43}N_4 - 2C_{UP2}N_3N_3 \\ + C_{CR}N_1N_6 = 0 \tag{3.5}$$

$$N_{erb} = N_1 + N_2 + N_3 + N_4 \tag{3.6}$$

$$\frac{\partial N_5}{\partial t} = -W_{56}N_5 + A_{65}N_6 + W_{65}N_6 + C_{CR}N_1N_6 = 0 \tag{3.7}$$

$$N_{yb} = N_5 + N_6 \tag{3.8}$$

Since the total erbium ion concentration N_{Erb} and ytterbium ion concentration N_{Yb} are known, there are six unknown quantities N_1, N_2, N_3, N_4, N_5 and N_6 in six equations. A Newton-Raphson algorithm was required to solve this system of nonlinear equations. Details are given in Appendix A.

7) Next, the contribution of each element to the net gain and absorption coefficient is computed (using Eqns. 2.30 and 2.31). Integrating over the waveguide cross-section yields the net gain and absorption coefficients.

$$\alpha_{13}(z,\lambda_p) = \iint_{x\,y} \overline{\psi}_p(x,y)\,\sigma_{13}(\lambda_p)\,N_1(x,y)\,dx\,dy \tag{3.9}$$

$$\alpha_{56}(z,\lambda_p) = \iint_{x\,y} \overline{\psi}_p(x,y)\,\sigma_{56}(\lambda_p)\,N_5(x,y)\,dx\,dy \tag{3.10}$$

$$\gamma_{65}(z,\lambda_p)=\int_x\int_y \overline{\psi}_p(\mathrm{x,y})\,\sigma_{65}(\lambda_p)\,N_6(\mathrm{x,y})\,dx\,dy \tag{3.11}$$

$$\gamma_{12}(z,\lambda_s)=\int_x\int_y \overline{\psi}_s(\mathrm{x,y})\,\sigma_{12}(\lambda_s)\,N_1(\mathrm{x,y})\,dx\,dy \tag{3.12}$$

$$\gamma_{21}(z,\lambda_s)=\int_x\int_y \overline{\psi}_s(\mathrm{x,y})\,\sigma_{21}(\lambda_s)\,N_2(\mathrm{x,y})\,dx\,dy \tag{3.13}$$

$$\gamma_{21}(z,\lambda_k)=\int_x\int_y \overline{\psi}_s(\mathrm{x,y})\,\sigma_{21}(\lambda_k)\,N_2(\mathrm{x,y})\,dx\,dy \tag{3.14}$$

8) The following signal, pump and ASE propagation equations are solved over a finite step Δz (using Euler's method) to obtain the change in optical power:

$$\frac{dP_p(z,\lambda_p)}{dz}=-\left[\alpha_p+l_p\right]P_p(z,\lambda_p) \quad \text{where} \quad \alpha_p=\alpha_{13}+\alpha_{56}-\gamma_{65} \tag{3.15}$$

$$\frac{dP_s(z,\lambda_s)}{dz}=\left[\gamma_s-l_s\right]P_s(z,\lambda_s) \quad \text{where} \quad \gamma_s=\gamma_{21}(\lambda_s)-\gamma_{12}(\lambda_s) \tag{3.16}$$

$$\begin{aligned}\frac{dP^{+}_{ASE}(z,\lambda_k)}{dz}&=\left[\gamma 21(z,\lambda_k)-\gamma 12(z,\lambda_k)\right]P^{+}_{ASE}(z,\lambda_k)\\&\quad+h\nu_k\Delta\nu_k\gamma 21(z,\lambda_k)\end{aligned} \tag{3.17}$$

In addition to the gain and absorption coefficients, an excess loss factor was introduced into both the signal and pump propagation equations (l_s and l_p, respectively). This accounts for losses due to waveguide imperfections (such as sidewall roughness and scattering sites). In the ASE propagation equation, the second term on the right-hand-side is a distributed source term used as a seed for the generation of ASE [18,30].

9) With the updated optical power, the simulation is advanced by Δz along z and steps 1-8 are repeated. This cyclical procedure continues over the length of the waveguide.

10) At the end of the waveguide, the net signal gain and pump attenuation are evaluated using Eqns. 2.36 and 2.37.

3.6 Validation of Model for Er-doped Waveguide Amplifier

One of the first demonstrations of a planar Er^{3+}-doped silica waveguide amplifier was reported by NTT [31]. In their work, Flame Hydrolysis Deposition (FHD) and Reactive Ion Etching (RIE) were used to fabricate a ridge waveguide which was 8 μm wide, 7μm high and 19.4 cm long. The erbium ion concentration was estimated to be 0.55 wt%. The waveguide cross-section and the corresponding transverse electric-field (TE) contours for signal $\psi_e(\lambda_s,x,y)$ and pump $\psi_e(\lambda_p,x,y)$ modes are illustrated in Figure 3.4.

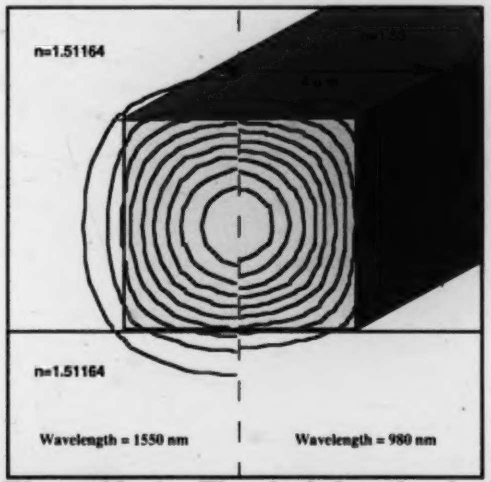

Figure 3.4 Ridge Waveguide 1. The shaded region is the Er-doped SiO_2 core with index n=1.53. The core is surrounded on all sides by SiO_2 cladding of index n=1.51164. The TE field contours for the signal (λ_s=1550nm) and pump (λ_s=980nm) mode are shown on the left and right, respectively. The contours represent 90% to 10% of peak amplitude.

The structure supports only a single guided mode at both signal and pump wavelengths. The refractive index profile [1] is such that the electric field is strongly confined to the Er-doped SiO_2 core; roughly 81% of the signal mode-field and 91% of the pump mode-field overlaps with the Er-doped core. Unlike fibre amplifiers, the overlap percentages do not figure explicitly in any of the model equations for planar waveguide amplifiers. However, it is a useful quantitative measure of light confinement and will be provided for all of the waveguides considered in this thesis. The overlap factor impacts both the optimum length of the amplifier and the pumping efficiency.

---

[1] Only the index difference between core and cladding was provided in [31]; not the actual indices.

The mode intensity contours $\psi_i(\lambda_s,x,y)$ and $\psi_i(\lambda_p,x,y)$ were obtained by squaring the electric field (Eqn. 2.20). The *modal area* of the intensity is of interest for normalization. The modal areas for signal and pump are 26.5 and 22.2 μm^2, respectively. The normalized intensity $\overline{\psi}_i(\lambda_s,x)$ and $\overline{\psi}_i(\lambda_p,x)$ at one specific point (the center) along the y-axis are shown in Figure 3.5. Henceforth, the notation for normalized intensity will be simplified to $\overline{\psi}_s$ and $\overline{\psi}_p$ for signal and pump, respectively.

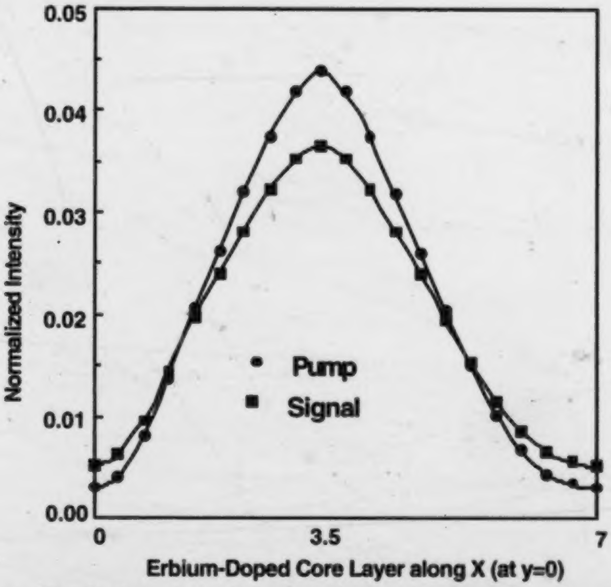

Figure 3.5 Normalized signal and pump intensity profile along the center of Ridge Waveguide 1, within the Er-doped SiO_2 core.

The normalized pump intensity exceeds that of the signal only near the center of the waveguide. Since the atomic transition rates and gain/absorption coefficients depend strongly on $\overline{\psi}_s$ and $\overline{\psi}_p$ [Eqns. 3.1-3.14], it is significant that their relative magnitudes vary across the waveguide cross-section. For a given optical pump power, the pump intensity may be too weak to invert the erbium population near the outer edges of the erbium-doped core. If that is the case, signal photons are more likely to be absorbed at that location. This justifies the need for analysing the waveguide in finite segments.

Simulating the gain characteristics of the waveguide shown in Figure 3.4 requires knowledge of the following parameters : lifetime of energy levels, transition cross-sections, background losses and upconversion coefficients. Since these parameters were not determined experimentally, Di Pasquale et al. have estimated them by observing the best fit to the experimental data [25]. The estimated values are listed in Table 3.3 and are applicable only for this specific case. These estimates are typical of erbium-doped fiber amplifiers. Given the low erbium content and similarity in glass chemistry (fiber amplifiers are also fabricated by Flame Hydrolysis and consist predominantly of silica), it is reasonable to expect the material parameters to be similar.

τ_{21}	11 ms
$\tau_{43} = \tau_{32}$	1 ns
$l_s=l_p$	0.2 dB/cm
$\sigma_{13}(\lambda_p)$	2.0 x 10^{-25} m^2
$C_{UP2}=C_{UP3}=C_{14}$	3.5 x 10^{-23} m^3/s

Table 3.3 Material parameters used for the simulation of Ridge Waveguide 1 [25].

For Ridge Waveguide 1, the predicted variation in signal transmission (or signal gain) as a function of input pump power is plotted in Figure 3.6 and compared with experimental results reported by NTT. It is clear that there is satisfactory agreement between the model developed in this chapter and NTT's experiment. The model developed by Di Pasquale predicted similar results. The model does over-estimate the gain slightly, particularly at high pump powers. Onset of pair-induced upconversion, a factor not accounted for in the model, may account for this discrepancy. Since this was not a multicomponent glass, erbium ion pairs may have formed even at these low dopant levels. Gain reduction due to clustering would manifest itself more clearly at high pump powers, under conditions of maximum population inversion.

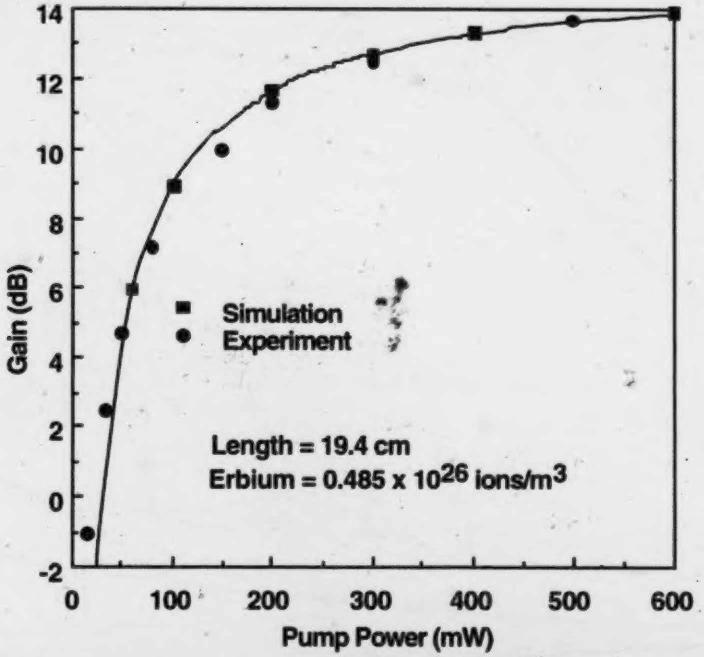

Fig. 3.6 Signal Gain vs. Pump Power for Ridge Waveguide 1. Comparison of numerical model developed in this chapter and experimental results from [31]. $P_s(0)=1\mu W$; $L = 19.4$ cm; $N_{Erb} = 0.485 \times 10^{26}$ iosn/m^3.

At high pump powers, the signal gain saturates when all of the erbium ions are in the metastable state and gainfully contributing to stimulated emission. With the population fully inverted in this device, there is no further room for improvement in performance. A plot of signal gain as a function of waveguide length (Figure 3.7) reveals a linear relationship. This suggests that signal gain can be increased by using a longer device. However, the linear relationship between gain and waveguide length does not extend indefinitely. At a certain length, the pump power would fall below the threshold required to sustain population inversion. The optimum length for the amplifier would be precisely where the pump is at threshold. Beyond optimum length, the signal would be re-aborbed by ground-state erbium ions. This delicate balance between signal gain, waveguide length, input pump power and pump depletion is an important design consideration for any optical amplifer.

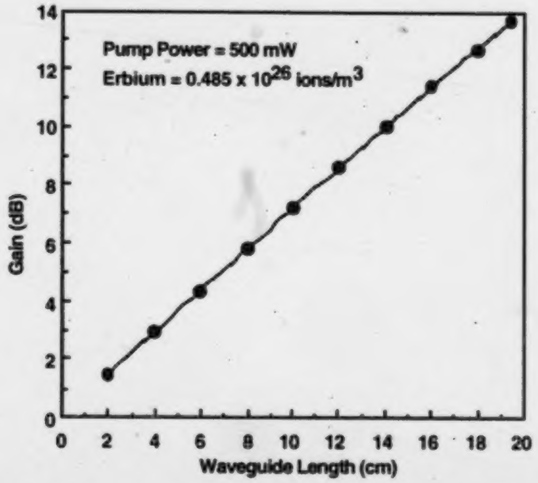

Figure 3.7 Signal Gain vs. Waveguide Length for Ridge Waveguide 1; $P_s(0)=1\mu W$; $P_p(0) = 500$ mW; $N_{Erb} = 0.485 \times 10^{26}$ ions/m^3.

Pump depletion as a function of input pump power is plotted in Figure 3.8. It is evident that the pump transmission also varies with input pump power. Implicit in that statement is information about population inversion. At low pump powers, the population inversion is weak and erbium ions in the ground state outnumber those at higher levels. Consequently, the overall rate of pump absorption (in dB/cm) is higher at low powers than under strong population inversion ("pump bleaching").

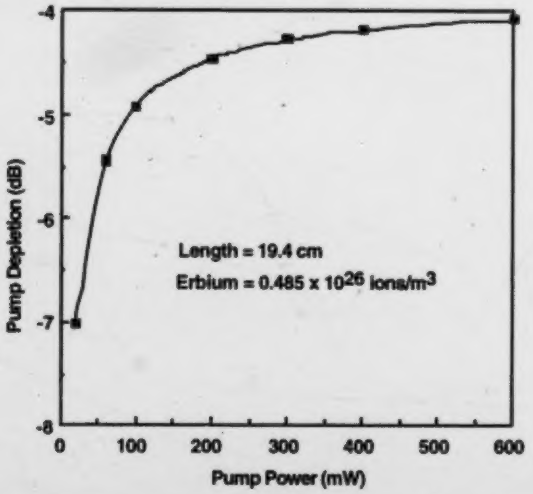

Figure 3.8 Pump Depletion vs. Input Pump Power for Ridge Waveguide 1; $P_s(0) = 1\mu W$; L = 19.4 cm; $N_{Erb} = 0.485 \times 10^{26}$ ions/m^3.

Signal gain also saturates when the signal power level approaches that of the pump. If this were to occur (either due to a high input signal power or as a result of amplification over extended lengths), the atomic transition rates between the ground state and metastable state would rival that between the ground state and the pumping level. This effectively negates the function of the pump, clamps the population inversion at a level well below its maximum and saturates the gain. Gain saturation behaviour due to signal strength is illustrated in Figure 3.9. The signal power is denoted in units of dBm, keeping with conventional notation [18].

$$P_{dBm} = 10Log_{10}P_{Watts} - 10Log_{10}(10^{-3})$$

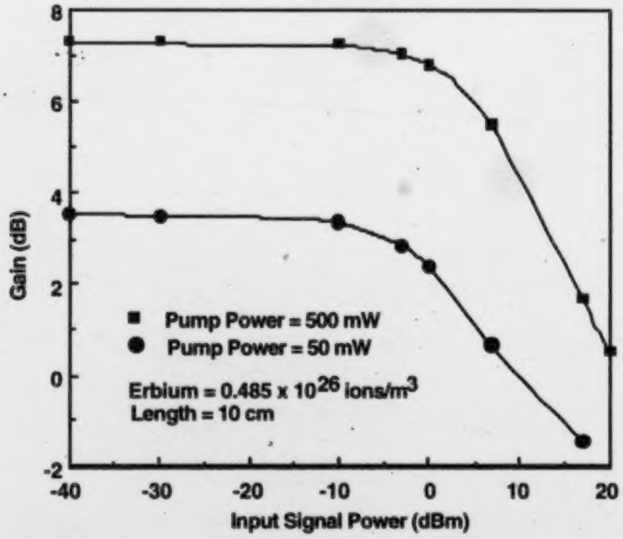

Figure 3.9 Signal Gain vs. Input Signal Power for Ridge Waveguide 1; $P_p(0)$ = 50, 500 mW; L = 10 cm; N_{Erb} = 0.485 x 10^{26} ions/m^3.

At signal power levels below -10 dBm (100 μW), the signal gain remains constant. For both high and low pump powers, the onset of gain saturation is evident only when the input signal power exceeds -10 dBm. For input signal powers approaching 20 dBm (100mW), the gain is reduced significantly. In fiber amplifiers, even a small input signal may be amplified over long distances and enter the saturation regime. Hence, it is customary to plot gain as a function of output signal power. Since planar Er-doped waveguide amplifiers are designed to be short in length and operated at high pump powers, this type of gain saturation can be neglected for applications other than power amplification. In this thesis, an input signal power of 1μW (unsaturated gain regime) will be assumed for the purposes of simulation

3.7 Validation of Model for Er/Yb co-doped Waveguide Amplifier

There have been many successful demonstrations of Er/Yb co-doped planar waveguide amplifiers [32-34]. However, the waveguide structures used in these experiments invariably have a graded refractive-index profile typical of diffusion / ion-exchange processes. There have not been any reports of Er/Yb co-doped planar waveguide amplifiers with discrete, dielectric layers. Hence, to test the model in the presence of ytterbium, Di Pasquale's model was used as the benchmark. The waveguide structure used by Di Pasquale to verify his erbium/ytterbium model is shown in Figure 3.10, along with the electric-field contour lines.

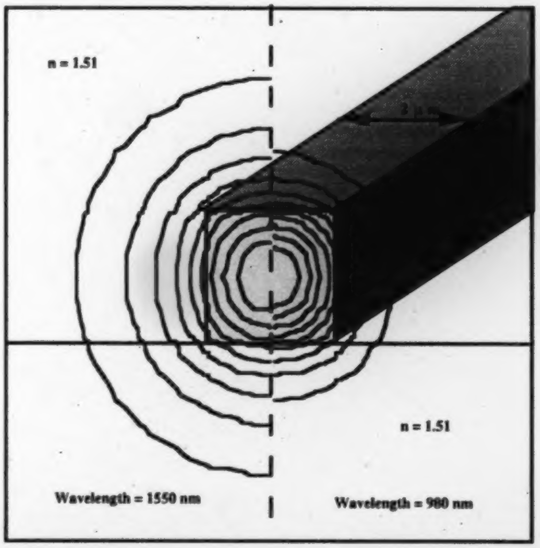

Figure 3.10 Ridge Waveguide 2. The shaded region is the Er/Yb co-doped core with index n=1.55. The core is surrounded on all sides by cladding of index n=1.51. The TE mode field contours for the signal (λ_s=1550nm) and pump (λ_s=980nm) are shown on the left and right, respectively.

The waveguide is singlemoded at both signal and pump wavelengths. The signal and pump overlap factors are Γ_s=30% and Γ_p=57%, respectively. The signal and pump modal intensity areas are 4.52 and 2.57 μm^2, respectively. Normalized intensity profiles for signal and pump along the center of the core are shown in Figure 3.11.

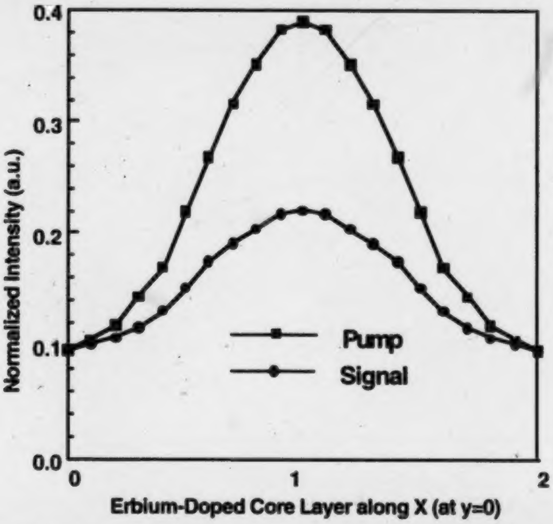

Figure 3.11 Normalized signal and pump intensity profile along the center of Ridge Waveguide 2, within the Er/Yb co-doped core.

The normalized pump intensity is higher than the normalized signal intensity at all points within the core, which was not the case in Ridge waveguide 1. This lowers the threshold pump power required to sustain population inversion. However, photon/atom interaction is reduced since a significant percentage of light propagates outside the core. Hence, there is a trade-off between the "quantity" and "quality" of the overlap.

Table 3.4 lists the material parameter values used by Di Pasquale in his model [20,24]. Although some of them are open to debate (particularly the assumption that the cross-relaxation coefficient C_{CR} is independent of ytterbium concentration), they will be used here for the sake of consistency. Di Pasquale assumes the excess loss factor to increase with N_{Erb} and N_{Yb}. For N_{erb}= 0.1-2.0 (in wt%) and N_{yb}= 1.0-20 (in wt%),

$$l_s = 7.717 + (2.126\ N_{erb}) + (0.29053\ N_{yb}) \qquad 1/m$$

$$l_p = 9.834 + (2.7\ N_{erb}) + (0.3696\ N_{yb}) \qquad 1/m$$

τ_{21}	11 ms
τ_{65}	1.5 ms
$\tau_{43} = \tau_{32}$	1 ns
$\sigma_{13}(\lambda_p)$	2.0 x 10^{-25} m^2
$\sigma_{56}(\lambda_p) = \sigma_{65}(\lambda_p)$	2.5 x 10^{-25} m^2
$C_{UP2}=C_{UP3}=C_{14}$	$[2.25N_{erb} - 0.64]$ x 10^{-23} m^3/s N_{erb} in wt%
C_{CR}	5.0 x 10^{-21} m^3/s

Table 3.4 Material parameters used for the simulation of Ridge Waveguide 2 [20,24]

Di Pasquale's model includes the option of introducing a counter-propagating pump from the opposite end of the waveguide. This is intended to compensate for the high rates of pump depletion commonly observed in ytterbium-doped waveguides. The model developed here does not consider counter-propagation of pump since it would necessitate an iterative algorithm that is computationally intensive. Hence, there are discrepancies in the computed signal gain between the two models. However, the functional form of the plots are similar.

Signal gain as a function of input pump power is plotted in Figure 3.12 for an amplifier that is 5 cm long and doped with 2.0 x 10^{26} erbium ions/m^3 (~ 2 wt%). The simulation was performed with and without ytterbium to highlight its impact. With ytterbium present (10 x 10^{26} ions/m^3), the amplifier performance improves on all fronts - maximum gain, minimum pump power required for signal transparency (0dB), pumping efficiency, etc. The signal gain saturates beyond 150 mW, indicating that population inversion has been maximized. In the absence of ytterbium, the pumping scheme is too weak to compensate for the depletion of the metastable state (due to upconversion). Hence, full inversion is never attained, even for pump powers exceeding 200 mW. At low pump powers, signal transmission actually improves in the absence of ytterbium. This is due to the excess loss factor, which was assumed to increase in the presence of ytterbium. The excess loss factor dominates the gain coefficient when the pump power is below threshold.

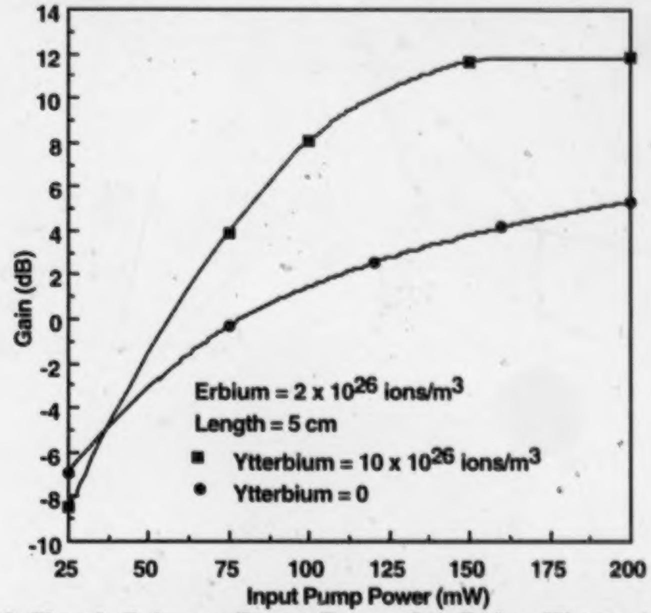

Figure 3.12 Signal Gain vs. Pump Power for Ridge Waveguide 2; L = 5 cm; N_{Erb} = 2 x 10^{26} ions/m^3; N_{Yb} = 0, 10 x 10^{26} ions/m^3.

To further illustrate the consequences of ytterbium co-doping, Figure 3.13 examines its impact on signal gain over a range of erbium dopant concentrations.

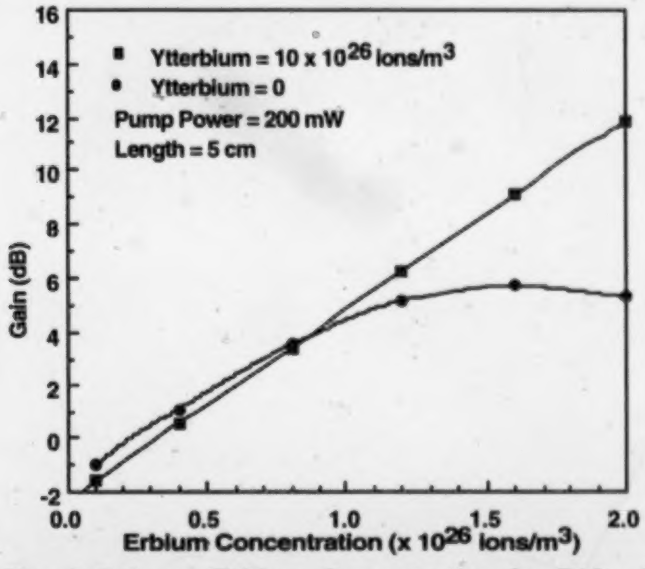

Figure 3.13 Signal Gain vs. Erbium Concentration for Ridge Waveguide 2; $P_p(0)$ = 200 mW; L = 5 cm; N_{Yb} = 0, 10 x 10^{26} ions/m^3.

At low erbium concentrations, upconversion is not a serious detriment and the amplifier performs better without ytterbium (again, excess loss due to addition of ytterbium outweighs its positive contribution). As the concentration of erbium increases, upconversion effects become increasingly pronounced and are mitigated only in the presence of ytterbium. For an erbium concentration of 2.0 x 10^{26} ions/m^3, ytterbium co-doping nets a gain improvement of 120%; quite significant over such a short length.

One of the drawbacks of ytterbium co-doping is the rapid depletion of the pump. This is true over the entire range of erbium concentrations but is particularly severe when combined with high erbium concentrations (Figure 3.14).

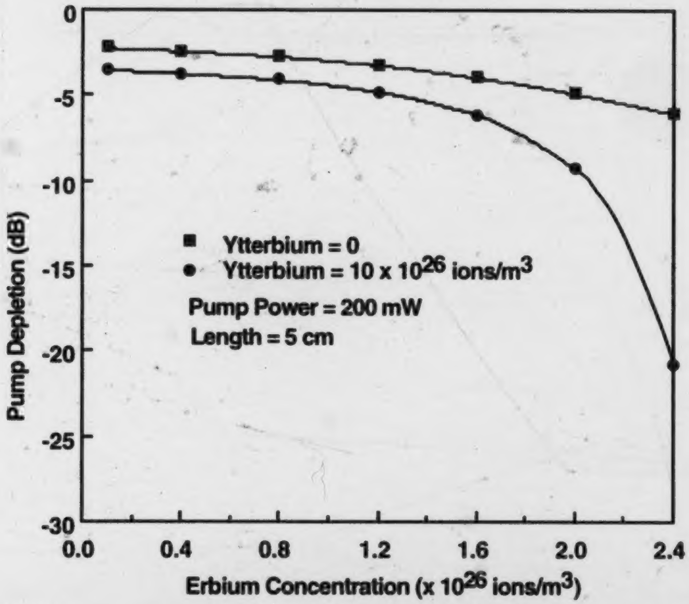

Figure 3.14 Pump Depletion vs. Erbium Concentration for Ridge Waveguide 2; $P_p(0)$ = 200 mW; L = 5 cm; N_{Yb} = 0, 10 x 10^{26} ions/m^3.

Even with high input pump powers, severe pump depletion limits the amplifier length to a few centimeters. Figure 3.15 illustrates the evolution of signal gain along the waveguide for a total input pump power of 300mW. The discrepancy between these curves and Di Pasquale's are noticeable because bi-directional pumping allows for a more even distribution of power along the waveguide (consequently, the optimum amplifier length can be extended). A maximum signal gain of 18 dB is predicted over 8 cm with 300 mW of pump power launched from one end; Di Pasquale's model predicts a gain of 26 dB over 12 cm with 150 mW of pump power launched from each end.

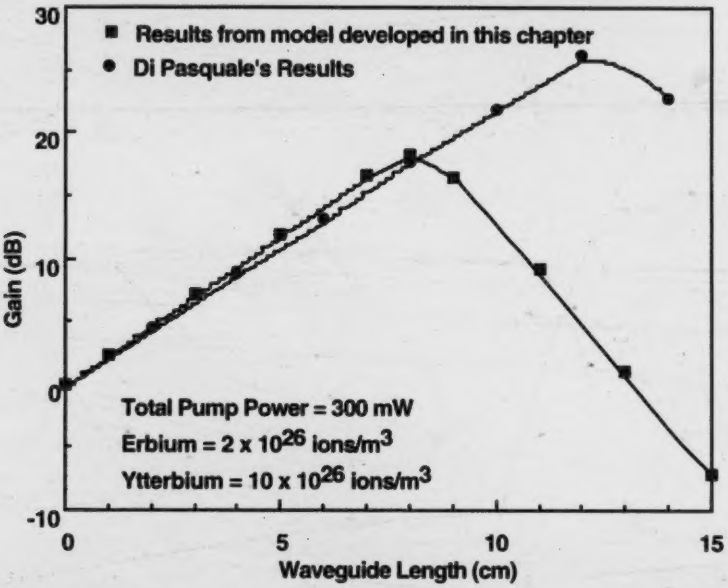

Figure 3.15 Signal Gain vs. Waveguide Length for Ridge Waveguide 2; P_p=300 mW; N_{Erb} = 2 x 10^{26} ions/m^3; N_{Yb} = 10 x 10^{26} ions/m^3.

3.8 Material Parameters

To reiterate, there appears to be significant discrepancies between some of the assumptions and material parameter values used by Di Pasquale and other published manuscripts. For instance, Veasey et al [35] were able to correlate theory to experiment only by assuming a linear relationship between the cross-relaxation coefficent C_{CR} and ytterbium concentration. More importantly, their estimate of C_{CR} was two orders of magnitude lower than Di Pasquale's. The emission/absorption cross-section data for ytterbium also differs widely within the literature, due in large part to the different glasses involved. As for the excess loss factor, there is no experimental evidence to support the severe concentration dependence and high losses assumed by Di Pasquale. As the state of this art evolves, a consensus is likely to emerge on these issues.

Two of the rare-earth-doped glasses used in this thesis were obtained from the same manufacturer who supplied Veasey. Hence, Veasey's estimates will be the primary source of reference for simulation purposes. They are listed in Table 3.5 and will be used for all further simulation work.

τ_{21}	11 ms
τ_{65}	2.0 ms
τ_{32}	10 μs
τ_{43}	1 ns
$\sigma_{13}(\lambda_p)$	1.1×10^{-25} m^2
$\sigma_{56}(\lambda_p)$	8.2×10^{-25} m^2
$\sigma_{65}(\lambda_p)$	8.1×10^{-25} m^2
l_s	0.15 dB/cm
l_p	0.30 dB/cm
$C_{UP2}=C_{UP3}=C_{14}$	$[2.25N_{Erb} - 0.64] \times 10^{-23}$ m^3/s for N_{Erb} = 0.5-3.0 (in wt%)
C_{CR}	$[0.705N_{yb} - 0.9935] \times 10^{-23}$ m^3/s for N_{yb} = 2.5-10 (in wt%)

Table 3.5 Material parameter values used for all further simulations [35,20]

3.9 Closer Examination of Model Equations

As a prelude to designing and fabricating waveguide structures doped with high rare-earth dopant concentrations, a conventional ridge waveguide will be modeled. Since there are numerous free parameters (rare-earth dopant concentrations, waveguide length, pump power, etc.) it is instructive to examine how each of them influences the eventual outcome. Ridge Waveguide 1 will serve as the control study. The behaviour of this device (in terms of gain/absorption coefficient, signal, pump and noise evolution along a waveguide, etc.) will be examined in detail. The results from this simulation will provide suggestions for improvement and warn of pitfalls to avoid.

Figures 3.16 shows the variation of signal gain as a function of erbium and ytterbium concentrations, with waveguide length and pump power fixed at 5 cm and 200 mW, respectively. When upconversion is ignored (C_{UP2}, C_{UP3} and C_{14} are set to zero), the signal gain is predicted to increase in direct proportion to erbium concentration. This leads to the erroneous conclusion that substantial gain could be achieved at high erbium concentrations without ytterbium co-doping. In fact, upconversion reduces the gain severely at high erbium concentrations, as predicted by Figure 3.16 and will be experimentally confirmed later. For moderately high erbium concentrations (>1 x 10^{26} ions/m^3), ytterbium co-doping improves the gain performance but the difference is noticeable only if the ytterbium-to-erbium dopant ratio falls within a specific range. In this instance, the optimum ytterbium-to-erbium ratio is 5-10 (from Figure 3.16). For dopant levels below or above this range, ytterbium sensitization is ineffective at best, detrimental at worst. The optimum ytterbium-to-erbium dopant range will vary depending on the desired length of the waveguide and the pump power available.

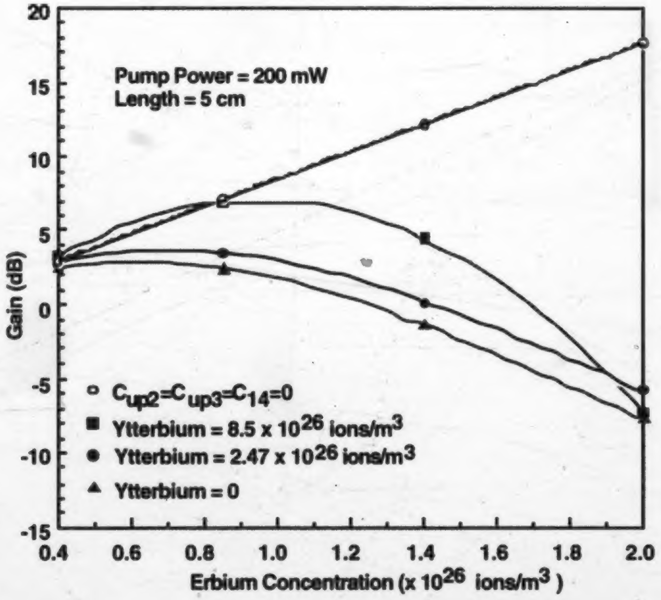

Figure 3.16 Signal Gain vs. Erbium Concentration for Ridge Waveguide 1; $P_p(0)$ = 200 mW; L = 5 cm; N_{Yb} = 0, 2.47 x 10^{26}, 8.5 x 10^{26} ions/m^3.

Figure 3.17 examines the variation in signal gain as a function of ytterbium concentration and waveguide length, with the erbium concentration and pump power fixed at 1.4 x 10^{26} ions/m^3 and 200 mW, respectively.

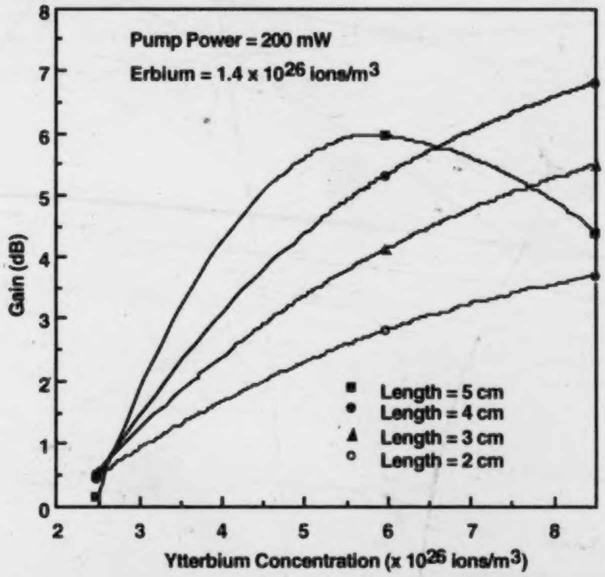

Figure 3.17 Signal Gain vs. Ytterbium Concentration for Ridge Waveguide 1; $P_p(0)$ = 200 mW; L=2,3,4 and 5 cm; N_{Erb} = 1.4 x 10^{26} ions/m^3.

The model predicts a maximum signal gain of ~7dB over 4 cm with 8.5 x 10^{26} ytterbium ions/m^3. With the same waveguide structure and pump power, NTT's experimental result netted 11dB of gain over 19.4 cm with 0.485 x 10^{26} erbium ions/m^3. Thus, by increasing the erbium concentration three-fold and adding ytterbium, the gain efficiency has been improved from 0.567 dB/cm to 1.75 dB/cm. The pumping efficiency drops from 0.055 dB/mW to 0.035 dB/mW due to strong pump absorption.

The evolution of pump and signal along the waveguide are plotted in Figures 3.18 and 3.19, respectively. In the absence of ytterbium, pump propagation is a slowly-varying exponential function of waveguide length; the depletion rate is almost constant at 0.58 dB/cm. In the presence of ytterbium, the depletion rate increases to ~1.65 dB/cm over the first 3 cm. There is an inflection point near 3.5 cm, beyond which the slope of the curve changes noticeably. At pump powers below 1mW, population inversion is no longer possible and the pump depletion rate increases dramatically to 25 dB/cm over the last 1 cm. The peak signal strength coincides with the change in slope of the pump curve. Strong re-absorption of the signal is evident beyond 4 cm. Hence, the optimum length for this waveguide amplifier under these conditions is 4 cm.

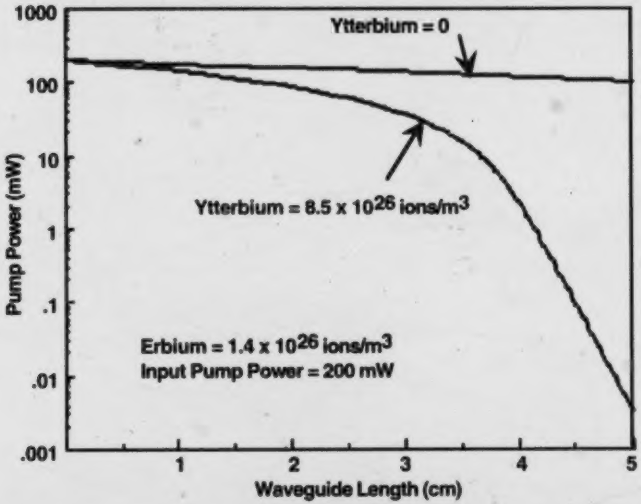

Figure 3.18 Pump Power vs. Waveguide Length for Ridge Waveguide 1; $P_p(0) = 200$ mW; $N_{Erb} = 1.4 \times 10^{26}$ ions/m^3; $N_{Yb} = 0, 8.5 \times 10^{26}$ ions/m^3.

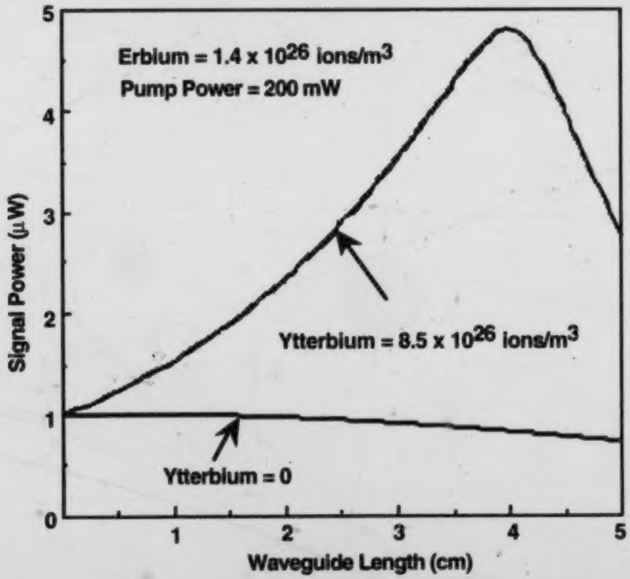

Figure 3.19 Signal Power vs. Waveguide Length for Ridge Waveguide 1; $P_p(0) = 200$ mW; $N_{Erb} = 1.4 \times 10^{26}$ ions/m^3; $N_{Yb} = 0, 8.5 \times 10^{26}$ ions/m^3.

The gain and absorption coefficients are plotted as a function of waveguide length in Figures 3.20 and 3.21, respectively. Since the gain coefficient is proportional to $N_2\sigma_{21}-N_1\sigma_{12}$, the vertical axis of Figure 3.20 can also be viewed as a measure of population inversion (N_2-N_1) along the waveguide. The inversion ratio is ~ 81% at the beginning, ~50% after 4 cm, and a negligible 8% after 5 cm, at which point the absorption coefficient is almost an order of magnitude higher than the gain coefficient.

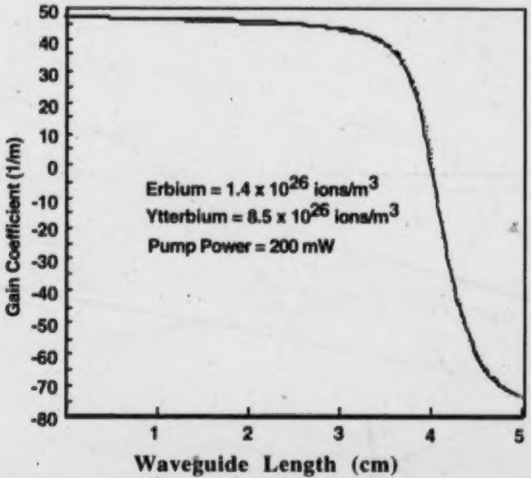

Figure 3.20 Gain Coefficient vs. Waveguide Length for Ridge Waveguide 1; $P_p(0)$ = 200 mW; N_{Erb} = 1.4 x 10^{26} ions/m^3; N_{Yb} = 8.5 x 10^{26} ions/m^3.

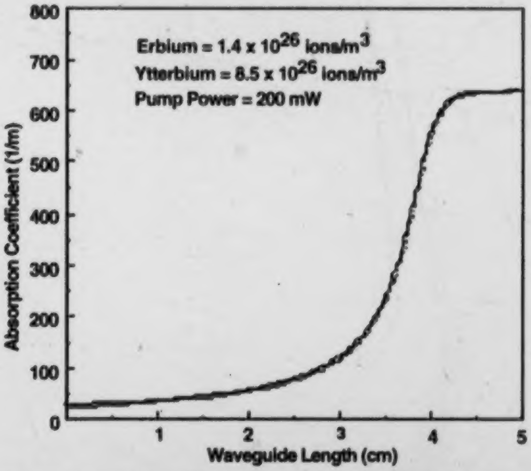

Figure 3.21 Absorption Coefficient vs. Waveguide Length for Ridge Waveguide 1; $P_p(0)$ = 200 mW; N_{Erb} = 1.4 x 10^{26} ions/m^3; N_{Yb} = 8.5 x 10^{26} ions/m^3.

The ASE power spectrum is plotted in Figure 3.22 for the case of maximum gain. The total area under the curve represents 3.24 μW of broadband ASE power that is generated over 4 cm. Optical filters with bandwidths as narrow as 1nm may be used at the output of the waveguide to supress most of this unwanted ASE noise. However, the ASE power contained within a bandwidth of 1nm at the signal wavelength (λ_s=1.532 μm) represents noise that cannot be supressed. This in-band ASE noise power amounts to 77 nW. Since the amplified signal power at the end of the waveguide is 4.8 μW, the Signal-to-Noise (SNR) ratio is 18 dB. In practical applications, the signal is usually frequency-modulated. The unmodulated, in-band ASE power is thus easily distinguished from the signal of interest.

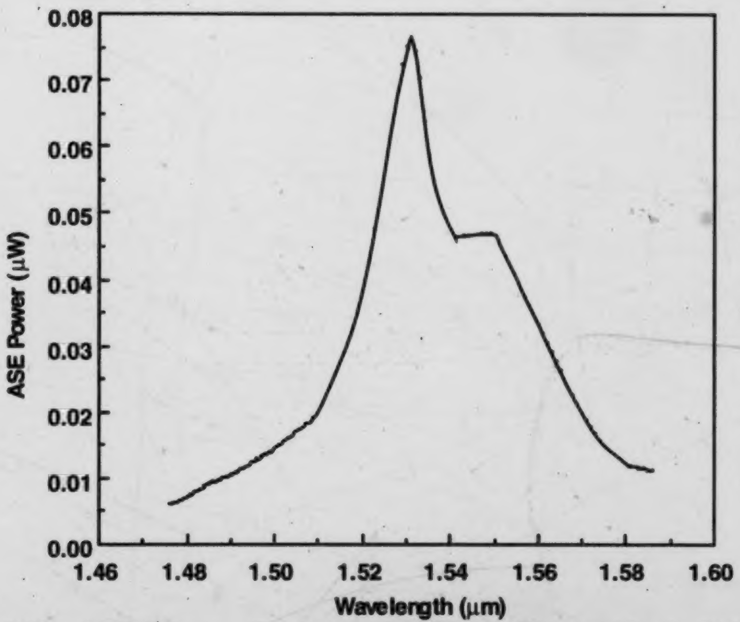

Figure 3.22 ASE Power Spectrum for Ridge Waveguide 1; $P_p(0)$ = 200 mW; L = 5cm; N_{Erb} = 1.4 x 10^{26} ions/m^3; N_{Yb} = 8.5 x 10^{26} ions/m^3.

The ASE power spectral plot takes the same form as that of the emission transition cross-section (Figure 3.2). Since this is true for all of the waveguides simulated in this thesis, only numerical values for broadband ASE power, in-band ASE power and Signal-to-Noise ratio will be provided henceforth.

Chapter 4 : Fabricating Optical Waveguides from Thin Films of Sputtered/PECVD Glass

4.1 Introduction

Two fundamental steps are involved in the fabrication of a silica-based planar optical waveguide : 1) deposition of thin films of glass, with appropriate refractive indices, on a silicon wafer. 2) selective removal of the deposited glass in all regions other than that intended for use as the waveguide. The basic principles behind silica micromachining and thin-film deposition processes such as sputtering and plasma enhanced chemical vapor deposition (PECVD) will be described. Later, the various processes and device designs that were attempted will be described. It should be noted that publication of specific processing recipes has been withheld in some cases as they are proprietary knowledge of the Alberta Microelectronic Centre (AMC). Although this chapter is primarily concerned with the actual fabrication of waveguides, some optical test results and considerations are included to illustrate the chronological progression of events and provide motivation for future chapters.

4.2 Thin-film Deposition and Micromachining:

4.2.1 Sputtering:

A typical sputter-deposition system (Figure 4.1) consists of a chamber that is evacuated to a pressure in the 1-100 mtorr range. The target glass is made a cathode through the application of approximately -20kV. The substrate on which the desired film is to be deposited is positioned directly underneath the target and forms the anode. A glow discharge is maintained between target and substrate through electron impact ionization of argon gas. The positive argon ions are accelerated towards the cathode and bombard the target glass with energies in the 0.1-1 KeV range. This creates a collision cascade (described as "atomic billiards" [36]) within the target glass, leading to the ejection of constituent atoms (with energies less than 50 eV). Some of the ejected (or sputtered) atoms are intercepted by the substrate, where a thin-film is formed over time. The pressure inside the chamber determines the average distance that sputtered atoms travel before colliding with another particle, be it an electron, an argon ion or a sputtered atom. At low pressures, the number of atoms sputtered from the target is reduced, as is the deposition rate. At high pressures, more argon ions bombard the target. Although this increases the number of sputtered atoms, a greater number of them are lost due to collisions and never reach the substrate. There is a fine balance to be struck in choosing the optimum operating pressure and power for deposition [36,37].

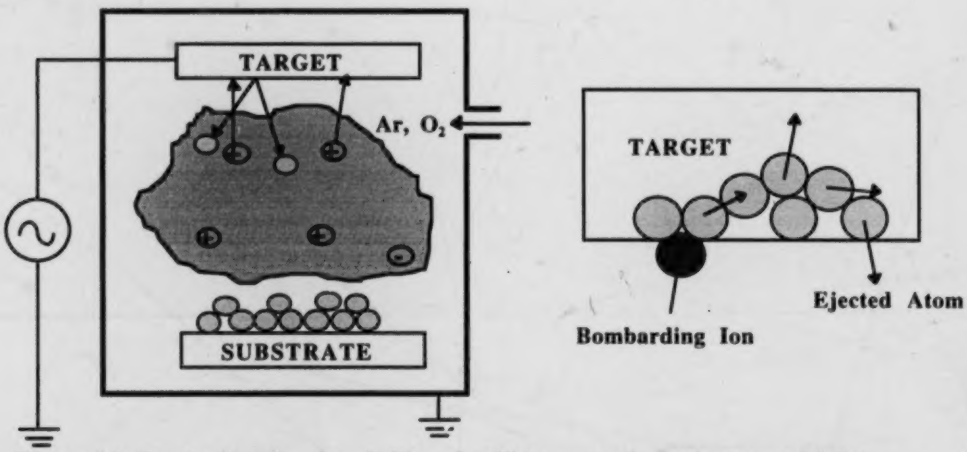

Figure 4.1 Sputtering chamber (left) and collision cascade at the target (right).

There are two common concerns regarding the reliability of the sputtering process : 1) It is conceivable that lighter atoms in the target glass may be preferentially sputtered at the expense of heavier atoms (such as rare-earth metals). 2) It is also conceivable that contaminants in the chamber may be incorporated into the deposited film. A subtler concern relates to oxygen deficiency in the system, which could prevent the rare-earths from being in their trivalent state (Er_2O_3). This is of critical importance since unreacted metallic erbium does not interact with photons. Addressing these issues is beyond the scope of this thesis. Given a rare-earth-doped multicomponent target glass, staff scientists at AMC sputtered thin-films onto three-inch silicon wafers. Micromachining these sputtered films was part of my research mandate.

4.2.2 Plasma-Enhanced Chemical Vapour Deposition (PECVD): PECVD processes also occur inside an evacuated chamber. An RF glow discharge is maintained through electron impact ionization of reactant gases. Unlike sputtering, CVD thin-films are actually solid-phase products of a chemical reaction between the chosen gases [38]. The reaction occurs on the surface of the heated substrate and gaseous by-products are ventilated out. A typical reaction may involve silane and ammonia to produce silicon nitride and hydrogen :

$$3SiH_4\ (g) + 4NH_3\ (g)\ \text{-->}\ Si_3N_4\ (s) + 12H_2\ (g)$$

The composition, density, refractive index and stress of CVD films are determined by the flow rates of the reactant gases, chamber pressure, substrate temperature and the RF power applied to the electrode [39].

Two kinds of CVD films were used in this thesis. A low-index (n=1.46) silicon dioxide (SiO_2) film approximately 5 μm thick was used as a buffer between the high-index silicon wafer (n=3.4) and the optical waveguide. The chemical reaction involved in producing SiO_2 is as follows :

$$SiH_4\ (g) + O_2\ (g)\ \text{-->}\ SiO_2\ (s) + 2H_2\ (g)$$

The other CVD film used extensively in this thesis was silicon oxynitride (SiON), which is the product of a plasma-enhanced reaction involving silane, ammonia and nitrous oxide:

$$SiH_4\ (g) + NH_3\ (g) + N_2O\ (g) + N_2\ (g)\ \text{-->}\ SiO_x\,N_y(s) + H_2\ (g)$$

The refractive index of SiON can be varied between n=1.46 (SiO_2) and n=2.0 by controlling the N_2O/NH_3 ratio inside the chamber [40]. SiON films were used as passive optical waveguides when and where appropriate. It should be noted that incorporating Er_2O_3 into the CVD process is difficult given the difference in volatility and vapor pressures [18]. At least one research group has succeeded in incorporating low levels (~0.48 wt %) of erbium in phosposilicate glass using PECVD [41]. Another research group attempted to incorporate erbium ions into SiON films through ion-implantation [42]. At present, AMC does not have the facilities to investigate these methods.

4.2.3 Photolithography: Photolithography is used to mark regions on the deposited glass over which the waveguide is to be formed Photolithography is a multiple-step process and is illustrated pictorially in Figure 4.2. First, a thin (<1.5 μm) uniform layer of photo-resist is spin-coated on top of the glass film. Photo-resist (PR) is sensitive to ultra-violet (UV) light and resistant to chemical etchants, hence the name. The sample is then heated to improve adhesion between PR and the glass. A photomask is placed in direct contact with the PR-coated sample, which is then exposed to a short burst of UV light. A photomask is a slab of glass with narrow strips of chrome (widths of 5 μm or even less) configured to form desired geometric patterns. The PR is exposed to UV-light everywhere except in the regions immediately underneath the chrome. The exposed regions of the PR are then rinsed away in a developer, leaving the protected regions to stand alone as rectangular ridges. The sample is then heated again to anchor the PR to the glass film in preparation for the next step - etching.

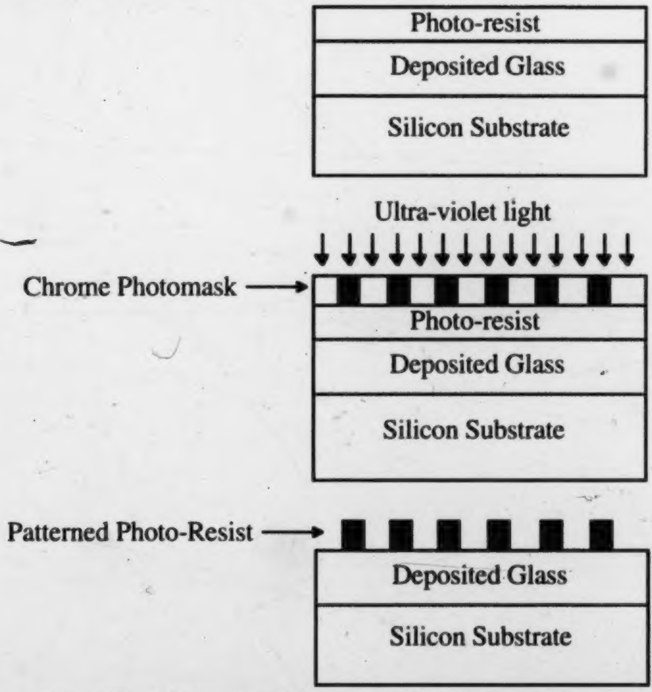
Photo-resist
Deposited Glass
Silicon Substrate
Ultra-violet light
Chrome Photomask
Photo-resist
Deposited Glass
Silicon Substrate
Patterned Photo-Resist
Deposited Glass
Silicon Substrate

Figure 4.2 Photolithographic steps : spin-coating of photo-resist (top), selective exposure to UV-light (middle), developing the exposed regions of the photo-resist (bottom).

4.2.4 Wet-Etching: The final step in forming the optical waveguide involves selective removal of the deposited glass, or etching. The deposited glass film can be etched in a chemical solution called Buffered Oxide Etch (BOE), which is a mixture of hydrofluoric acid and nitric acid. Just as the chrome photomask selectively protected PR from exposure to UV-light, the PR shields the glass film from exposure to BOE in regions which eventually form the waveguide. Since PR is resistant to BOE, mask erosion is not a factor in wet-etching. Wet-etching is an isotropic process, with the etch proceeding in all directions. If the glass film is x μm thick, a complete vertical etch would result in a lateral "under-cut" of equal distance (measured from the outer edges of the photo-resist). If the under-cut is too severe, the photo-resist may peel away due to inadequate support. After the etch is timed to completion, the photo-resist is rinsed away in acetone and the unetched portions of the deposited glass constitute the optical waveguide. In the case of wet-etching, the waveguide is far removed from the ideal rectangular profile. This process is illustrated pictorially in Figure 4.3.

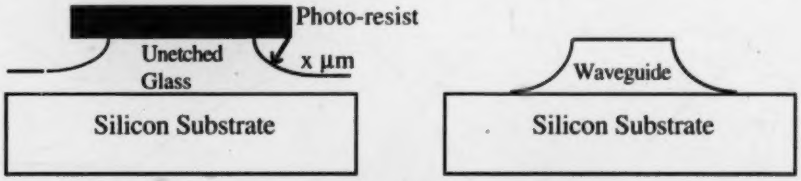

Figure 4.3 Chemical wet-etching : Isotropic etch-profile and under-cut (left), non-rectangular optical waveguide (right).

Chemical wet-etching produces anisotropic etch-profiles only in crystalline structures like silicon [43,44]. However, the glass films considered in this thesis are amorphous and anisotropic etch-profiles are only possible using reactive ion etching.

4.2.5 Reactive Ion Etching: Reactive ion etching (RIE) is a dry, gas-based process commonly used to etch glass. The process takes place in an evacuated chamber and in the presence of fluorine-based gases which are ionized by impact with electrons. In some respects, RIE can be thought of as the reverse of PECVD. In RIE, free radicals in the plasma react with the deposited glass to form volatile products, which are then ventilated out. CHF_3 and CF_4 have been widely used to etch anisotropic trenches in glass [45-47]. Free fluorine combines with silicon as follows:

$$Si(s) + 4F(g) \dashrightarrow SiF_4 (g)$$

Glass removal also occurs due to sputter-etching, which results from ion-bombardment caused by the difference in potential between the substrate and the plasma. Sputter-etching is a strong function of the RF power applied to the electrode and the chamber pressure. Sputter-etching does not remove the glass in the lateral direction since ion-bombardment is highly directional. Hence, anisotropic etch-profiles are obtained. Unfortunately, accelerated ions also bombard the photo-resist, which results in mask erosion [48]. *Etch selectivity*, a relative measure of the etch rates for glass and mask, is defined as follows :

$$\text{Etch Selectivity} = \frac{\text{Etch Rate of Glass } (\mu m/min)}{\text{Etch Rate of Mask } (\mu m/min)}$$

An etch selectivity greater than unity is desirable since it would allow the entire glass film to be etched with a mask of comparable thickness. The process is illustrated in Figure 4.4.

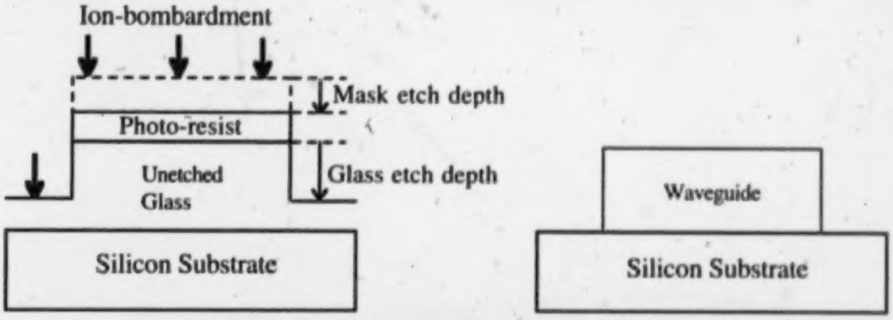

Figure 4.4 Reactive Ion Etching: Anisotropic etch-profile of glass and mask erosion (left), rectangular optical waveguide (right).

4.3 Sputtering Er-doped Glass Films:

According to published experimental results [31,41,49,50] and simulations from the previous chapter, planar erbium-doped ridge waveguides with small cores were known to be optimum for high signal amplification. An erbium-doped bulk glass, labelled TRL-A, was purchased from Schott Glass Technologies (SGT) with the aim of fabricating such waveguides. TRL-A was a variant of the S-8040 series of filter glasses manufactured by SGT. The S-8040 series is a collection of lanthanum sodium silicate host glasses, each of which can host up to 30 wt. % of a particular lanthanide element [51]. The precise chemical make-up of TRL-A was not released by SGT since the information was deemed proprietary. The Er_2O_3 content was confirmed as 3 wt. % (~ 3 x 10^{26} ions/m^3). The refractive index of TRL-A was specified to be n=1.60 at a wavelength of 587.6 nm. The density of the glass was specified as 3.33 g/cm^3.

A three-inch silicon wafer was first coated with 5 μm of CVD-oxide. Using TRL-A as the target, a 1.5μm-thick film was then sputter-deposited atop the SiO_2 layer. The film growth rate was only 5 nm/min, which forced the deposition run to last several hours. The film was 5-10% thicker in the center of the wafer due to higher flux of sputtered atoms prevalent in the middle of the chamber.

4.4 Wet-Etching Sputtered Erbium-doped Glass Films

AMC's standard recipe for photolithography was used to pattern photo-resist (HPR 504) strips 5, 7 and 9 μm wide on top of the sputtered film. The sample was then etched in a 10:1 solution of BOE and intermittently inspected using a microscope and a profilometer. It was observed that residue from the etch tended to accumulate in the regions adjacent to the ridge. This was confirmed through profilometer measurements (Figure 4.5). Stirring the BOE solution during the etch reduced this build-up to a certain extent but did not eliminate it completely.

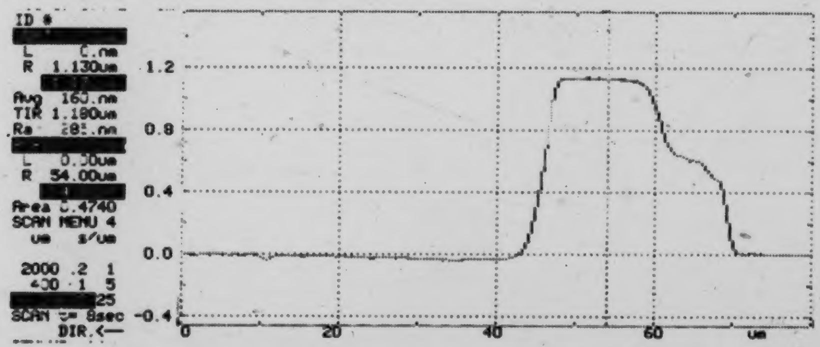

Figure 4.5 Profilometer scan revealing build-up of etch residue adjacent to ridge.

The etch residue was removed completely only when the sample was immersed in a "hot piranha" solution (1:3 mixture of hydrogen peroxide and sulfuric acid), commonly used to remove organic impurities. After removing the etch residue and the photo-resist, the ridges were photographed (Figure 4.6) using a Scanning Electron Microscope (SEM).

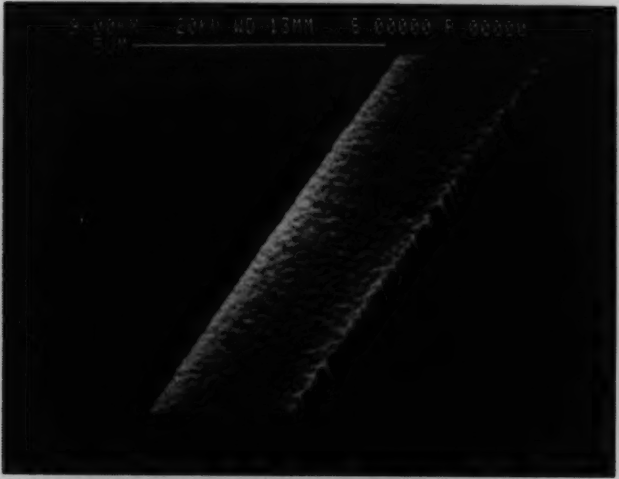

Figure 4.6 SEM photograph of ridge waveguide fabricated by wet-etching.

The etch depth varied from 0.92 to 1.15 µm along a 5 mm stretch of one randomly chosen waveguide. This non-uniformity is a consequence of attempting to etch a multicomponent film with a single etchant [47]. BOE etches SiO_2, which forms approximately 70% of the sputtered film. The remaining 30% consists of sodium, lanthanum and erbium, all of which are impervious to BOE. Regional variations in film composition may also have contributed to the non-uniformity in etching.

The waveguide shown in Figure 4.6 was tested for its optical properties. The attenuation was so severe that 10µWatts of launched He-Ne light were almost completely extinguished over 1 cm. There was no evidence of spontaneous or stimulated emission in this waveguide. Two avenues were pursued in an effort to improve light propagation in this waveguide. A 2µm-thick SiO_2 layer was deposited (PECVD) on top of the Er-doped ridge waveguide to reduce index mismatch at the waveguide sidewalls, which is a major cause of scattering loss [52]. However, the stress imposed by the upper-cladding seemed to have altered the waveguide profile (Figure 4.7). Light propagation in the waveguide worsened, possibly due to stress-fractures in the ridge.

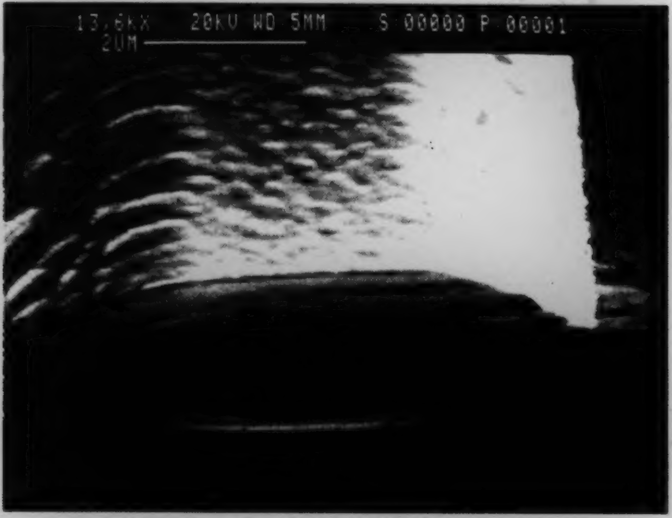

Figure 4.7 Stress induced on ridge waveguide by deposition of upper-cladding.

Alternatively, an attempt was made to anneal the waveguide by heating it to the transition temperature specified for the sputter-target glass. Annealing was expected to rectify any porosity in the sputtered film and smoothen the jagged edges induced by the etch [53]. However, the waveguides suffered a catastrophic structural change during the course of the reflow (Figure 4.8). This unexpected turn of events generated a new line of research, which is described in the next chapter.

Figure 4.8 Change in ridge waveguide structure following reflow step.

4.5 Reactive-Ion-Etching Sputtered Erbium-doped Glass Films

In response to the lack of success with wet-etching, the focus of attention shifted towards RIE as a means of fabricating ribs on the sputtered film. AMC's standard RIE recipe (chamber pressure of 40 mTorr and RF Power of 150 Watts in the presence of CHF_3 and CF_4) for etching CVD-oxide was used to etch the sputtered film. However, it was found that the etch rate for the sputtered film (90 Angstroms/min) was significantly slower than for SiO_2 (715 Angstroms/min). Variations in gas flow rates and chamber pressure did not influence the etch rate for the sputtered film significantly. However, the etch rate was a strong function of RF power, confirming that the film was being etched almost exclusively by ion-bombardment and not chemical reaction. The absence of reactive etching is most likely a consequence of the bond structure for this particular glass. Since photo-resist was being etched at the rate of 200 Angstroms/min under these conditions, the etch selectivity was only 0.45. This was inadequate to etch through 1.5 μm of the sputtered film. Hence, alternative masking layers were investigated.

Metallic chrome (0.5 μm thick) was deposited on top of the sputtered glass film. Ribs 5, 7 and 9 μm wide were patterned on the chrome using photo-lithography and wet-etching. With chrome now acting as the masking layer, the sputtered film was etched in the RIE chamber under different RF power settings (Table 4.1).

RF Power	Etch Rate for Er-doped film	Etch Rate for Chrome	Etch Selectivity
150 Watts	90 Angstroms/min	17 Angstroms/min	5.3
200 Watts	134 Angstroms/min	28 Angstroms/min	4.8
250 Watts	173 Angstroms/min	43 Angstroms/min	4.0

Table 4.1 Etch rates and selectivity for reactive ion etching sputtered erbium-doped glass film, with chrome acting as mask.

The chrome proved a much hardier mask, improving etch selectivity significantly. Still, the reliance on high RF power meant that the sputtered glass film had to be exposed to strong ion-bombardment over extended durations. This took a toll on the quality of the sidewalls (Figures 4.9 and 4.10).

Figure 4.9 Rib formed on sputtered Er-doped glass film using RIE : RF Power = 100W.

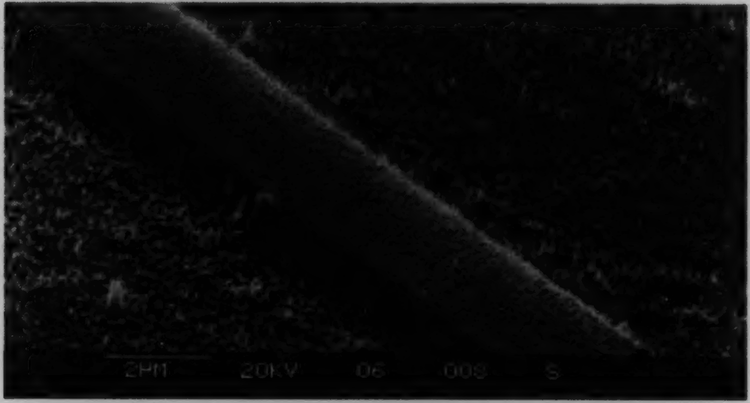

Figure 4.10 Rib formed on sputtered Er-doped glass film using RIE : RF Power = 250W.

It should also be noted that this particular method of micromachining rib waveguides involves two pattern transfers, from photo-resist to chrome and then onto the Er-doped glass. Each transfer dilutes the quality of the final pattern. This is partly responsible for the "squiggly" sidewalls evident in Figure 4.9. All of the above factors combined to make the resulting waveguides extremely lossy. The inability to successfully etch such a complex glass is a paradox since it is that very complexity which allows for the incorporation of large quantities of erbium.

4.6 Reactive-Ion-Etching SiON films

In stark contrast, it was observed that SiON lent itself very well to dry etching. Even at RF powers as low as 80 Watts, the etch rate for SiON was 333 Angstroms/min, suggesting that chemical reaction was the primary cause for the etch. With an etch selectivity in excess of 2.0 (with respect to photo-resist), ridges 3 μm deep could be etched in one hour, with little or no damage inflicted by bombarding ions on the highly anisotropic sidewalls (Figure 4.11).

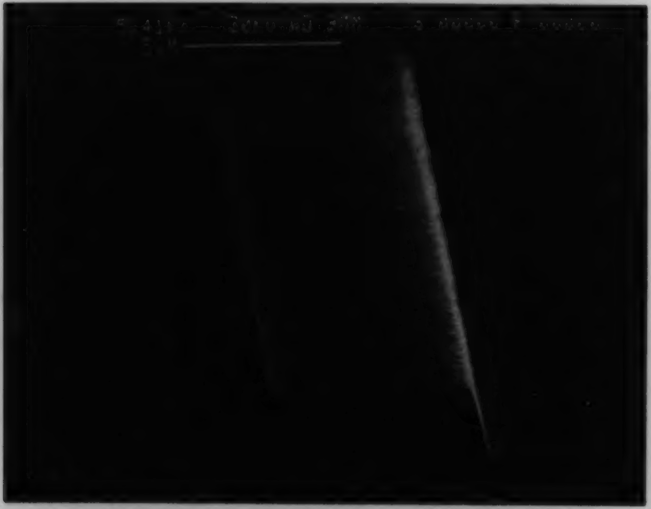

Figure 4.11 Rib formed on SiON film using RIE : RF Power of 80W.

Optical loss measurements [54] were performed at a wavelength of 980 nm on two SiON ridge waveguides, one etched shallow and the other deep. Both waveguides were exposed to identical RIE process parameters (RF Power of 100 Watts), but for different durations.

Waveguide Dimensions	Loss without upper-cladding	Loss with upper-cladding
1.5 μm deep; 9 μm wide	0.82 dB/cm	0.42 dB/cm
3.0 μm deep; 9 μm wide	1.54 dB/cm	0.59 dB/cm

Table 4.2 Optical loss characteristics of SiON ridge waveguides.

Based on these results, an attempt was made to design and fabricate a composite waveguide combining the sputtered Er-doped film and SiON.

4.7 Fabricating Composite Multiple-Layer Ridge Waveguides

Up to this point, there had been no evidence of spontaneous emission at any wavelength in any of the erbium-doped waveguides that were fabricated. To achieve this initial success, a deep low-loss ridge waveguide was deemed essential for two reasons: 1) increased photon intensity due to strong lateral light confinement. 2) improved coupling due to large mode-field diameter [55]. However, it became increasingly apparent that fabricating such waveguides on the sputtered film was impractical. Therefore, a composite waveguide was designed (Figure 4.12) whereby a very thin (0.2 μm) layer of the sputtered Er-doped film was sandwiched between two thick (2.0 μm) layers of SiON.

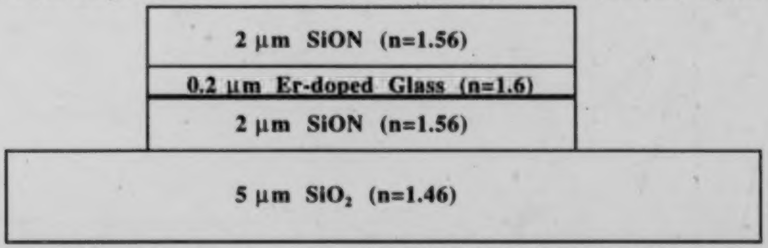

Figure 4.12 Design of composite SiON/Er-doped ridge waveguide.

In choosing the refractive index for SiON (a variable parameter - Section 4.2.2), two conflicting considerations had to be balanced. On one hand, the SiON index had to be lower than that of the Er-doped film to maximize light intensity in the middle of the ridge. On the other hand, the mode-field diameters could be widened only by limiting the index difference. The film thicknesses were chosen based on the knowledge (from Sections 4.5-4.6) that the combined layer structure (4.2 μm) could be reactive ion etched in approximately ninety minutes using an RF Power of 150 Watts. The fabricated device, which was 4.3 cm long, is shown in Figures 4.13-4.14. "Grass" patterns evident on the waveguide sidewalls are common artifacts of long etches [48]. A Norland Optical Adhesive [56] was spin-coated on top of the ridge to act as an upper-cladding.

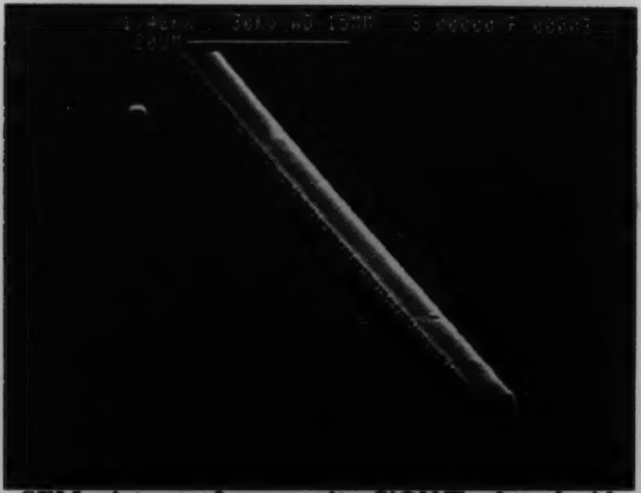

Figure 4.13 SEM picture of composite SiON/Er-doped ridge waveguide.

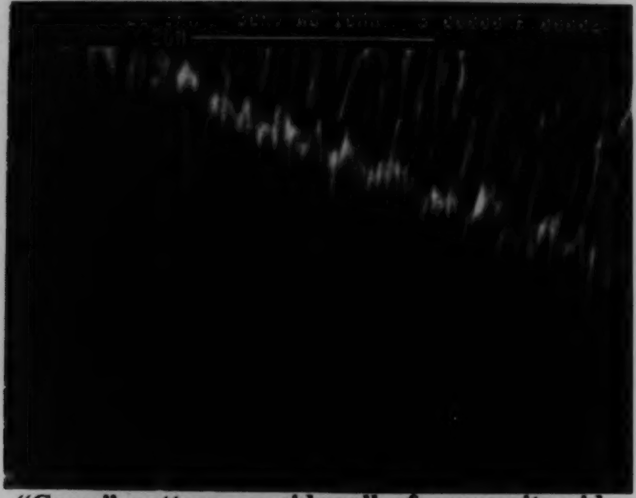

Figure 4.14 "Grass" pattern on sidewall of composite ridge waveguide.

When this waveguide was pumped with 975 nm light, a faint trace of green light was visible near the input (along the first 2 mm). This was the first indication of spontaneous emission from the sputtered film, although the emission was at an undesired wavelength (please see Figure 3.1 and Section 3.2). However, there was still no evidence of spontaneous emission at infra-red wavelengths. Fiber-to-fiber throughput loss (which includes insertion, scattering and absorption losses) was measured at different wavelengths (Table 4.3). The results suggested that 975 nm pump light was not being absorbed as strongly as 1550 nm light.

Wavelength	Throughput Loss
632 nm	15.5 dB
870 nm	14.0 dB
975 nm	17.4 dB
1550 nm	36.0 dB

Table 4.3 Fiber-to-fiber throughput loss for composite ridge waveguide.

To investigate this further, the waveguide near-field was imaged on a CCD camera (please see 6.2.2). The near-field image of 975 nm pump light (Figure 4.15) revealed a null in intensity in the middle of the waveguide, where the Er-doped film was located. FWAVE confirmed that the electric-field distribution for the second-order pump mode had a null in the middle of the core. Given that spontaneously emitted green light was visible near the input, it appears likely that optical power had coupled from the fundamental mode to the second order mode at some point along the waveguide. This would explain the relatively weak pump absorption (Table 4.3) and the absence of infra-red emission.

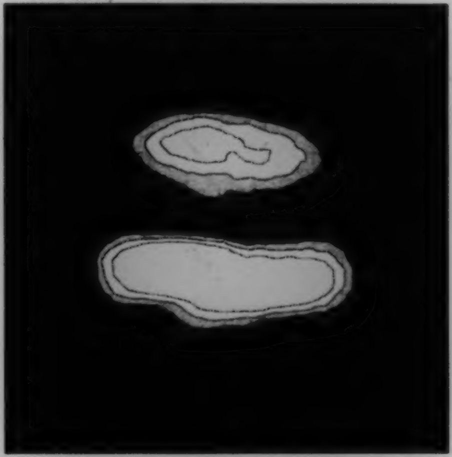

Figure 4.15 Near-field image of 975nm light in composite ridge waveguide.

Although the composite SiON/Er-doped ridge waveguide did not serve its intended function, these results provided valuable information which would help direct future efforts. The next iteration in design was the SiON/Er-doped strip-loaded waveguide, which produced the first observation of spontaneous and stimulated emission at 1550nm (discussed in Chapter 6).

Chapter 5 : Micromachining Circular Hollow Channels From Planar Rectangular Glass Films

5.1 Introduction

This chapter recounts the investigation of a unique micromachining technique, discovered during the course of fabricating optical waveguides. As described in the previous chapter, ridge waveguides fabricated by wet-etching were marked by high losses. Other research groups have recommended annealing as an effective solution to address these shortcomings [42,49]. During the annealing process, oxygen diffusion into sputtered and ion-implanted films has been shown to activate unreacted rare-earth metals to their trivalent state and improve luminescence intensities and lifetimes. Also, it is common knowledge that reflowing the glass helps smoothen jagged edges induced by the etch. A series of annealing/reflow experiments were undertaken in an effort to rectify the spectroscopic properties of the sputtered film and improve waveguide loss performance.

5.2 Formation of Hollow Microchannel - Run #1

Using the process recipe described in the previous chapter, rib waveguides ranging from 5-9 µm in width were wet-etched on a 0.7 µm thick film of sputtered Er-doped glass (Figure 5.1).

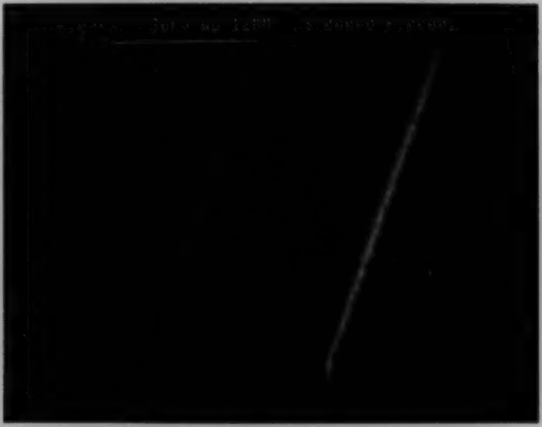

Figure 5.1 - A 0.7µm x 7µm rib wet-etched on sputtered Er-doped film.

The etch was continued past the estimated time required for the 0.7 μm film. This was done to compensate for non-uniformities in film thickness and the etching process. Etching into the SiO_2 under-cladding ensured that the sputtered film was completely cleared over all parts of the wafer. Due to their small vertical dimension, insertion loss in these waveguides was expected to be too high for any meaningful optical characterization. These waveguides were to be used only as test samples for characterizing annealing parameters such as temperature, duration, environment, etc.

A large portion of the wafer was cleaved and annealed in a thermal oxidation furnace at 600 °C with water vapour flowing across the furnace tube at the rate of 100 sccm. The sample was loaded only after the furnace had reached the set temperature point. After one hour, the sample was unloaded and a small segment of the wafer was cleaved for SEM analysis. The remaining portion was re-loaded into the furnace to be annealed longer. An SEM picture (Figure 5.2) revealed the appearance of random bubbles in the waveguide but not in the surrounding regions. The waveguide edges were still sharp, suggesting that the glass hadn't reflown significantly even at a temperature ~70°C higher than the specified transition temperature for the bulk glass.

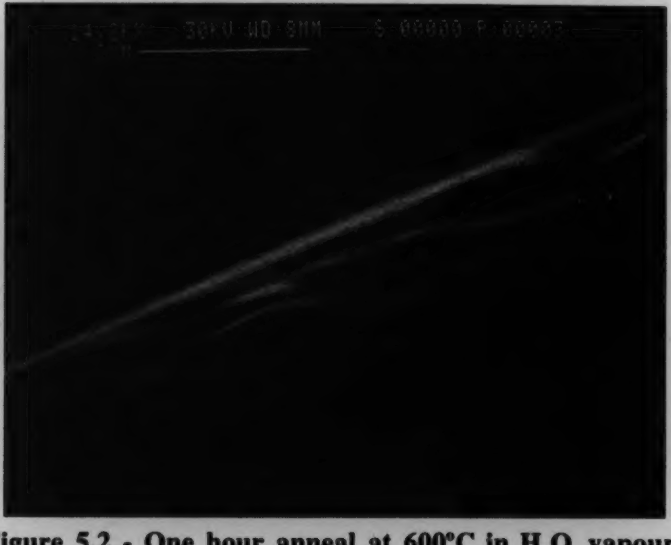

Figure 5.2 - One hour anneal at 600°C in H_2O vapour.

After two hours, the glass appeared to have softened to the point where the waveguide cross-section had a rounder profile (Figure 5.3). Bubble formation was even more pronounced at this stage.

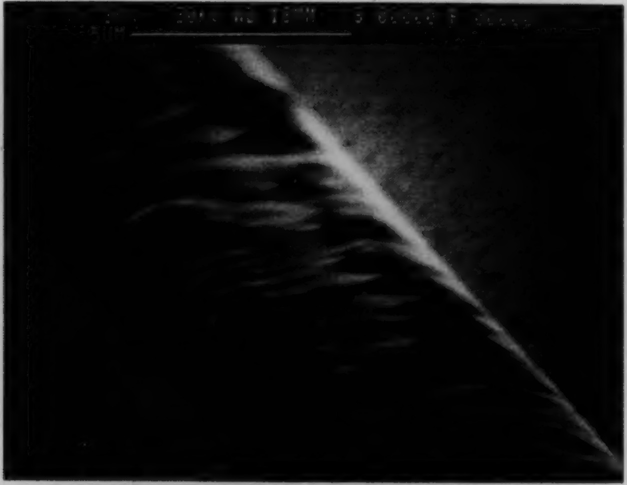

Figure 5.3 - Two hour anneal at 600°C in H_2O vapour.

After three hours, the glass had reflown completely and was extremely smooth in texture but there had been a fundamental change in its structure. An SEM picture (Figure 5.4) of the cleaved edge revealed that the rectangular glass ribs had detached from the underlying SiO_2 layer and had been re-shaped into hollow "tunnels".

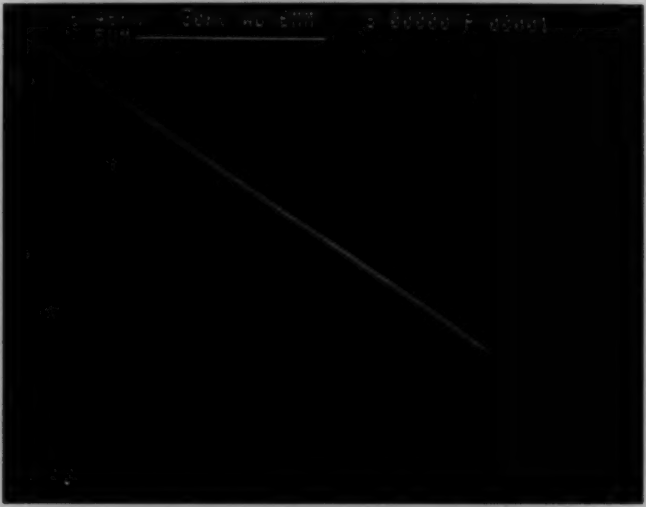

Figure 5.4 - Three hour anneal at 600°C in H_2O vapour; 7μm wide rib.

Profilometer scans confirmed the change in profile and increase in height. However, the structure was brittle and had a tendency to collapse under the weight of the profilometer stylus. Thus, the structural uniformity along the length of the "tunnel" could not be established. The change in profile was also evident in the smaller ribs, which were narrower than the intended 5 μm due to etch under-cut. At these dimsensions, the "tunnel" manifested itself in the form of a sub-micron sized hole running through the middle (Figure 5.5).

Figure 5.5 - Three hour anneal at 600°C in H_2O vapour; 2 μm wide rib.

Based on thin-film literature, two possible explanations were considered for this phenomenon - compressive stress and/or loss of adhesion due to accumulation of gas. In his book on thin-film deposition [37], Donald L. Smith comments on both:

> "Compressive stress failure is characterized by de-adherence and buckling, which from the top appears sometimes as domes or bubbles and sometimes as an undulating meander pattern looking like a mole tunnel".
>
> "Gas evolution from films can also cause de-adherence if the gas becomes trapped at the interface so that it builds up pressure there. Sputter-deposited films often contain a percent or two of Ar, and plasma-CVD films can contain tens of percent of H" (pp. 185-200).

In this specific instance, the contributing factor was not immediately obvious. While photographs taken during the early stages of the anneal (Figures 5.2-5.3) seem to correspond to Smith's description of stress-induced failure, the final result (Figure 5.4) suggests an interface effect. Stresses in thin films are induced by mismatch in coefficient of thermal expansion between the thin film and the substrate, which is the case here. Since the SiO_2 layer was CVD-deposited and the upper film was sputtered in an argon environment, gas evolution due to argon and hydrogen incorporation was also likely. Annealing characteristics were investigated further in an attempt to understand this phenomenon.

5.3 Formation of Hollow Microchannel - Run #2

For the next run, the thickness of the sputtered film was increased to 1.3 μm. In the event of tunnel formation, the increased film thickness was expected to provide better structural integrity. Before patterning and etching waveguides on this film, a piece of the wafer was annealed under the same conditions as before. After one hour, bubbles were observed all over the sample (Figure 5.6), some as large as 100 μm in diameter.

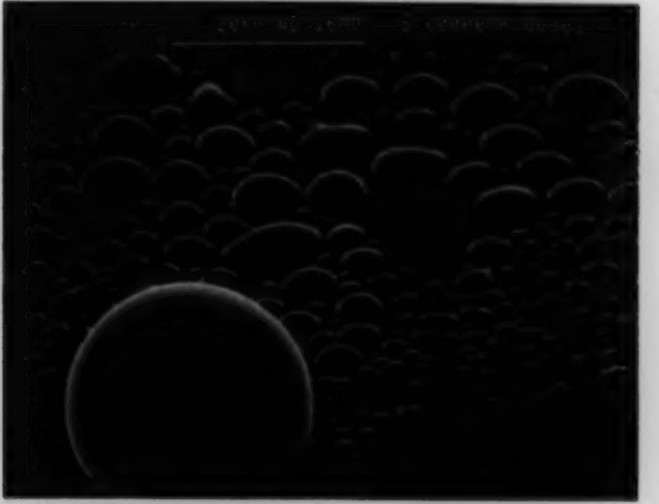

Figure 5.6 - One hour anneal of a planar sputtered film.

According to an expert on thin-films [57], the likelihood of stress inducing such a response was limited considering the extent of deformation evident in Figure 5.6. Evolution of gas was deemed more plausible given the 100 μm wide bubble. According to the literature, microspheres of this size have been produced by intentionally mixing blowing agents (such as anhydrous sodium sulfate, calcium carbonate, sodium carbonate, urea, etc) into the glass and gassifying them at high temperatures [58,59]. This so-called "reboil phenomenon" relies on the evolving gas to re-shape the molten glass.

Ribs were etched on the thicker film using the same process recipe. Since etching through the entire film resulted in under-cut and peeling of the photoresist, the etch depth was limited to 1 μm. Unlike the previous case, where the sputtered film had been completely removed from regions adjoining the rib, a thin film (0.3-0.4 μm) remained adjacent to the ribs. The width of the ribs were < 6 μm (Figure 5.7).

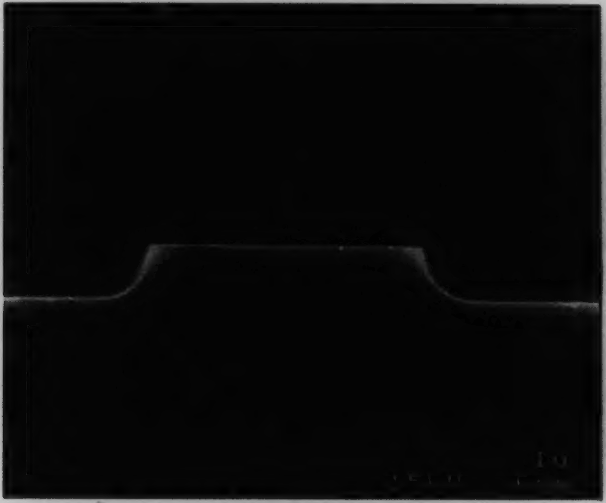

Figure 5.7 - 1.0μm x 6μm rib etched on a 1.3μm-thick sputtered film.

After a few trial runs, the temperature was set to 580°C. Since bubbling was observed to occur regardless of the environment, the sample was annealed in ambient conditions inside the furnace. After one hour, a cleaved edge of the sample revealed that the planar ribs had once again been transformed into "tunnels", but on this occasion the cross-sectional profile was remarkably circular with a diameter of almost 9 μm (Figure 5.8). Owing to the higher resolution of this photograph, the detachment was confirmed to occur at the interface between the sputtered film and the underlying SiO_2 layer. The structure was still too brittle for profilometer measurements. However, there were no noticeable structural discontinuities along the hollow microchannels, as tests would later confirm.

Figure 5.8 - Cleaved edge of a sample annealed for 60 minutes.

Figure 5.9 shows evidence that the transformation in profile was not an aberration. The photomask that was used to pattern the ribs had 24 lines, each 9 µm wide and separated from one another by 100 µm. Microchannels were formed from every line.

Figure 5.9 - Multiple microchannels on the same substrate.

A SEM picture of the uncleaved outer edge of the annealed sample is shown in Figure 5.10. Clearly, the inflation of the ribs had not extended all the way to the outer edges. The original rectangular profile of the rib was preserved close to the edges of the sample (within ~ 10 μm) and the change in profile had occurred only in the interior regions.

Figure 5.10 - Uncleaved edge of a sample annealed for 60 minutes.

An explanation for the tapered edges remains at large. However, the sealed ends lent further credence to the theory of gas-entrapment. Gas build-up at the interface between the sputtered glass film and the oxide layer, coupled with the absence of an outlet on either end, seemed to have contributed to re-shaping the softened glass over time. In order to verify this theory, another sample was annealed under the same conditions for 30 minutes and cleaved into two pieces. A SEM picture of the cleaved edge (Figure 5.11) showed that the sidewall was thicker and the diameter of the microchannel smaller when compared to the sample that was annealed for 60 minutes. This established the duration of anneal as an important parameter which influences the eventual size and shape of the "tunnel" structure.

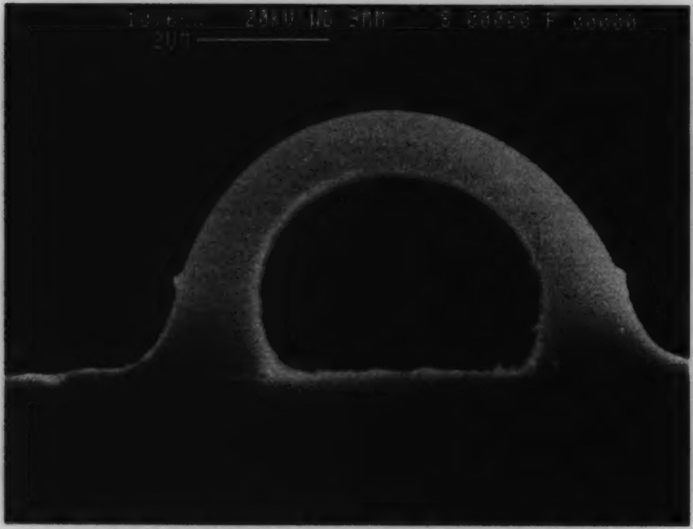

Figure 5.11 - Cleaved edge of a sample annealed for 30 minutes.

The other half of the cleaved sample was then annealed for another 30 minutes, with the expectation that the resulting structure would be similar in dimension to that of Figure 5.8. However, no further re-shaping of the glass was observed, confirming that the cleaved edge had provided an outlet for the gas on one end and halted the inflation process. It is worth noting that since the glass film was only partially etched, a very thin layer of glass was present in the regions adjacent to the ridge. However, no inflation was visible in those regions after the anneal. Presumably, gas was able to diffuse out through such a thin film of glass. Also, regions of the glass exposed to the etchant were visibly pitted (Figure 5.10), which may have facilitated the out-gassing.

In an effort to identify the gases that evolve during the anneal, samples were sent out for mass spectrometer analysis at The Westaim Corporation. According to the report filed by their Analytical Laboratory, no gases were detected below temperatures of 550°C. The mass spectra for water, oxygen and carbon dioxide were detected at 600°C, but barely above background levels. The report concluded by suggesting that the mass spectra pattern may be incomplete and that a thicker film coating might yield a more accurate analysis. However, due to the slow sputter-deposition rates, this approach was not pursued further.

5.3.1 Testing

Two experiments confirmed that the microchannels of Figures 5.8 were hollow over their entire lengths. First, a 1 mm He-Ne laser beam ($\lambda = 632$ nm) was focused with a 20X microscope objective lens into one end of a hollow microchannel 7 mm long (cleaved at both ends). A 60X microscope objective was used to magnify the image at the output end of the microchannel onto a CCD camera. Figure 5.12 shows a near-field image of the far end. The emerging light is confined within the wall of the microchannel, which appears in the picture as a dark ring. Observation of side-scattered light showed that the attenuation was moderate and that there were no abrupt changes in intensity. In the second experiment, water was seen to enter the microchannels by capillary action when one end was immersed (Figure 5.13).

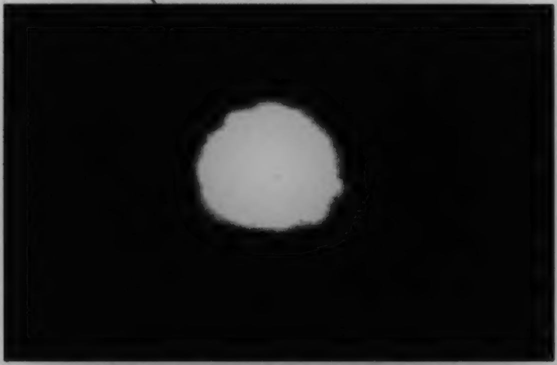

Figure 5.12 - Near-field image showing light propagating within the hollow microchannel.

Figure 5.13 - Water entering the hollow microchannel through capillary action.

5.4 Formation of Hollow Microchannels - Run #3

Up to this point, the most important process parameter influencing the formation of the hollow microchannel appeared to be the duration of the anneal, rather than temperature or environment. The erbium-doped glass was sputter-deposited on yet another oxide-coated wafer to assess its sensitivity to other process parameters : ridge depth, adhesion and ridge width. Due to changes in the sputtering system, staff scientists at AMC were forced to change the sputtering parameters and the maximum thickness of the deposited film was now limited to 1 μm. The film was etched to depths ranging from 0.1 μm to 0.6 μm and annealed under identical conditions. In the case of a shallow etch (etch depth < 0.2 μm), the inflation of the glass due to gas occured everywhere and not just underneath the ridge. Consequently, the microchannels were not clearly defined and could barely be distinguished from the surrounding regions, which were also inflated at random (Figure 5.14).

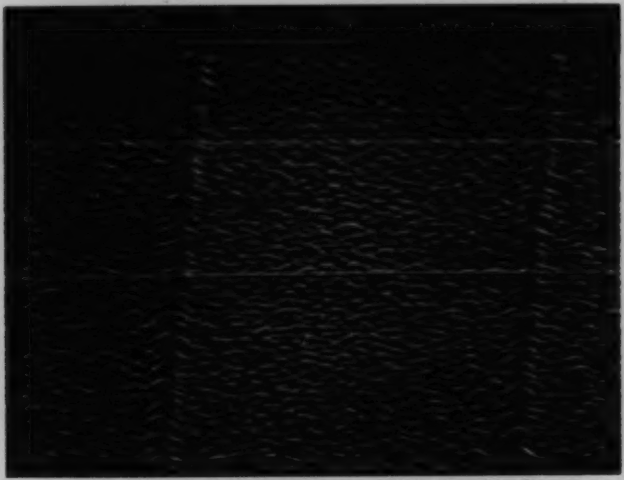

Figure 5.14 - Shallow etch fails to produce well-defined hollow microchannels.

For etch-depths greater than 0.6 μm, no bubbling was evident in the adjoining regions and the microchannels were clearly defined (Figure 5.15). This confirmed the earlier supposition that evolving gases were able to diffuse out through a thin film of glass but tended to accumulate beneath thicker layers. Even though the annealing conditions were identical to previous runs, this microchannel was semi-circular in profile as opposed to the circular profile seen in Figure 5.8. Also, fibrous glass strands were visible inside the microchannel. This suggested that there was an increased tendency for this glass film to adhere to the underlying oxide. A less sticky glass film would likely face less resistance and be able to inflate more, thus giving the circular profile seen before. The adhesion factor, which is a function of the sputtering conditions and the cleanliness of the substrate, thus affects both the interior surface quality of the microchannel and its profile.

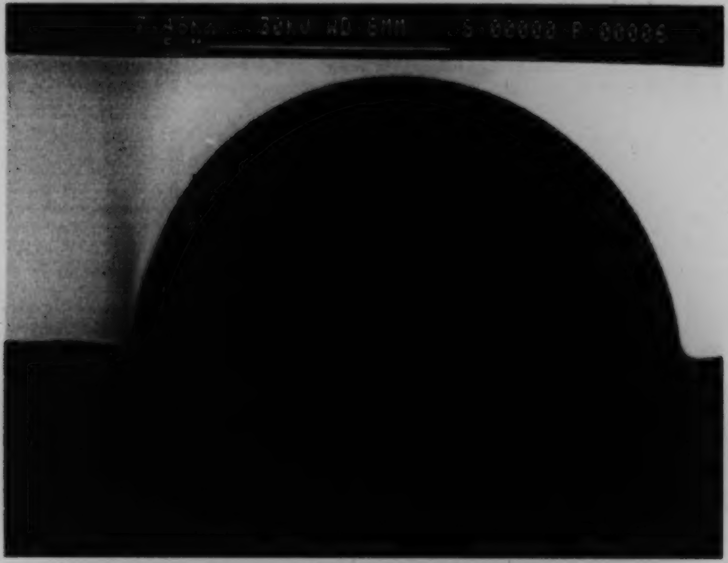

Figure 5.15 - A deeper etch produces a well-defined hollow microchannel. The cross-section of this microchannel differs from earlier runs due to adhesion effects.

A new photomask with 5, 7, 9, 11, 13, 15, 20, 25, 50 and 100 µm wide features was designed in an effort to fabricate microchannels of various sizes. After patterning and annealing, the corresponding height of the microchannels were 1.4 µm, 2.1 µm, 2.8 µm, 3.4 µm, 4.0 µm, 4.4 µm, 6.1 µm, 6.6 µm, 12 µm and 24 µm. Thus, the height:width ratio of the resulting microchannels remained approximately constant (1:3.5-4.0) regardless of the original width of the rib. One of the largest microchannels that was fabricated is shown in Figure 5.16. The fibrous strands resulting from improved adhesion are even more apparent in this photograph.

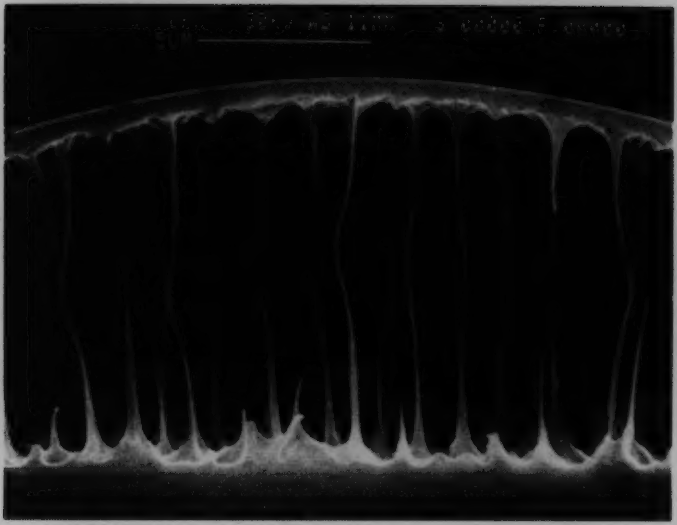

Figure 5.16 - A 12 μm high, 50 μm wide microchannel.

An attempt was made to fabricate microchannels in the form of a Y-branch. A 10 μm wide straight section was split into two 5 μm wide branches. After annealing, microchannel formation was evident in all three sections. The height of the branching arms was only 1 μm, in keeping with the typical aspect ratio. As a result of surface tension, water was seen to enter the straight section of the microchannel but not the smaller branching arms (Figure 5.17). However, ambient air in the straight section had to have been displaced through the branching arms by the water. This intuitively confirmed that there was no phyical discontinuity at the branching point despite the disparity in size.

Figure 5.17 - Water inside one arm of a Y-branch microchannel.

5.5 Potential Applications of Hollow Microchannels

Hollow glass microchannels on planar substrates are of interest for integrated optics, micromechanics and microfluidics. These devices have many diverse applications such as light-guiding [60,61], biomedical analysis [62], chemical analysis [63] and sensors [64,65]. Their use may potentially extend to include on-chip cooling for integrated electronic and optoelectronic devices [66].

With some exceptions [67], hollow devices are generally fabricated by etching grooves or channels in a substrate and sealing the groove with a lid. The etched regions of the substrate forms the hollow microchannel. The fluid of interest is then pumped into the microchannel using micropumps. In certain cases, the etching of trenches is dependent on the nature of the substrate and is limited by substrate characteristics such as crystal structure. Hence, present technologies yield microchannels with rectangular, triangular or semi-circular cross-sectional profiles. The conceptual difference between currently employed methods and the method outlined in this chapter is illustrated pictorially in Figures 5.18 and 5.19.

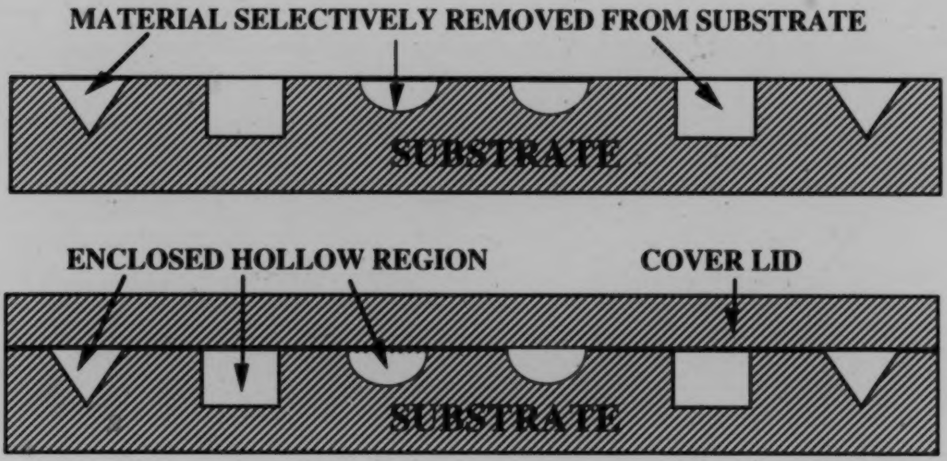

Figure 5.18 - Existing technology to fabricate hollow microchannels.

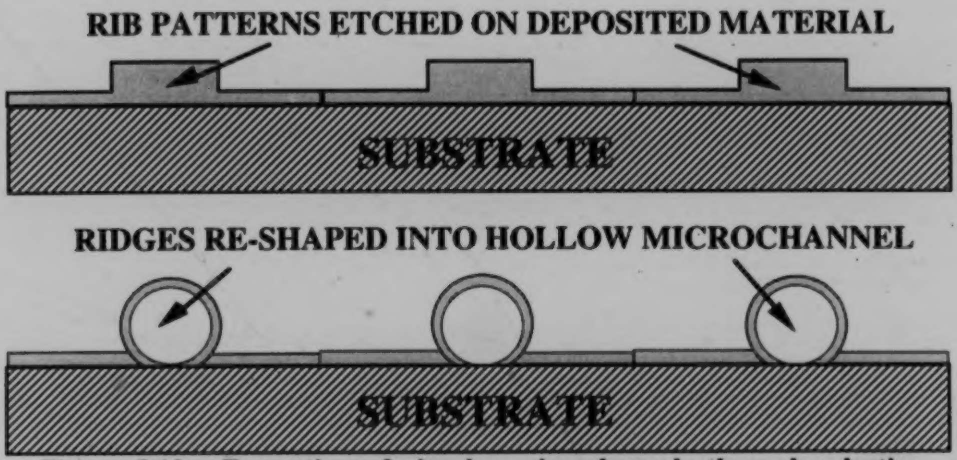
RIB PATTERNS ETCHED ON DEPOSITED MATERIAL
SUBSTRATE
RIDGES RE-SHAPED INTO HOLLOW MICROCHANNEL
SUBSTRATE

Figure 5.19 - Formation of circular microchannels through selective accumulation of gas and de-adherence.

Although a significant amount of research is still required to develop this concept into a functional device, the micromachining principle outlined in this chapter could offer several advantages over current technologies : 1) As a surface micromachining technique, it is independent of the underlying substrate. Such microchannels could conceivably be fabricated on any integrated microfluidic or micro-optic substrate. 2) Circular cross-sectional profiles would likely be more conducive to fluid flow. 3) Hollow microchannels with complex topographies (such as Y-branches) could be realized merely by photolithographic control. 4) Potentially, the principle of selective inflation through gas accumulation and de-adhesion can be applied to a wide variety of materials, not just glass.

Chapter 6 : Rare-Earth-Doped Waveguides in Strip-Loaded Configurations - Fabrication and Modeling

6.1 Introduction

In response to the difficulties encountered in etching deep ribs on sputtered multicomponent glass films, alternative waveguide structures were explored. In a strip-loaded device, the waveguide core consists of two layers with closely matched refractive indices ($\Delta n<0.3$). A rib is etched on the upper film; the lower film is left as a planar slab. The rib provides the lateral confinement required to guide light in two dimensions. The index difference determines the extent to which light overlaps with the underlying slab. By creating a composite core with two different materials, advantages and disadvantages inherent to either material can be exploited or circumvented. Issues related to rare-earth-doped strip-loaded waveguides - fabrication, testing, design options and modeling - are discussed in this chapter.

6.2 Experimental Results for Erbium-doped Strip-Loaded Waveguide

6.2.1 Fabrication and Spectroscopy

The TRL-A bulk glass (Section 4.3) was again used as the target to sputter thin films of erbium-doped glass. To identify the various absorption bands of erbium, a spectrophotometer was used to study transmission of light (over the wavelength range 500-1100 nm) through a 2 mm-thick sample of the TRL-A (Figure. 6.1).

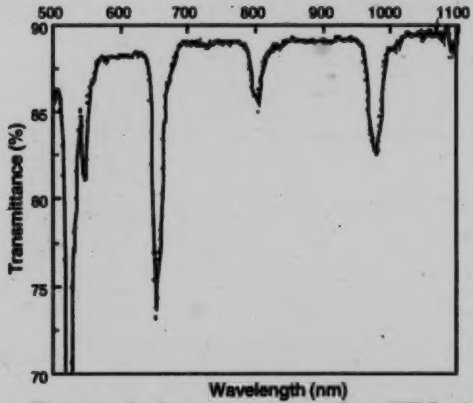

Figure 6.1 - Transmission spectrum for TRL-A bulk glass.

A thin film (1.5 μm) was sputtered from the TRL-A onto a silicon wafer as described in Section 4.3. The material composition of the sputtered film is of critical importance to device performance. Although the sputtered film is intended to be a replica of the original sputter target, changes in composition are intrinsic to the sputtering process. Energy Dispersive X-ray (EDX) is one of the more accessible technologies available to analyze the composition of thin-films [39]. When a thin-film is bombarded with an electron inside a Scanning Electron Microscope (SEM), a core electron of an element in the film absorbs the energy of the bombarding electron and is excited to a higher orbit. When the excited electron subsequently relaxes to a vacant lower orbit, the process is accompanied by the emission of an X-ray photon. The energy of the X-ray photon is unique to that element. As the energy of the bombarding electron is varied from 10 to 30 keV, X-ray photon emission is detected from all of the elements in the film. An X-ray spectrometer attached to the SEM registers the intensity of the photon emission and identifies the element (by comparing the location of the intensity peaks to documented reference data). The results of an EDX scan on the sputtered film are shown in Figure 6.2 and the composition (in wt. %) is tabulated in Table 6.1.

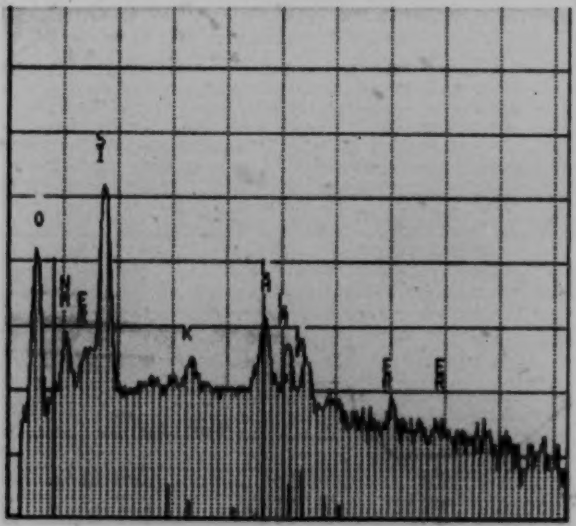

Figure 6.2 X-ray Photon Intensity vs. Electron Bombarding Energy - EDX scan of sputtered Er-doped glass film.

Element	Weight Percent
Si	70.11
Na	10.71
La	14.72
K	1.35
Er	3.12

Table 6.1 Composition of sputtered Er-doped glass film, obtained using EDX.

It should be noted that EDX gives only approximate quantitative estimates of film composition. EDX did confirm the absence of significant contamination and/or preferential deposition of elements but did not confirm that the rare-earth metals were in their trivalent state. Rutherford Back-Scattering or Secondary Ion Mass Spectroscopy are required for a more comprehensive spectroscopic analysis.

A 1.5μm-thick PECVD silicon oxynitride (SiON) layer was deposited on top of the sputtered film. The refractive index of the SiON layer was approximately 1.56 (at a wavelength of 632 nm). Ridges 9 μm wide were formed on the SiON film using photolithography and reactive ion etching (please see Section 4.6). The wafer was cleaved to produce waveguides 1.2 cm long. An SEM photograph showing the cross-sectional profile of the device is shown in Figures 6.3.

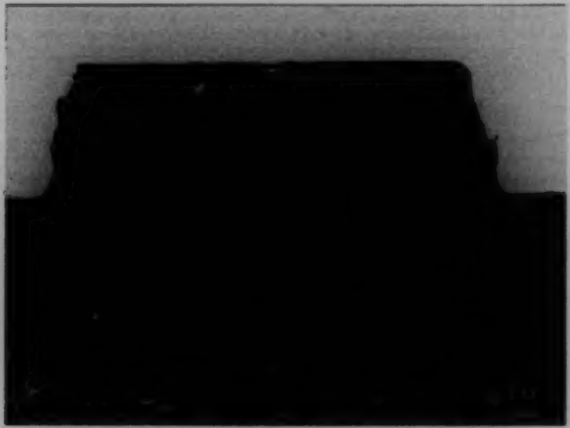

Figure 6.3 SEM photograph showing cross-section of strip-loaded waveguide.

Both the SiON rib and the underlying Er-doped glass film are dense and show no signs of porosity. The white streaks visible in the SiON layer and the SiO_2 under-cladding are not structural flaws inherent to the film; they are merely stress-induced anomalies incurred while cleaving the wafer.

6.2.2 Passive Optical Properties

The cross-section of the strip-loaded waveguide that was designed and the corresponding electric field lines for signal (λ_s=1550 nm) and pump (λ_p=980 nm) modes are illustrated in Figure 6.5. The structure supports only a single mode in the vertical direction at 1550 nm but is multimoded at 980 nm.

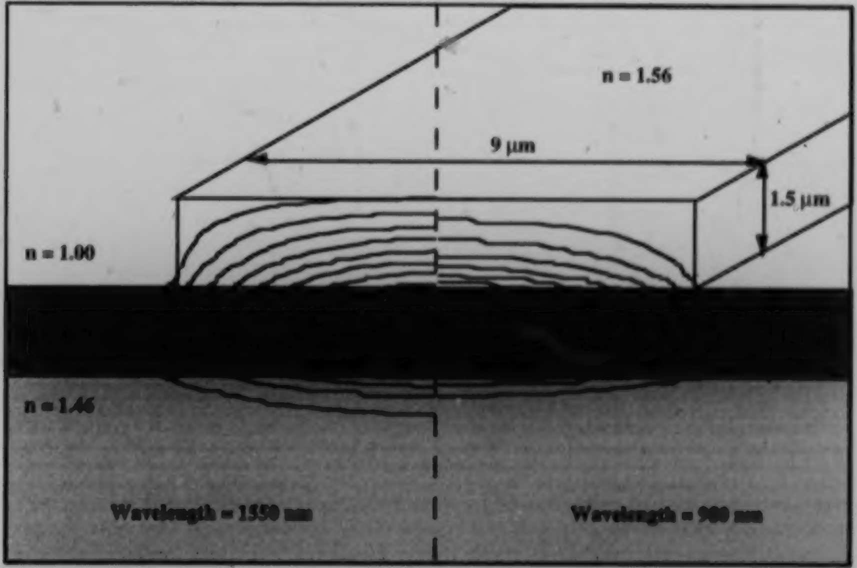

Figure 6.5 Strip-loaded Waveguide A. The dark-shaded layer is the erbium-doped sputtered film, with index n=1.59; the un-shaded layer is the SiON rib, with index n=1.56; the light-shaded layer is the SiO_2 cladding with index n=1.46. The TE field contours for the fundamental signal and pump mode are shown on the left and right, respectively. The contours represent 90% to 10% of peak amplitude. The device was 1.2 cm long.

The mode-field dimensions (defined as the distance between e^{-2} contour lines) are ~ 3.3 µm x 10.4 µm for the signal and 2.8 µm x 10.6 µm for the pump. The mode-field widths in the lateral direction closely matches the mode-field diameter for a singlemode fiber (MFD=10 µm for a core of 7 µm). Thus, only the fundamental modes were seen to be excited in this device during experiments, although the waveguide supports higher-order lateral modes in theory. The electric field overlap with the erbium-doped film was ~61% for signal and ~74% for the pump. In the erbium-doped slab layer, 10% field contour lines extend only 1 μm beyond the edge of the SiON rib, indicating strong lateral confinement. If the refractive index of the SiON film were to be lowered to that of SiO_2, greater than 95% of the electric field would overlap with the Er-doped region but the lateral confinement offered by the SiON rib would be negligible.

The modal areas for signal and pump intensity were 8.3 μm^2 and 6.7 μm^2, respectively. The normalized intensity profiles for signal and pump within the erbium-doped film are shown in Figure 6.6. Along the center of the waveguide, the normalized pump intensity is higher than the signal intensity over most of the erbium-doped region. This is true at points away from the center as well, since the pump mode-field contour lines extend farther out in the lateral direction than do signal mode-field contours.

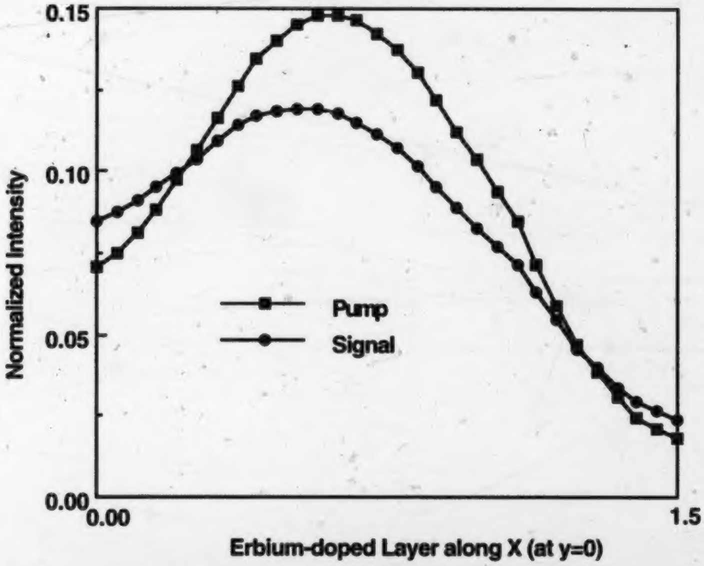

Figure 6.6 Normalized signal and pump intensity profiles along the center of strip-loaded waveguide A, within the sputtered erbium-doped film.

To begin the experiment, beams from a 975 nm laser diode and a 1547 nm Distributed Feedback Laser (DFB) were launched separately into a singlemode fiber. The singlemode fiber was butted to the input facet of the strip-loaded waveguide with the aid of index-matching fluid to improve coupling. At the output facet of the waveguide, a microscope objective lens and a beam expander were used to image the near-field onto a CCD camera. The near-field image of the pump intensity, shown in Figure 6.7, confirmed a tightly confined, asymmetric mode in the waveguide.

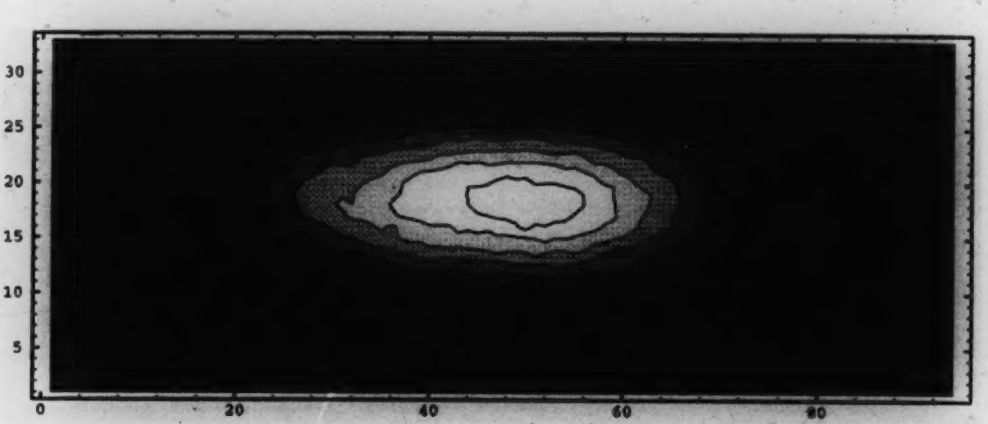

Figure 6.7 Image of near-field intensity for strip-loaded waveguide A, showing 90% to 10% contours for the 975nm pump beam. X and Y axes represent pixel numbers. 10 pixels ~ 1.3 μm.

To determine coupling and propagation losses at signal and pump wavelengths, light exiting the waveguide was collected using a step-index multimode fiber (62.5 μm core) and directed to a silicon or germanium photodetector. Optical throughput loss in the waveguide was determined by comparing the optical power measured at the output of the multimode fiber to that available on the single-mode input fiber. By cutting back the length of the waveguide, optical loss data was generated as a function of waveguide length. From a simple linear fit to the data (Figure 6.8), losses at 975 nm and 1547 nm due to Er^{3+} absorption and other factors were estimated to be ~ 3.5 and 5.9 dB/cm, respectively. Extrapolation of the measurements to zero length indicate coupling losses in the range of 3 to 4 dB, which is close to the theoretical value for coupling a circular fiber mode to an elliptical waveguide mode.

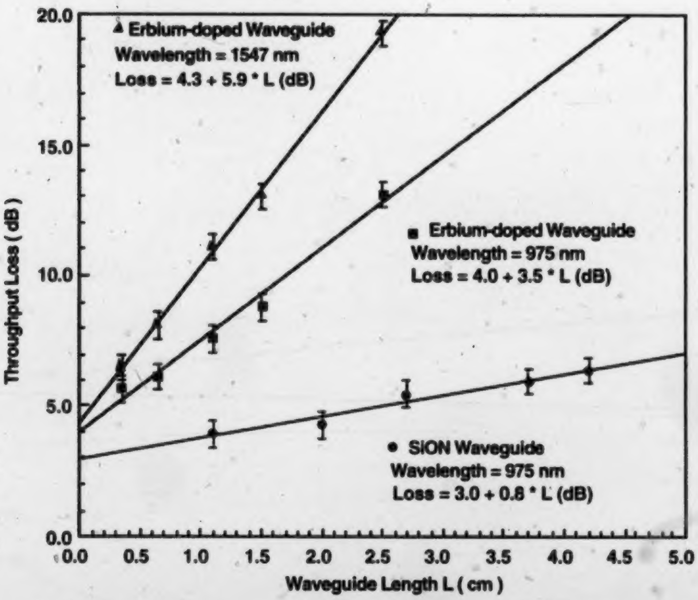

Figure 6.8 Cut-back throughput loss measurements for erbium-doped strip-loaded waveguide A and a comparison passive strip-loaded SiON waveguide. The measurements indicate strong absorption by erbium at 975 nm and 1547 nm. Measurements on the passive waveguide indicate excess propagation losses of 0.8 dB/cm.

For comparison, a passive strip-loaded waveguide with the same refractive index profile and dimensions was fabricated. Instead of the erbium-doped sputtered film, an SiON film of index n=1.59 and thickness 1.5 μm was used. Cut-back loss measurements on the passive SiON waveguide, also shown in Figure 6.8, reveal excess propagation losses of 0.8 dB/cm at 975 nm. Since SiON is extremely transparent at infra-red wavelengths, these losses can be attributed solely to imperfections in the waveguide. This excess waveguide loss can be assumed to be approximately the same for the erbium-doped device since the fabrication process recipe was not changed. The erbium-induced loss can thus be separated as ~ 5 dB/cm at 1547 nm and ~2.7 dB/cm at 975 nm. The propagation losses in the SiON waveguide improved to 0.4 dB/cm when a polymer (Norland Optical Adhesive 65) was spin-coated on top of the SiON rib to act as an upper-cladding. However, this option was not considered for the erbium-doped device because the high-index polymer (n=1.52) would have shifted the mode-fields up, away from the erbium-doped film.

6.2.3 Active Optical Properties

To study the active properties of the erbium-doped strip-loaded waveguide, a fiber Wavelength Selective Coupler (WSC) was purchased to combine pump and signal light onto a single fiber. The output fiber of the WSC was butted to the waveguide input. When 23 mW of pump power was launched into the waveguide, spontaneous emission was observed in the 1520-1580 nm wavelength region (Figure 6.9). The peaks at 1535 nm and 1550 nm are characteristic of erbium-doped silicate glasses. There was a faint trace of green light visible throughout the length of the waveguide as a result of co-operative upconversion. This was not unexpected for such high erbium concentrations.

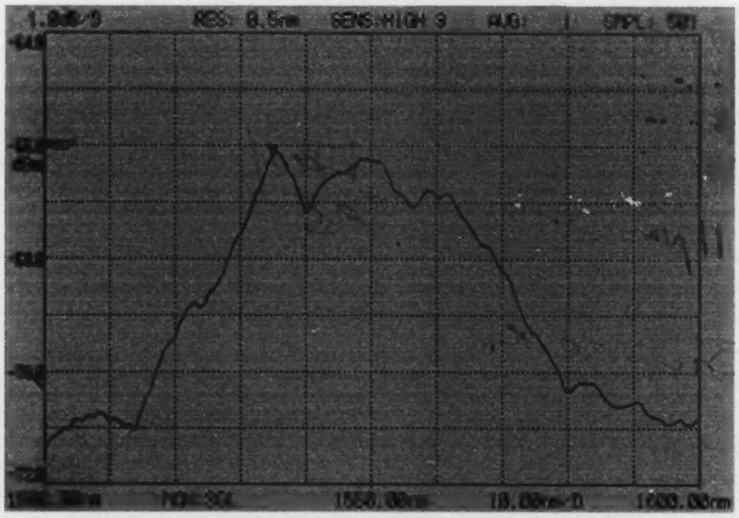

Figure 6.9 Spontaneous emission spectrum observed in strip-loaded waveguide A. The excitation source was 23 mW, launched from a single 975nm laser diode.

Back-scattered spontaneous emission near the waveguide input was used to measure the luminescence lifetime. Spontaneous emission is strong near the input facet of the waveguide, where population inversion is high. Backward-travelling spontaneous emission re-enters the WSC and exits through the open 1550 nm input port (a signal is not required when characterizing spontaneous emission). Light exiting the 1550 nm port of the WSC was filtered and detected with a germanium photodetector. Two 20 dB filters designed for the lower infra-red band were used to improve upon the 30 dB contrast offered by the WSC and ensure that the pump was extinguished. With the pump beam chopped at 50 Hz, the luminescence lifetime in the waveguide was measured to be ~148 μs (Figure. 6.10).

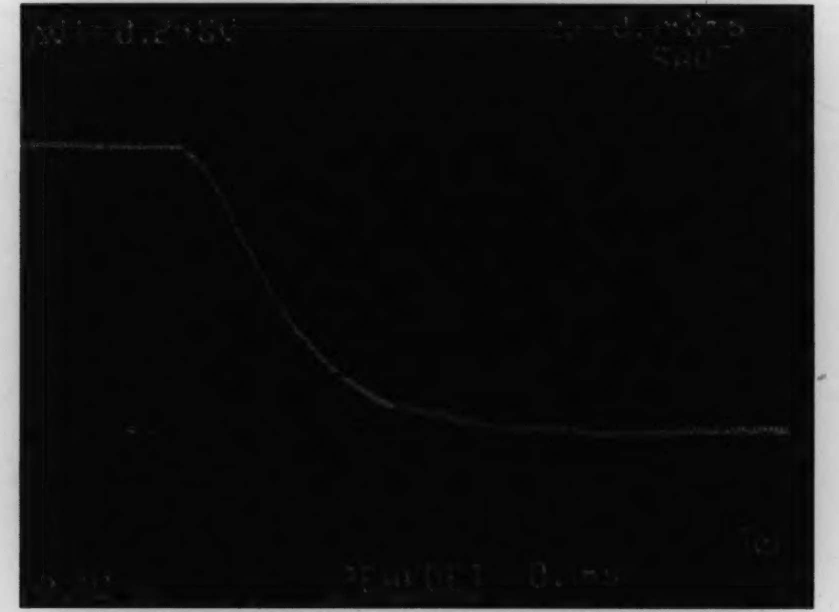

Figure 6.10 Luminescence lifetime measurement for strip-loaded waveguide A. Oscilloscope reading ΔT=148 μs corresponds to the time taken for the intensity to decay to 1/e of its peak value (ΔV = 0.248 V).

A similar experiment was performed on the bulk sputter target. The bulk glass was exposed to 60 mW of pump power and the measured lifetime was 87 μs. Since insertion losses were not a factor when illuminating a bulk glass, the pump intensity incident on the bulk was stronger than in the waveguide. The measurement in the bulk glass thus represents the lower limit for the lifetime, where ion-ion interaction is most severe. The lifetimes in the bulk glass and sputtered film were of the same order, suggesting that the spectroscopic properties of the glass were not significantly altered in this case. However, lifetime quenching was quite pronounced in both cases, much more so than would be expected due to upconversion. Non-radiative relaxation of excited ions through multiphonon emission could be a possible explanation for the low lifetimes measured in this glass.

Signal throughput in the waveguide was studied in the presence and absence of a pump source. Beams from the 1547 nm DFB laser and the 975 nm pump laser diode were launched into the waveguide simultaneously using the WSC. The signal throughput was found to increase by ~0.8 dB in the presence of 23 mW of launched pump power. Stated in a different form, signal loss in this device at 1547 nm was 7.1 dB (referring to Figure 6.8). Upon pumping, the signal loss improved to 6.3 dB. This enhancement in signal throughput does not represent amplification, but it is proof of an accumulation of erbium ions in the metastable state. Since the lasing wavelength for the DFB laser was 12 nm away from the peak emission observed in this waveguide (Figure 6.9), it was thought that stimulated emission would be stronger with a signal source operating near 1535 nm.

The next phase of the experiment was carried out at Seastar Optics in Victoria, British Columbia over the course of a week. A laser diode with multiple cavity modes in the 1530-1560 nm wavelength range was available at Seastar's research facility. In addition, two 975 nm laser diodes, each rated for 60 mW, were available. The two pump beams were combined in free-space using a polarization beamsplitter before being launched into a WSC. Light exiting the waveguide was fed to an optical spectrum analyzer so that multiple signal wavelengths could be viewed simultaneously. By doubling the pump power, signal throughput (near 1547 nm) was enhanced further, up to a maximum of 1.4 dB with 45 mW of launched pump power. Stimulated emission was found to be strongly dependent on signal wavelength. The enhancement in signal throughput was noticeably stronger near 1535 nm than 1555 nm, as shown in Figure 6.11. At a wavelength of 1535.5 nm, signal throughput improved by almost 2.9 dB upon pumping; at 1554.5 nm, the enhancement was only 0.7 dB. These results are indicative of stimulated emission for the following reason : if there had been no radiative contribution (i.e. no stimulated emission) resulting from the pumping, the reduction in ground-state population would have caused equal signal enhancement at all wavelengths. However, the signal enhancement is wavelength sensitive, similar to the emission cross-section.

Figure 6.11 Light exiting strip-loaded waveguide A resolved on an optical spectrum analyser. Multiple signal cavity-modes in the absence of pump (above) and in the presence of 45 mW of launched pump power (below).

Back in Edmonton, a second batch of erbium-doped strip-loaded waveguides was fabricated to investigate the reproducibility and uniformity of the fabrication process. Although glass deposition and micromachining process recipes were unchanged, the active optical properties were markedly different from the previous run. Figure 6.12 plots signal throughput enhancement as a function of waveguide length for 20 mW of launched pump power. At the 1.2 cm mark, the enhancement was half of what it was in the previous case. Beyond 1.5 cm, the enhancement began to decrease due to insufficient pump and signal re-absorption (similar in form to that of Figure 3.18).

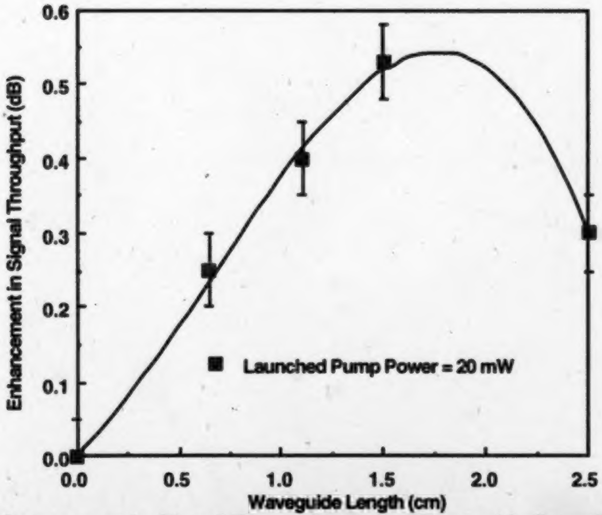

Figure 6.12 Enhancement in Signal Throughput vs. Waveguide Length. Experimental result for second batch of erbium-doped, strip-loaded waveguide A.

A few months later, the experimental set-up at TRLabs was upgraded when a tunable Ti:Sapphire laser became operational. Even with 200 mW of pump power now available at 975 nm, the 1.5 dB enhancement in signal throughput (Figure 6.13) was insufficient to compensate for the 3.5 dB net signal loss sustained over 0.6 cm. These results confirmed that device performance was being severely hampered by upconversion. Further, the unpredictability and non-uniformity of the sputtering process was an on-going obstacle.

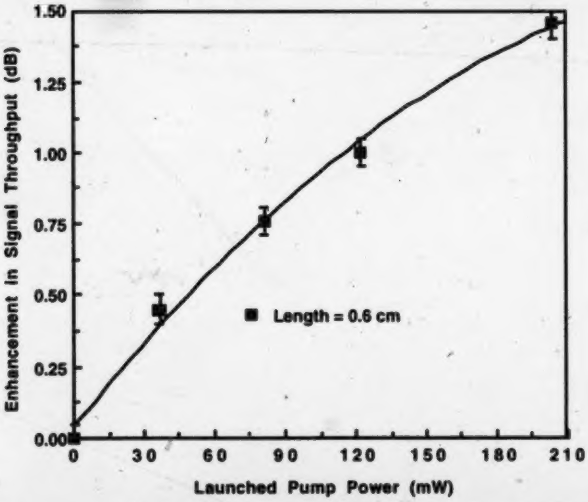

Figure 6.13 Enhancement of Signal Throughput vs. Launched 975nm Pump Power. Experimental result for second batch of erbium-doped, strip-loaded waveguide A.

6.3 Correlating Simulation and Experiment

In this section, experimental results from the previous section will be compared with numerical predictions generated by the model. The material parameters listed in Table 3.5 still hold, with the following exceptions : measured values were used for the metastable state lifetime τ_{21} and the excess loss factors l_s and l_p (from Section 6.2.3). Figure 6.14 compares the signal (λ=1547 nm) throughput enhancement as predicted by the model, with the experimental result from the first batch of erbium-doped strip-loaded waveguides. The functional form of the two curves are similar, although exact numbers differ by up to 0.2 dB. Slight variations between intended design and the fabricated device (in terms of refractive index), local variations in waveguide structure and erbium concentration (due to non-uniformity in sputtering) could account for this discrepancy. Both simulation and experiment confirm that net signal gain isn't feasible at these pump powers due to strong co-operative energy transfer.

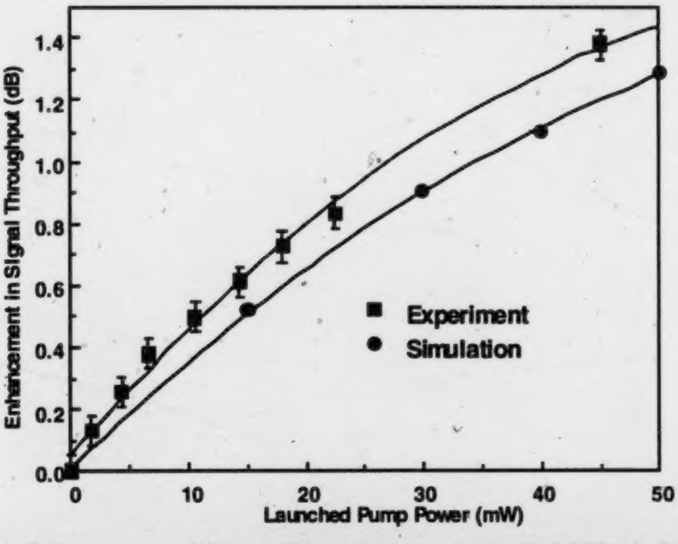

Figure 6.14 Enhancement of Signal Throughput vs. Launched 975 nm Pump Power. Comparison of experimental results and simulation for strip-loaded waveguide A. $P_s(0)$= -8 dBm; $N_{Erb} = 3 \times 10^{26}$ ions/m^3; τ_{21} = 148 μs; l_s=l_p=0.8 dB/cm.

Figure 6.15 predicts enhancement of a signal at peak emission wavelength. In the absence of pump, a net signal loss of 8.8 dB is predicted over 1.2 cm. With 50 mW of 975 nm pump, the loss improves to 5.8 dB. This 3 dB enhancement in signal transmission upon pumping is again in close agreement with the experimentalvalue of 2.9 dB. It should be noted that the net signal loss predicted by the model (8.8 dB) is higher than was observed in the experiment (7.1dB). This is primarily due to the fact that the cut-back loss measurements were performed at 1547 nm, 12 nm away from the peak absorption wavelength for the glass.

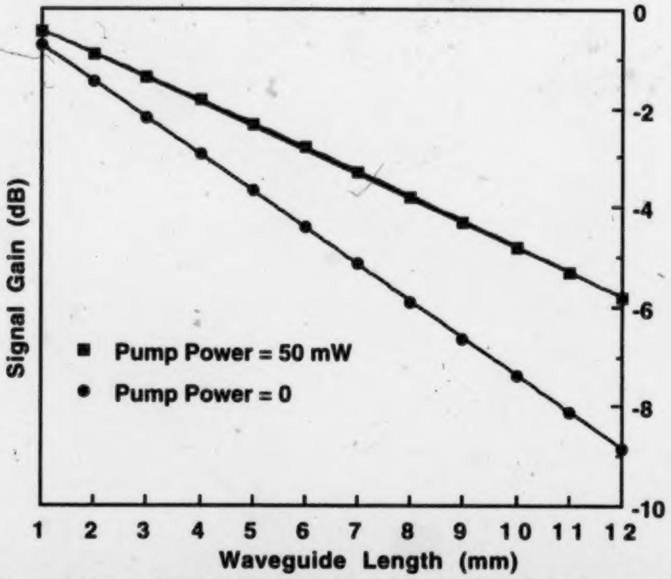

Figure 6.15 Signal Gain vs. Waveguide Length : Simulation of strip-loaded waveguide A. $P_p(0)$=0, 50mW; $N_{Erb} = 3 \times 10^{26}$ ions/m^3; τ_{21} = 148 μs; $l_s = l_p$=0.8 dB/cm.

The typical sequence of device design, simulation, fabrication and testing had to be altered to adapt to limitations imposed by the fabrication process and evolving experimental capabilities. With experiment and simulation now having been mutually validated, the latter was used to forecast improvements. The remainder of this chapter is devoted to simulating strip-loaded waveguide amplifiers. Different designs were explored to assess the viability of using strip-loaded waveguides as amplifiers. Various combinations of rare-earth dopant levels, pump powers and amplifier lengths were explored in an effort to improve device performance.

6.4 Design Options for Rare-Earth-doped Strip-Loaded Waveguides

One obvious area for improvement is the excess waveguide loss factor. Propagation losses of 0.1 dB/cm are commonly reported in waveguides fabricated using PECVD films [41]. Losses below 0.1 dB/cm are apparently feasible FHD [31]. The excess waveguide loss can realistically be brought down to 0.3 dB/cm by successfully annealing the waveguide and/or introducing an upper-cladding. As mentioned in Section 6.2.2, an upper-cladding alone reduced the propagation loss by a factor of two. For an efficient amplifier, the metastable state lifetime τ_{21} should be at least several milliseconds. Improving glass spectroscopy is in the domain of material scientists. In Chapter 3, ytterbium co-doping was shown to improve pumping efficiency for waveguides with high erbium concentrations. With these improvements (l_p=0.3 dB/cm and l_s=0.15 dB/cm; τ_{21}=10 ms; N_{Yb}=10 x 10^{26} ions/m^3), Figure 6.16 predicts a net signal gain of 2 dB in the same strip-loaded waveguide structure which was tested earlier. However, 2 dB of net gain over 1.2 cm is insufficient for applications forseen for these devices.

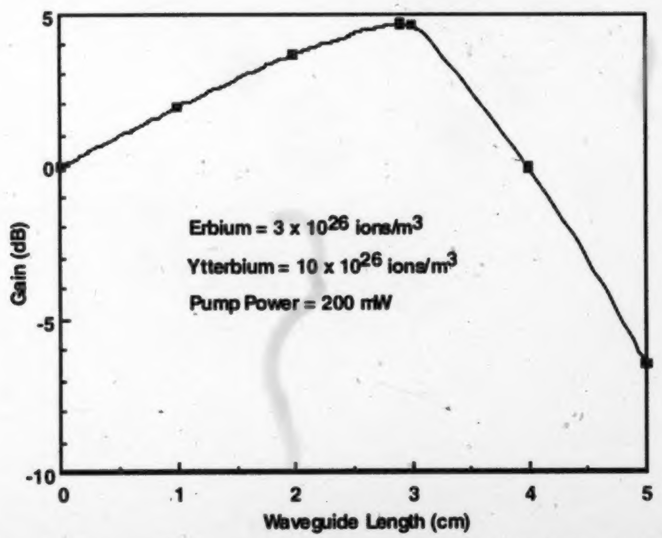

Figure 6.16 Signal Gain vs. Waveguide Length : Simulation of strip-loaded waveguide A. $P_p(0)$=200mW; τ_{21}=10ms; N_{Erb} = 3 x 10^{26} ions/m^3; N_{Yb} = 10 x 10^{26} ions/m^3.

Figures 6.17 & 6.18 predict signal gain of ~20 dB over 10 cm with 500 mW of pump. With 300 mW, a more practical number, 15 dB of gain is predicted over

7.55 cm. It is also worth noting that in the presence of ytterbium, it is actually advisable to lower erbium concentration and increase the optimum amplifier length.

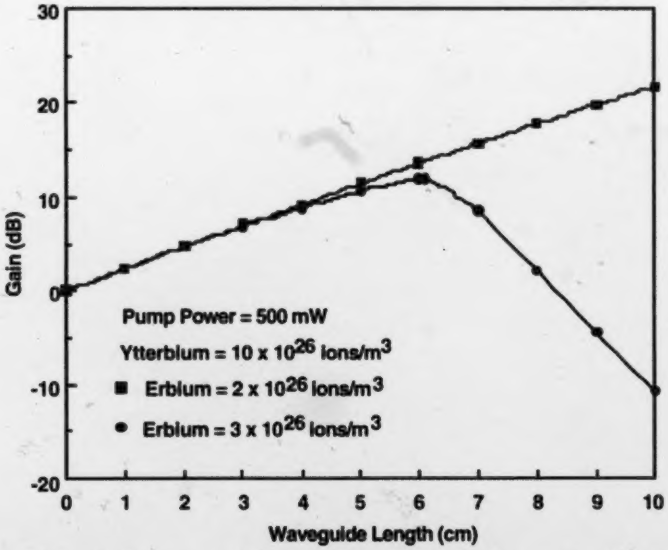

Figure 6.17 Signal Gain vs. Waveguide Length for strip-loaded waveguide A (simulation). $P_p(0)$=500mW; N_{Erb} = 2,3 x 10^{26} ions/m^3; N_{Yb} = 10 x 10^{26} ions/m^3.

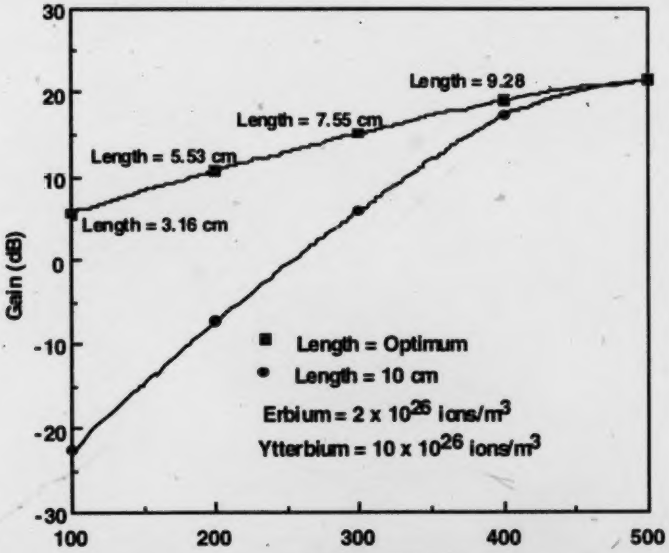

Figure 6.18 Signal Gain vs. Pump Power for strip-loaded waveguide A (Simulation). L = 10cm, Optimized; N_{Erb} = 2 x 10^{26} ions/m^3; N_{Yb} = 10 x 10^{26} ions/m^3.

Having simulated strip-loaded waveguide A under different rare-earth concentrations, pump powers and length, it is now instructive to examine variations in the waveguide cross-section. Since the refractive index of the SiON layer is a flexible parameter, the following questions arise : a) How adversely would raising the SiON index affect amplifier performance? b) Conversely, how much better would the device perform if a rib was to be fashioned directly on the sputtered film (i.e. without a SiON strip-loading layer)? c) How do the noise characteristics compare? To address these issues, and to compare the influence of ytterbium co-doping, the waveguide devices listed in Table 6.2 will be modeled. Relative to Strip-loaded waveguide A (whose modal properties are repeated again for comparison), only the refractive index of the SiON layer was varied.

Waveguide Label	SiON Index	E-Field Overlap Factor Signal Γ_s	 Pump Γ_p	Modal Area Signal	 Pump
Ridge	N/A	76.1%	88.1%	5.3 μm^2	4.5 μm^2
Strip-loaded A	n=1.56	61.4%	73.3%	8.3 μm^2	6.7 μm^2
Strip-loaded B	n=1.59	52.1%	54.2%	10.6 μm^2	9.7 μm^2
Strip-loaded C	n=1.62	39.6%	28.4%	7.5 μm^2	5.6 μm^2

Table 6.2 Waveguide labels, SiON index and corresponding modal properties.

A ridge waveguide formed directly from the sputtered film has a high overlap factor, which would naturally translate to better gain performance and pumping efficiency than any of the strip-loaded devices. However, the modal areas and spot-sizes for the ridge waveguide are small, which tends to increase coupling loss. In the strip-loaded configuration, light propagation is split almost evenly between the two core layers if the SiON index is matched to that of the sputtered film. The effective width of the composite core is double that of the ridge and consequently, the modal areas are twice as large. If the SiON index is increased beyond that of the sputtered film, the SiON becomes the primary waveguide core and reduces the overlap factor significantly. The electric-field contours and normalized intensity profiles for all three devices are illustrated in the following pages.

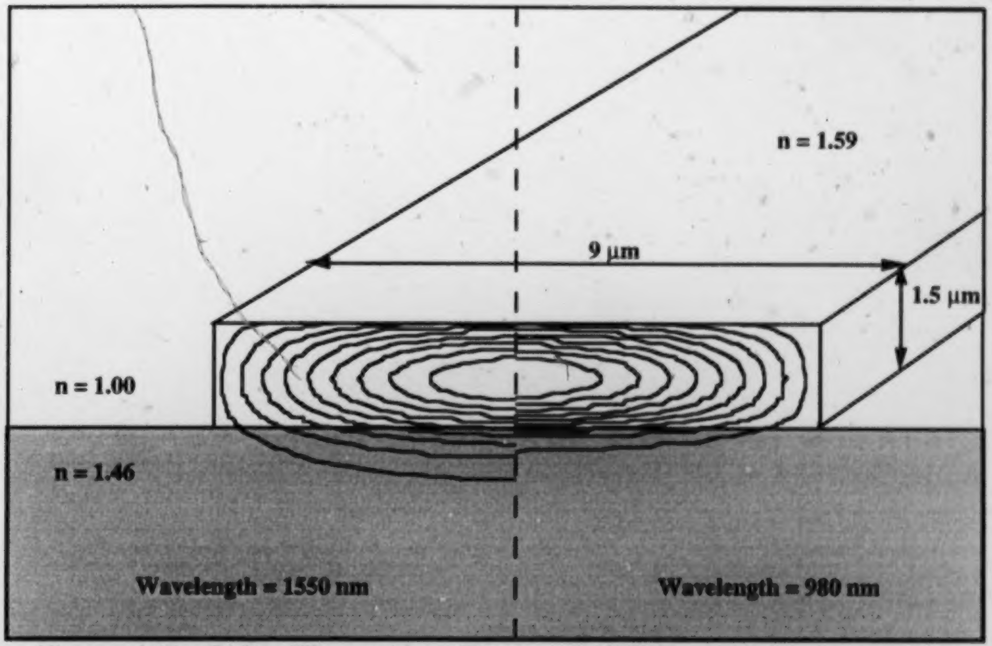
n = 1.59
9 μm
1.5 μm
n = 1.00
n = 1.46
Wavelength = 1550 nm
Wavelength = 980 nm

Figure 6.19 Ridge Waveguide. The un-shaded layer is the rare-earth-doped sputtered film, with index n=1.59; the shaded layer is the SiO_2 cladding with index n=1.46. The TE field contours for the fundamental signal and pump mode are shown on the left and right, respectively. The contours represent 90% to 10% of peak amplitude.

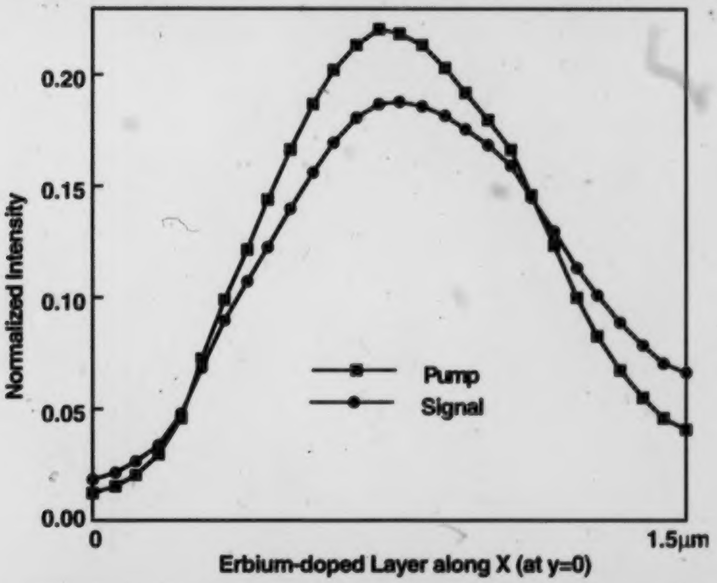

Figure 6.20 Normalized signal and pump intensity profiles along the center of Ridge Waveguide, within the sputtered film.

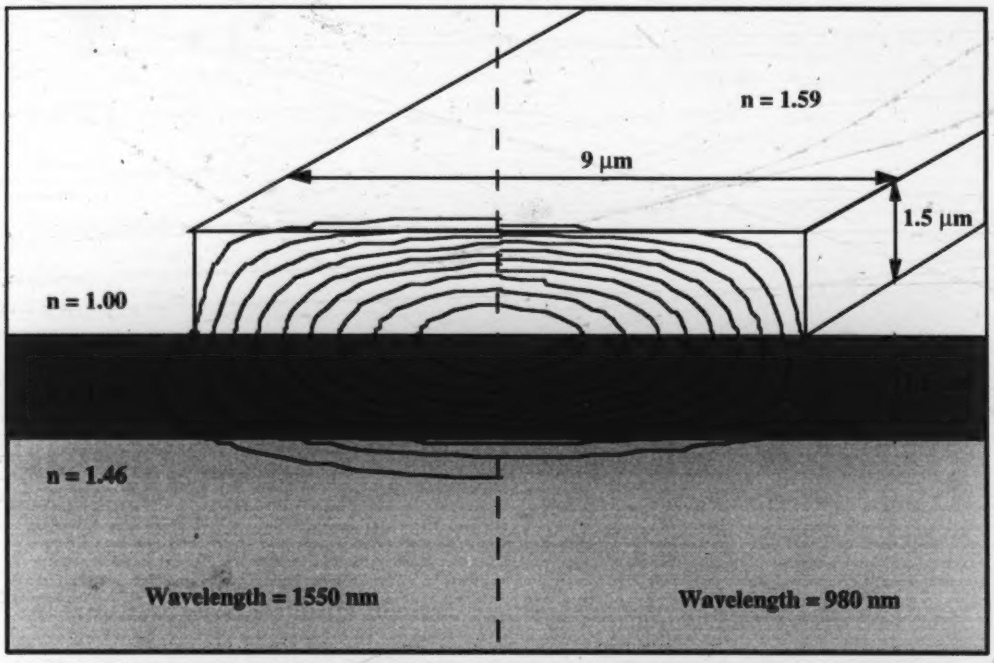
n = 1.59
9 μm
1.5 μm
n = 1.00
n = 1.46
Wavelength = 1550 nm
Wavelength = 980 nm

Figure 6.21 Strip-loaded Waveguide B. The dark-shaded layer is the rare-earth-doped sputtered film, with index n=1.59; the un-shaded layer is the SiON, with index 1.59; the light-shaded layer is the SiO_2 cladding with index n=1.46. The TE field contours for the fundamental signal and pump mode are shown on the left and right, respectively. The contours represent 90% to 10% of peak amplitude.

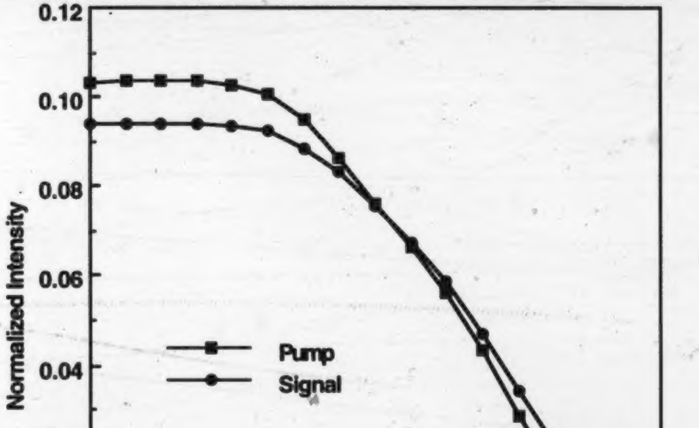

Figure 6.22 Normalized signal and pump intensity profiles along the center of Strip-loaded Waveguide B, within the sputtered film.

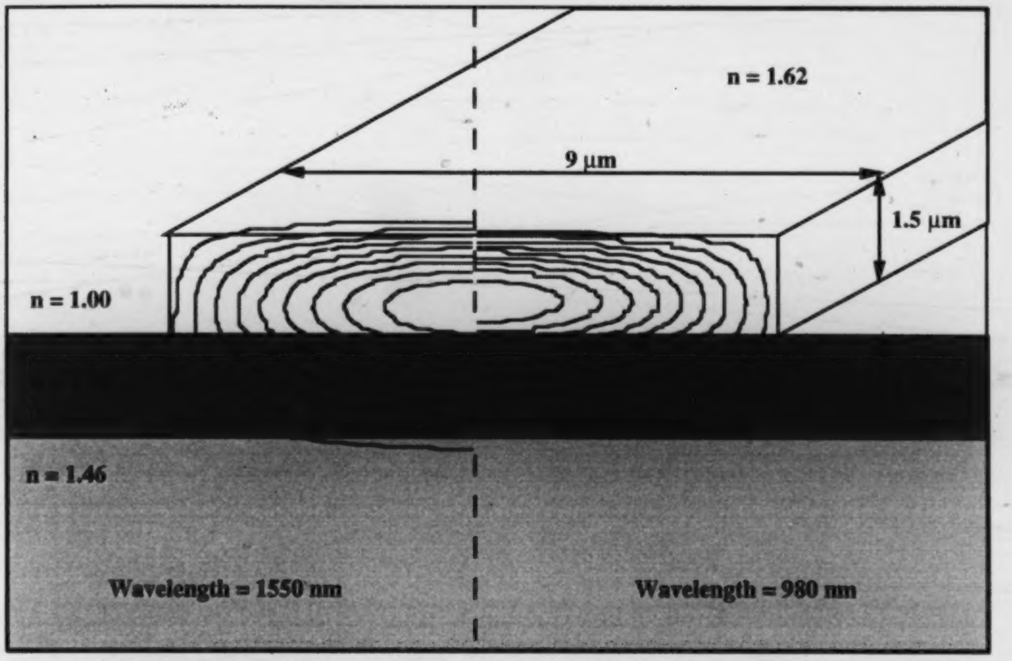
n = 1.62
9 µm
1.5 µm
n = 1.00
n = 1.46
Wavelength = 1550 nm
Wavelength = 980 nm

Figure 6.23 Strip-loaded Waveguide C. The dark-shaded layer is the rare-earth-doped sputtered film, with index n=1.59; the un-shaded layer is the SiON, with index 1.62; the light-shaded layer is the SiO_2 cladding with index n=1.46. The TE field contours for the fundamental signal and pump mode are shown on the left and right, respectively. The contours represent 90% to 10% of peak amplitude.

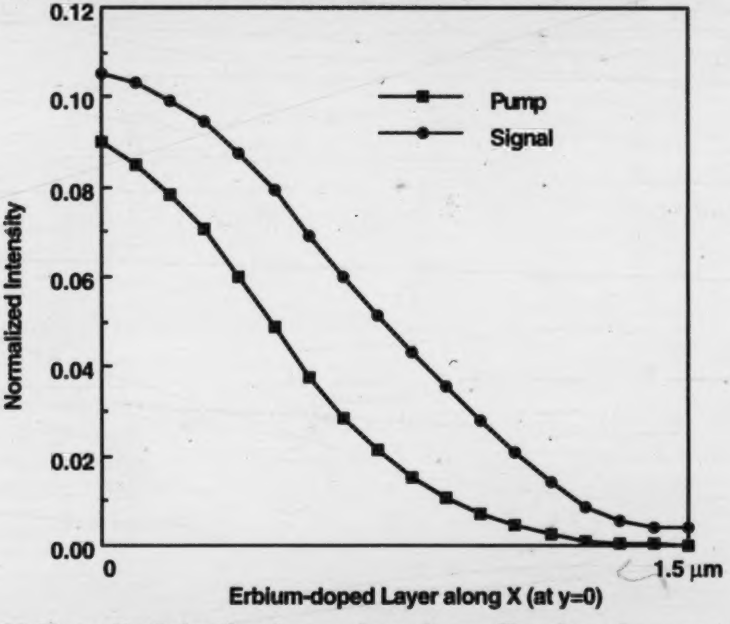

Figure 6.24 Normalized signal and pump intensity profiles along the center of Strip-loaded Waveguide C, within the sputtered film.

Figures 6.25 and 6.26 compare the predicted gain performance of the devices listed in Table 6.2 for short lengths (<5 cm), high erbium concentration (2-3 x 10^{26} ions/m^3) and an input pump power of 200 mW.

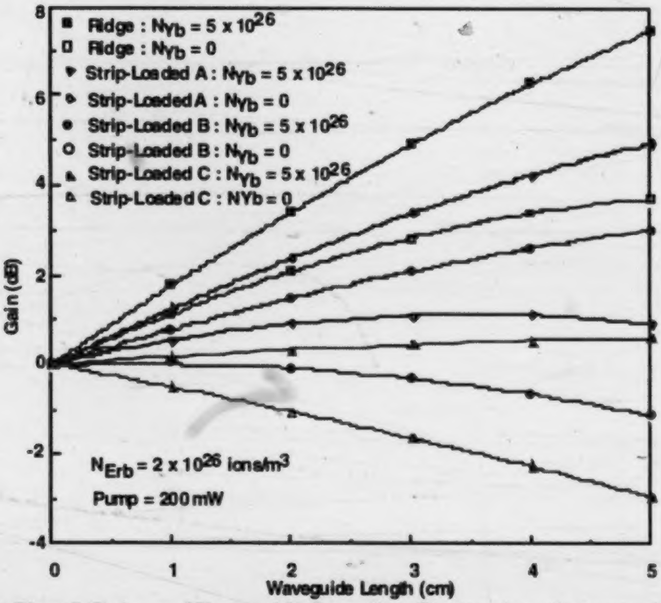

Figure 6.25 Signal Gain vs. Waveguide Length : Comparison between Ridge, Strip-loaded waveguides A, B, and C. $P_p(0)$ = 200 mW; N_{Erb} = 2 x 10^{26} ions/m^3.

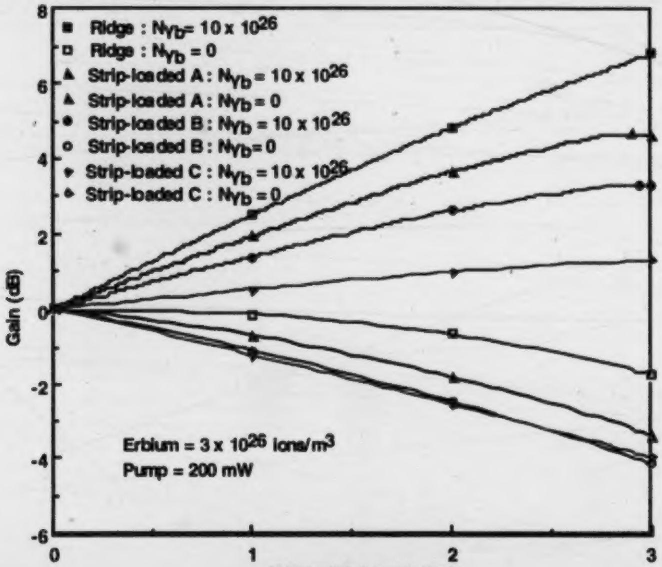

Figure 6.26 Signal Gain vs. Waveguide Length : Comparison between Ridge, Strip-loaded waveguides A, B, and C. $P_p(0)$ = 200 mW; N_{Erb} = 3 x 10^{26} ions/m^3.

According to these results, ytterbium co-doping improves signal throughput in all of the devices (by 3.7-4.2 dB over 5 cm for $N_{Erb} = 2 \times 10^{26}$ ions/m^3; by 5-8 dB over 3 cm for $N_{Erb} = 3 \times 10^{26}$ ions/m^3). For strip-loaded waveguides B and C, where the overlap factors are low, this improvement constitutes the difference between net loss and net gain. Over 5 cm, the signal gain predicted for strip-loaded waveguide A is only ~2.5 dB lower than that of the ridge waveguide. Less than 8 dB of signal gain is forecast in all cases.

For the same erbium dopant levels, Figures 6.27 and 6.28 compare predicted gain performance over 10 cm with 500 mW of pump. Since energy transfer between erbium ions is dependent on concentration, the steady-state population inversion achieved at such high pump powers is not significantly different for the two erbium dopant levels considered. Hence, the gain observed through 5 cm in each device is roughly the same, regardless of the erbium concentration. Since pump depletion is more rapid at higher rare-earth concentrations, it is advisable to lower the dopant level to 2×10^{26} ions/m^3 and sustain population inversion/stimulated emission over longer distances (as in Figure 6.27).

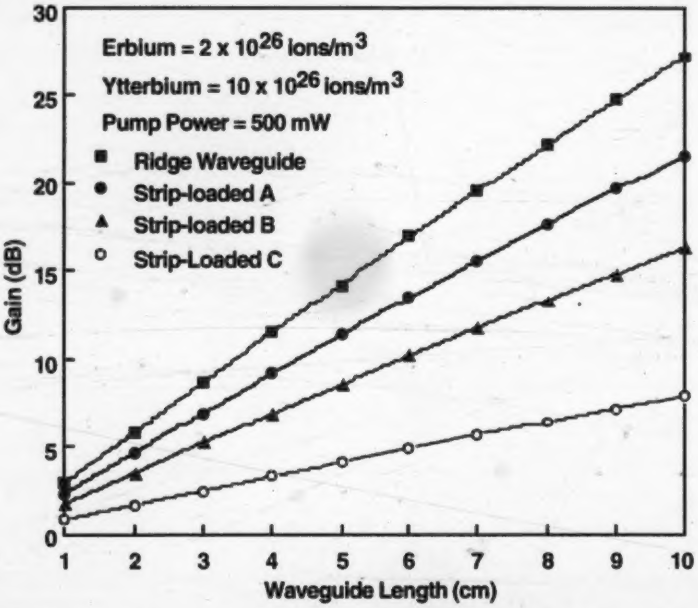

Figure 6.27 Signal Gain vs. Waveguide Length : Comparison between Strip-loaded waveguides A, B, C and Ridge Waveguide. $P_p(0)$=500mW; $N_{Erb} = 2 \times 10^{26}$ ions/m^3.

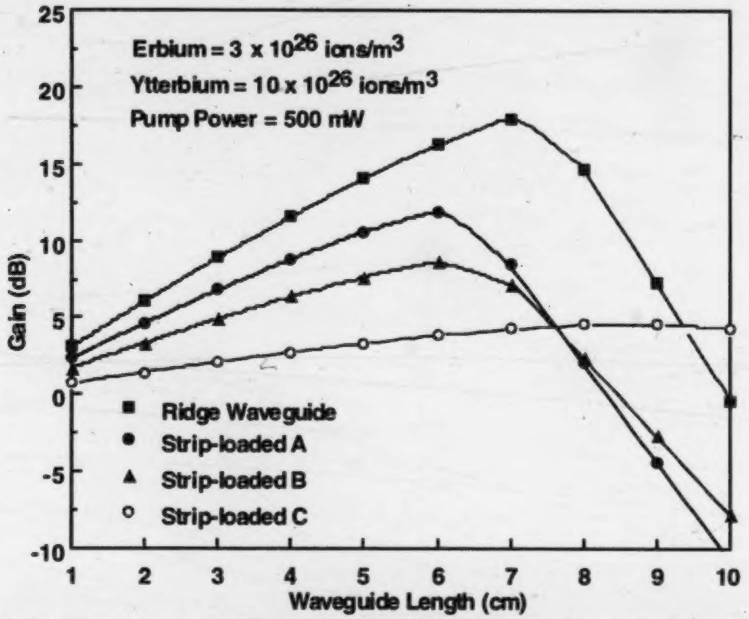

Figure 6.28 Signal Gain vs. Waveguide Length : Comparison between Strip-loaded waveguides A, B, C and Ridge Waveguide. $P_p(0)$=500mW; N_{Erb} = 3 x 10^{26} ions/m^3.

Table 6.3 lists the optimum operating length for each device for various input pump powers. The corresponding signal gain is plotted in Figure 6.29.

Waveguide Label	Optimum Amplifier Length (cm)				
	$P_p(0)$ = 100mW	200mW	300mW	400mW	500mW
Ridge	3.79	6.57	8.87	10.82	12.48
Strip-loaded A	3.16	5.53	7.55	9.28	10.82
Strip-loaded B	3.28	5.66	7.7	9.46	11.00
Strip-loaded C	5.23	8.68	11.36	13.6	15.53

Table 6.3 Optimum amplifier lengths for Strip-loaded waveguides A, B, C, and Ridge waveguide for various $P_p(0)$. N_{Erb} = 2 x 10^{26} ions/m^3; N_{Yb} = 10 x 10^{26} ions/m^3.

The optimum length for strip-loaded device C tends to be longer than device A because pump depletion occurs more gradually (owing to weaker overlap). However, results for the ridge waveguide illustrate that the percentage of overlap is not the only factor in determining pump depletion. Although a greater percentage of light overlaps with rare-earth ions in the ridge configuration, pump depletion in the ridge (9.1 dB over 10 cm for $P_p(0)$=500 mW) is less severe than in strip-loaded waveguides A (13.9 dB) and B (13.1 dB). This is a direct consequence of population inversion. Under conditions of strong inversion, there are fewer ground-state erbium ions along the waveguide. By virtue of its modal structure, population inversion in the ridge waveguide is higher than in any of the strip-loaded devices. For strip-loaded waveguide C, the extremely low mode-overlap (28%) appears to be the overriding factor in determining pump throughput. Despite weak population inversion, pump depletion (6.7 dB) in device C is predicted to be the least severe among the four.

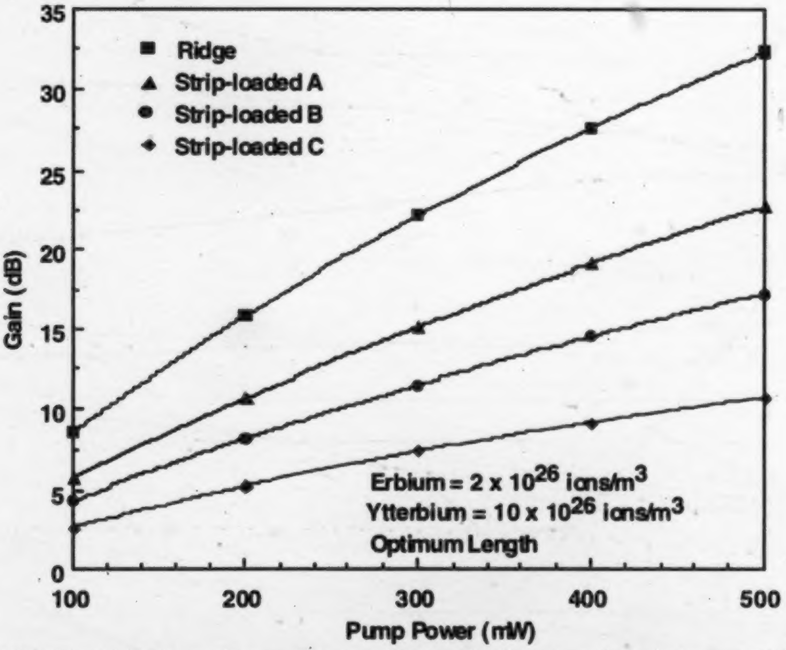

Figure 6.29 Signal Gain vs. Pump Power : Theoretical comparison between Strip-loaded waveguides A, B, C, and Ridge waveguide. Length Optimized.

From Figures 6.25-6.29 and Table 6.3, index-loading and gain performance can be related through a general rule of thumb : for each change in waveguide design (from ridge to strip-loaded A to strip-loaded B), a penalty of ~0.5 dB/cm is incurred in terms of the gain coefficient (provided the amplifiers are at or below optimum length). A further penalty of 0.7 dB/cm is incurred for strip-loaded waveguide C.

Table 6.4 compares broad-band ASE power, in-band ASE power and the output signal-to-noise (SNR) ratio for the various waveguide structures. With 500 mW of pump power over 10 cm, all of the devices are operating below optimum length. Therefore, re-absorption of ASE does not influence the comparison. The SNR drops by 4-6 dB for each regressive change in waveguide design.

Waveguide Label	Broadband ASE	In-band ASE	Output SNR
Ridge	-19.4 dBm	-35.6 dBm	32.8 dB
Strip-loaded A	-20.3 dBm	-36.5 dBm	28.1 dB
Strip-loaded B	-21.3 dBm	-37.6 dBm	23.9 dB
Strip-loaded C	-24.0 dBm	-40.3 dBm	18.2 dB

Table 6.4 Broad-band ASE Power, In-band ASE Power and Output SNR for Strip-loaded waveguides A, B, C, and Ridge waveguide. $L = 10$ cm; $P_p(0) = 500$ mW; $N_{Erb} = 2 \times 10^{26}$ ions/m^3; $N_{Yb} = 10 \times 10^{26}$ ions/m^3.

In terms of gain and noise, strip-loaded waveguide A comes closest to matching the performance of the ridge waveguide. Device B fares worse in comparison to both. For a pump power of 300 mW, the ridge waveguide is predicted to yield a net gain of 22 dB (gain coefficient of ~ 2.5 dB/cm; pumping efficiency of 0.073 dB/mW) and SNR better than 33 dB. For the same pump power, gain of 15 dB (gain coefficient of ~ 2 dB/cm; pumping efficiency of 0.05 dB/mW) and SNR better than 28 dB is predicted for strip-loaded waveguide A. This penalty in device performance could be worth paying in return for a uniform layer-structure across the wafer.

Eventually, these waveguide amplifiers would have to be integrated with other passive devices (such as WSCs, splitters, switches, etc.) on a single substrate, as shown in Figure 6.30. If the amplifier is formed in the ridge configuration, deposition of the sputtered rare-earth-doped film would have to be confined to a specific region of the wafer. A different material would have to be deposited in the adjoining regions to fabricate the passive devices. To form optical waveguides, the two sections would have to be micromachined separately. Ideally, this task should involve a single photolithographic and micromachining step. The layer structure for strip-loaded waveguides would make this possible, especially if SiON is used as the passive film.

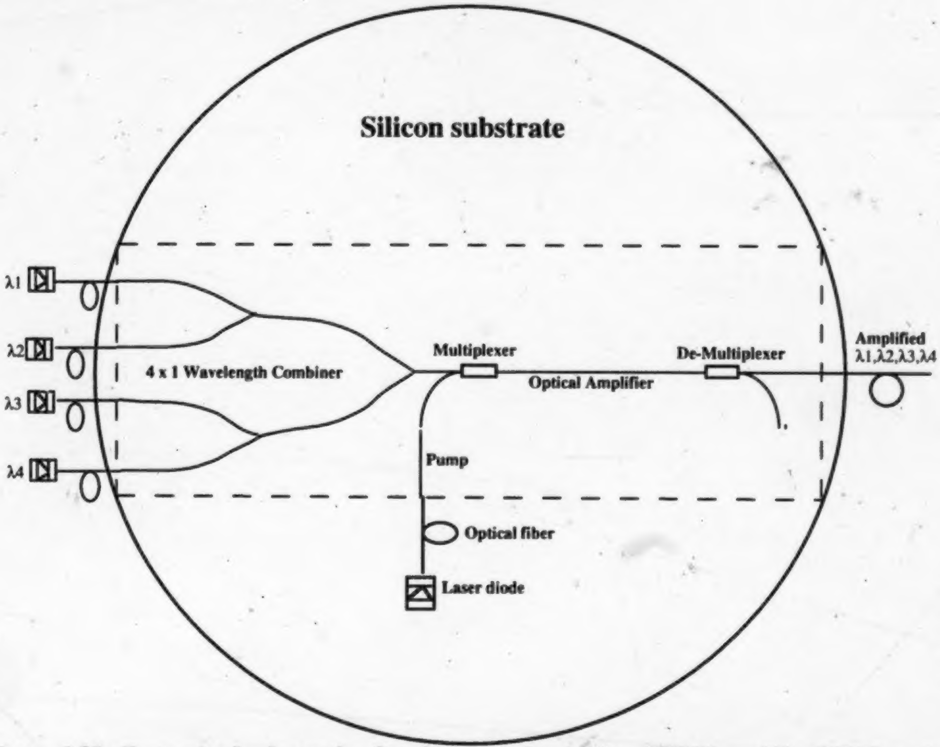
Silicon substrate
λ1
λ2
λ3
λ4
4 x 1 Wavelength Combiner
Multiplexer
Optical Amplifier
De-Multiplexer
Amplified
λ1,λ2,λ3,λ4
Pump
Optical fiber
Laser diode

Figure 6.30 Conceptual schematic of an integrated combiner/WSC/amplifier/WSC module

For the optical amplifier segment, the index of the SiON layer can be lowered below that of the sputtered film to allow for significant interaction between light and the rare-earth ions. In other regions, the index of the the SiON can be made as high as n=2.0, thus reducing the underlying rare-earth-doped film to a low-absorption cladding. The refractive index can be selectively controlled by changing gas flow rates inside the PECVD chamber. These index variations do not affect micromachining characteristics. Since the thickness of the SiON film will be uniform over all parts of the wafer, ribs can be etched on SiON using a single etch-step. Depending on the location over the wafer, SiON ribs would function either as index-loading layers for the amplifier or as passive, ridge waveguides.

Chapter 7 : Evanescent Pumping of Rare-Earth-Doped Bulk Glass Using Dispensed Polymer Waveguides - Fabrication and Modeling

7.1 Introduction

Given that waveguide fabrication through thin-film deposition and micromachining resulted in devices with poor spectroscopic properties and optical quality, alternative approaches were sought. A rare-earth-doped bulk glass with a longer luminescence lifetime was obtained from a different manufacturer. Instead of using this bulk glass as a source material for thin-film sputtering, an optical waveguide was formed directly atop the bulk glass by dispensing a polymer. Although the passive polymer acts as the primary waveguiding layer, the evanescent field (please refer to Chapter 2) of the pump and signal modes extend down into the bulk glass to provide excitation and emission. Issues related to evanescently-pumped waveguides formed on rare-earth-doped bulk glasses - fabrication, testing and design options - are discussed in this chapter. This is a pre-cursor to the next chapter, where optical waveguides are formed within rare-earth-doped bulk glass through an ion-exchange process.

7.2 Polymer Waveguide on top of Er/Yb Bulk Glass : Experimental Results

7.2.1 Fabrication

Polymer waveguides are attractive because of their low loss, low cost and ease of fabrication. Typically, they have been used as multimode (MM) step-index structures for optical interconnects in hybrid integrated circuits [68]. Recently, graded-index MM polymer waveguides [69,70] and a planar, graded effective index MM polymer waveguide [71] have been reported. The latter are formed by a simple dispensing technique. The parabolic surface of the polymer was found to produce a near-quadratic index waveguide, thus confining light within a region narrower than the overall waveguide dimension. Conceivably, such waveguides may be formed over long distances (0.5 m).

For these experiments, an erbium / ytterbium co-doped phosphate bulk glass (n = 1.53) was purchased from Kigre Inc [72]. The precise dopant levels for the glass (named QX/Er) were unavailable but the erbium content was known to be in the 0.1-0.2 wt% range and the ytterbium content approximately a factor of 15 higher. A 1 in x 1 in x 2 cm transmission sample of the QX/Er was sliced to a 2 mm thick piece. Both top and bottom surfaces of this glass were polished to optical standards. Using a pressurized syringe under computer control [73], an optical adhesive (NOA 81) was dispensed directly on the erbium-doped glass. The NOA 81 was cured by exposure to UV-light to form a polymer of refractive index 1.56. The resulting parabolic polymer waveguide had a maximum height of 8 μm and a base width of 180 μm (Figure 7.1). Input and output facets were obtained by scribing and cleaving the glass substrate and the resulting waveguides were 1cm long.

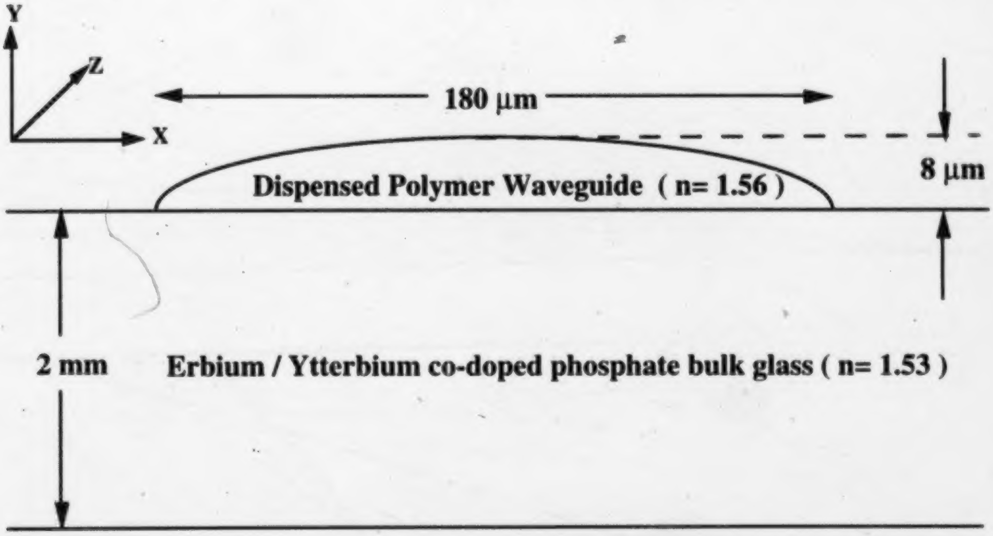
Y
Z
X
180 μm
8 μm
Dispensed Polymer Waveguide (n= 1.56)
2 mm
Erbium / Ytterbium co-doped phosphate bulk glass (n= 1.53)

Figure 7.1 Schematic of polymer waveguide dispensed on bulk glass.

The aspect ratio of a waveguide formed by this method is determined by the contact angle at the edge, which is a function of the surface tensions at the liquid/air and liquid/glass interfaces. Each polymer/substrate combination has a relatively constant aspect ratio over a wide range of waveguide dimensions. The process is highly repeatable. For example, in an array of 100 microlenses formed by this technique, the standard deviation in focal length was found to be approximately 1% [74].

7.2.2 Passive Optical Properties

As in the case of the strip-loaded devices, several passive optical properties of the dispensed polymer waveguide are of interest - the number, shape and size of the vertical modes, the amount of mode in the substrate, and the overlap between the 980 nm pump and the 1547 nm signal mode in the erbium/ytterbium glass. In Chapter 2, the sequence of steps involved in analysing rectangular waveguides was outlined. For waveguides with parabolic cross-sections, such as in Figure 7.1, the formulation of the problem and its solution is slightly more complicated and is best handled through the *effective-index method* [5].

The effective-index method breaks down a two-dimensional problem into two one-dimensional problems. At various points along the lateral direction x, the dispensed polymer and the underlying bulk glass are analysed as thin one-dimensional slabs stacked up along the vertical (y) direction. Given the parabolic profile of the dispensed polymer, the thickness of the polymer slab will be unique for each lateral position x. Consequently, the solution to the wave equation and the effective propagation constant β will also be unique at each x. After generating a series of $\beta(x)$'s, the waveguide is analysed as a collection of slabs, each with effective index $[n(x)= \beta(x)/k_0]$, stacked side-by-side along x. The discrete β's that satisfy the wave equation and the boundary conditions for this configuration are the solutions to the two-dimensional structure. My colleague David Boertjes, who collaborated with me on a paper (on which this chapter is based), had developed an effective-index algorithm to compute mode profiles and propagation constants for dispensed polymer waveguides. He used this to compute the mode profiles and overlap factors for the waveguide shown in Figure 7.1. The contour lines for the fundamental pump and signal modes are re-produced from our joint manuscript (Figure 7.2). This picture serves to illustrate how the parabolic profile creates a graded-index effect along the lateral direction and helps confine the mode-field to a much narrower width (~40 μm) than the physical dimension of the polymer (180 μm).

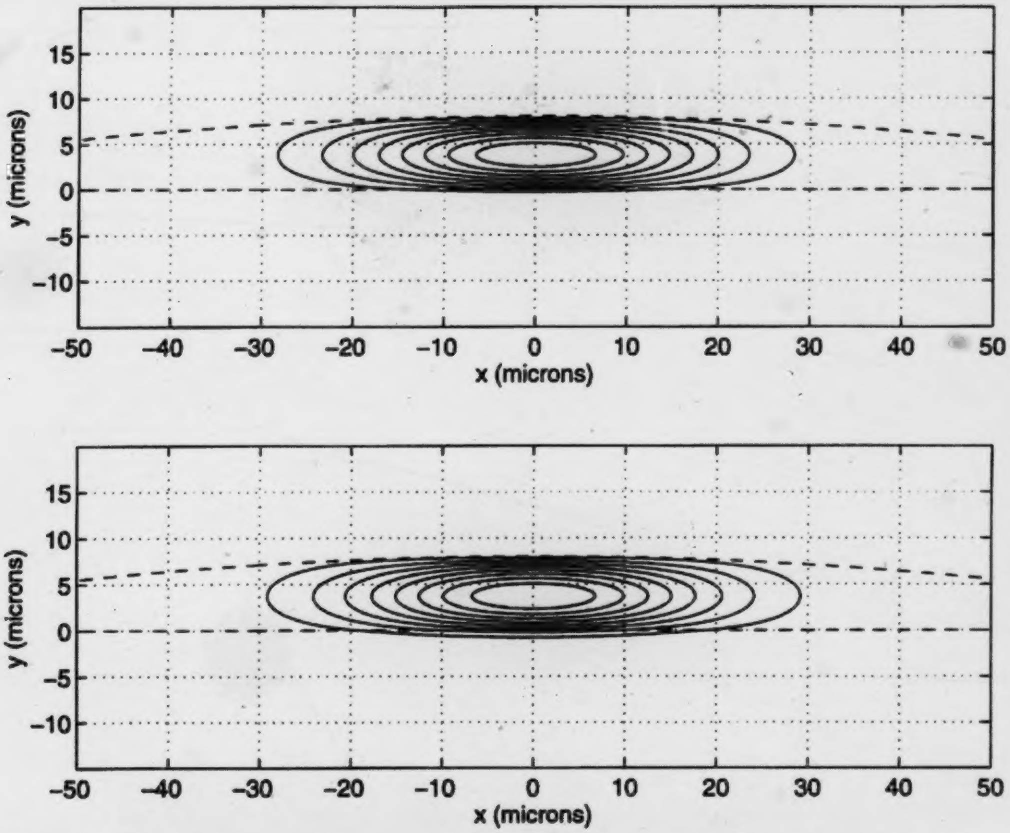

Figure 7.2 Fundamental pump (above) and signal (below) mode-profile for dispensed polymer waveguide shown in Figure 7.1.

As evidenced from previous chapters, the percentage of pump and signal field that overlaps with the erbium/ytterbium glass is of great importance. The overlap factor for the fundamental mode was estimated to be only 0.21 and 0.74 for pump and signal, respectively. However, this waveguide structure supports five modes at the pump wavelength and three modes at the signal wavelength. The fields of higher order modes extend deeper into the bulk substrate.

7.2.3 Active Optical Properties

The experimental set-up used to study the active properties of the dispensed polymer waveguide is illustrated in Figure 7.3.

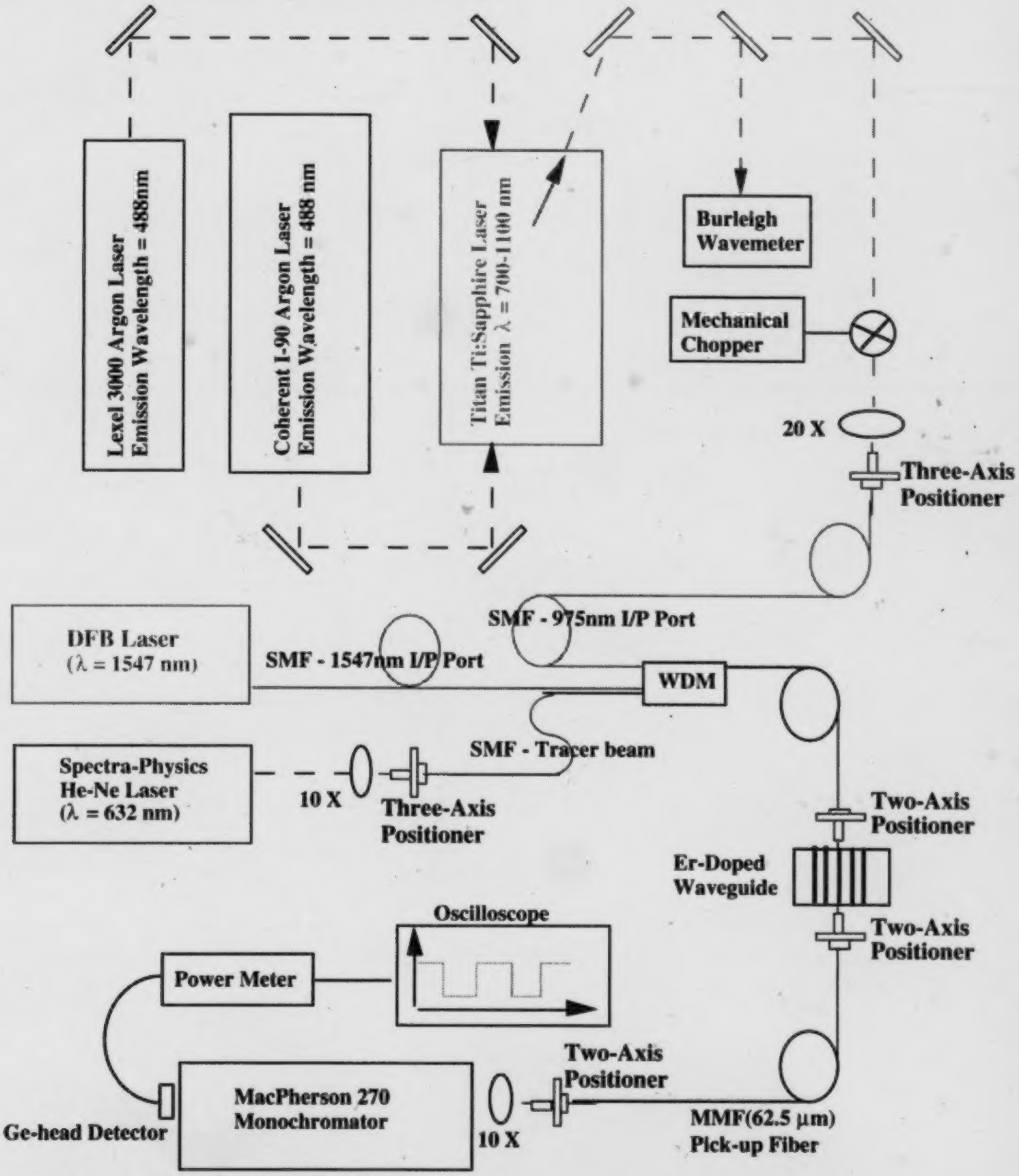
Lexel 3000 Argon Laser
Emission Wavelength = 488nm
Coherent I-90 Argon Laser
Emission Wavelength = 488 nm
Titan Ti:Sapphire Laser
Emission λ = 700-1100 nm
Burleigh Wavemeter
Mechanical Chopper
20 X
Three-Axis Positioner
DFB Laser
(λ = 1547 nm)
SMF - 975nm I/P Port
SMF - 1547nm I/P Port
WDM
SMF - Tracer beam
Spectra-Physics He-Ne Laser
(λ = 632 nm)
10 X
Three-Axis Positioner
Two-Axis Positioner
Er-Doped Waveguide
Two-Axis Positioner
Oscilloscope
Power Meter
Two-Axis Positioner
MacPherson 270 Monochromator
Ge-head Detector
10 X
MMF(62.5 μm) Pick-up Fiber

Figure 7.3 Experimental set-up to study active properties of polymer waveguides dispensed on QX/ER bulk glass.

The Ti:Sapphire crystal was pumped from opposite ends with two 5 watt Argon lasers. The output from the Ti:Sapphire was combined with a signal from a 1547 nm DFB laser using a fiber WSC. A Helium-Neon laser was used as a visual aid when aligning fiber to waveguide. The output pigtail of the WSC was butted to the input facet of the polymer/glass waveguide. A multimode fiber was used at the output facet of the waveguide to gather light which was then filtered using a monochromator and subsequently detected.

The spontaneous emission spectrum in the 1520-1570 nm wavelength region, observed with 210 mW of 980 nm pump power launched into the waveguide, is shown in Figure 7.4.

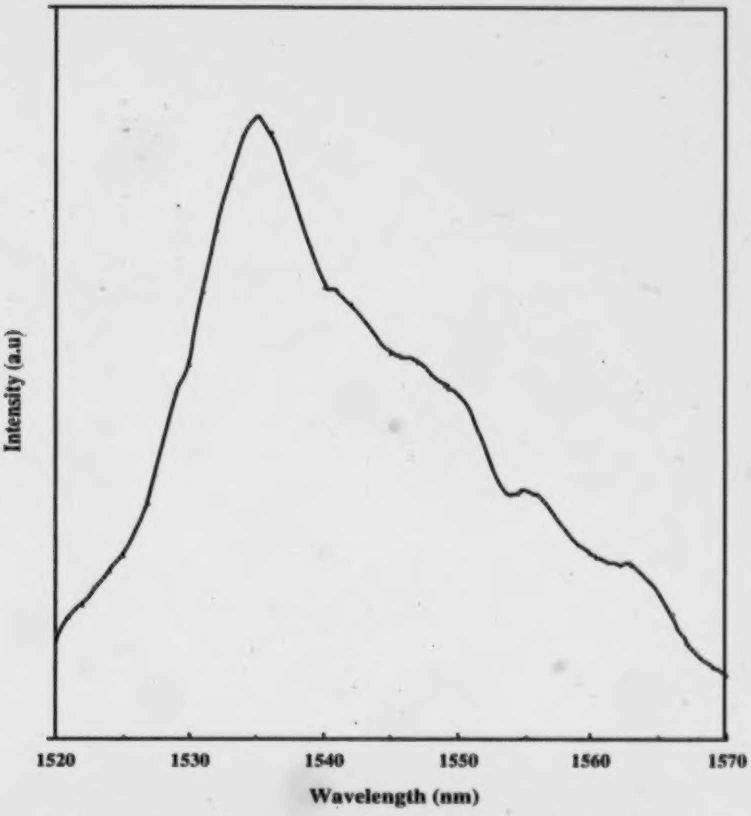

Figure 7.4 Spontaneous emission spectrum observed in polymer waveguide dispensed on QX/ER bulk glass.

Unlike the Schott Glass product studied in the previous chapter, this glass had only one sharp emission peak, at 1535 nm. Bright green light was visible throughout the length of the waveguide. Given the low erbium content in this glass, it is believed that green fluorescence is caused by Excited State Absorption (ESA) of pump photons from the $^4I_{11/2}$ level, rather than co-operative upconversion. The intensity of the green light did not diminish significantly when the Ti:Sapphire was tuned to wavelengths between 900 nm and 1000 nm, which corresponds to the wide absorption band of ytterbium. By chopping theTi:Sapphire beam at 50 Hz and observing the luminescence decay charateristics on an oscilloscope (Figure 7.5), the lifetime for spontaneous emission in this waveguide was estimated to be 8 ms (with 210 mW of launched pump power).

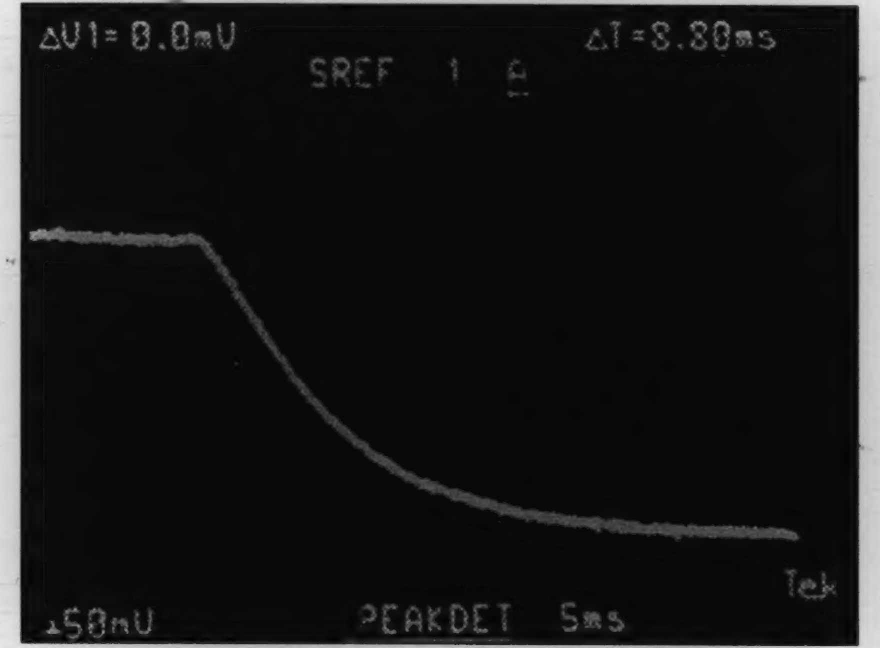

Figure 7.5 Lifetime of spontaneous emission for polymer waveguide dispensed atop QX/ER bulk glass.

Given the short length of the device, losses could not be measured using the cut-back technique. However, fiber-to-fiber losses were measured at three wavelengths to separate the insertion losses from the losses due to the erbium. The throughput loss was 4.2 dB @ 1300 nm, 5.8 dB @ 1547 nm and 4.5 dB @ 980 nm. Since neither erbium nor ytterbium has an absorption band near 1300 nm, the losses at that wavelength were attributed to coupling losses at the two end-facets and the losses inherent to the polymer waveguide. The coupling loss was likely higher than the 3 dB estimate since the cleaved end facets were tilted a few degrees from the ideal orientation. The on-chip erbium-induced loss was estimated to be approximately 1.6 dB @ 1547 nm and 0.3 dB @ 980 nm.

The enhancement of a transmitted signal at a wavelength of 1547 nm was studied. The 1547 nm laser diode was modulated at a frequency of 2kHz so that amplified spontaneous emission could be ignored during the pump-probe measurements. The attenuation of the signal was found to decrease by a maximum of 1.7 dB when pumped with an estimated 210 mW. The relationship between transmitted signal enhancement and residual pump power exiting the waveguide is shown in Figure 7.6. The onset of saturation at high pump power suggests that the maximum signal enhancement was obtained for this device.

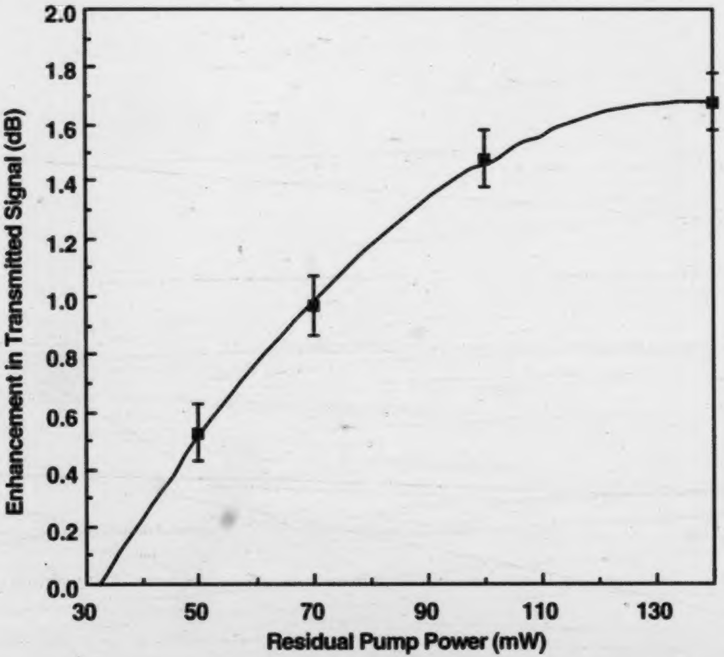

Figure 7.6 Enhancement in Trasmitted Signal vs. Residual Pump Power for polymer waveguide dispensed atop QX/ER bulk glass.

The 1.7 dB of enhancement in signal transmission upon pumping compensates for the on-chip loss but not the coupling losses. These experimental results were not verified by the model for the following reasons : 1) the precise dopant levels were unknown. 2) the model is limited by the fact that it only accounts for one propagating mode at each wavelength. 3) the optical power distribution among the various excited modes was unknown. 4) the analysis would have been computationally intensive, given the number of finite elements required to model a waveguide of large dimensions.

7.3 Design Options for Evanescently-Pumped Waveguide Amplifiers

Evanescently-pumped rectangular waveguides were modeled for their potential use as amplifiers. Two waveguide designs (Evanescent A&B) with markedly different overlap factors were considered. They are shown in Figures 7.7-7.8, along with their signal and pump mode-field (TE) contours. The dimensions and indices were chosen to make both structures single-moded at signal and pump wavelengths.

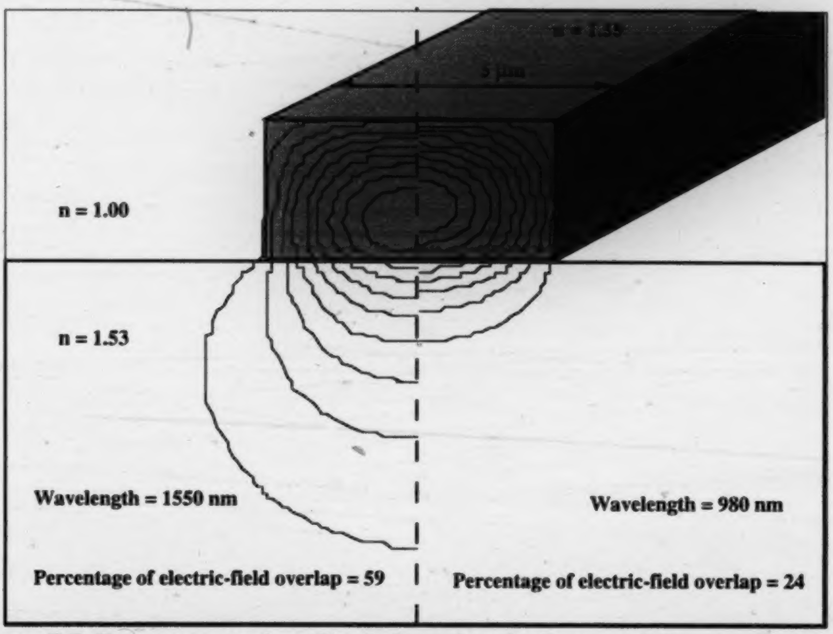

n = 1.55
5 µm
n = 1.00
n = 1.53
Wavelength = 1550 nm
Wavelength = 980 nm
Percentage of electric-field overlap = 59
Percentage of electric-field overlap = 24

Figure 7.7 Evansescent A - Shaded region is 5 µm x 2.5 µm passive rib with n=1.55; un-shaded region is 2mm thick rare-earth-doped bulk substrate (n=1.53).

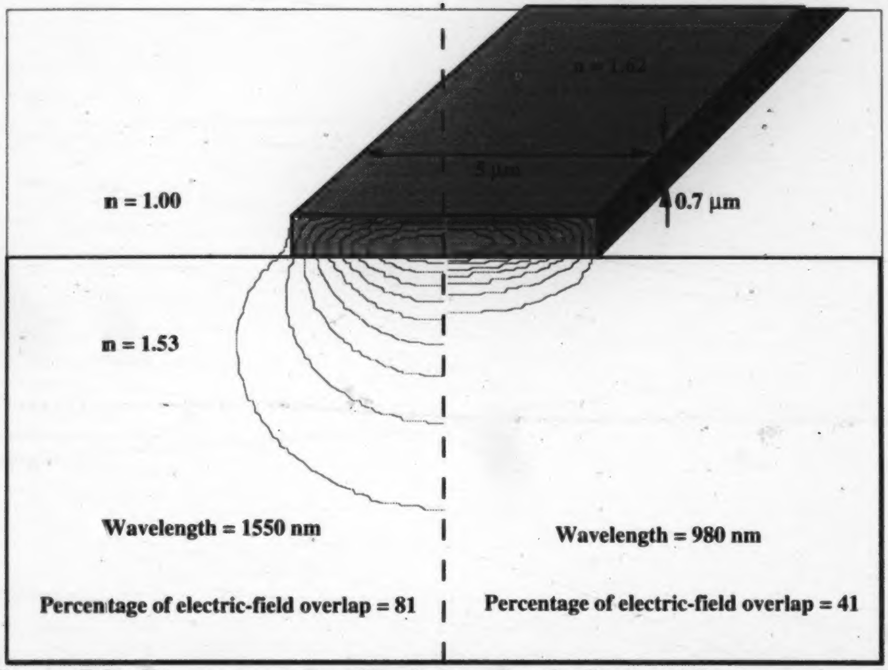
n = 1.62
5 µm
n = 1.00
0.7 µm
n = 1.53
Wavelength = 1550 nm
Wavelength = 980 nm
Percentage of electric-field overlap = 81
Percentage of electric-field overlap = 41

Figure 7.8 Evansescent B - Shaded region is 5µm x 0.7µm passive rib (n=1.62); un-shaded region is 2mm-thick rare-earth-doped bulk substrate (n=1.53).

The numerical model was used to compare device performance for various erbium/ytterbium dopant levels and pump powers. Assuming an input pump power of 500 mW and a ytterbium concentration of 10 x 10^{26} ions/m^3, the optimum erbium concentration for device A was found to be ~1 x 10^{26} ions/m^3 (Figure 7.9). For concentrations above this value, signal gain is severely reduced due to : 1) upconversion and 2) signal absorption in unpumped regions deep inside the substrate, where pump mode-field lines do not penetrate but signal mode-field lines do. The latter is a common and unavoidable feature of all evanescently-pumped amplifiers. For erbium concentrations lower than 1 x 10^{26} ions/m^3, population inversion and gain coefficients are reduced. It may be posited that equivalent gain could still be accumulated over longer distances. For an erbium dopant level of 0.5 x 10^{26} ions/m^3, the optimum length would ostensibly be 50 cm (or twice that for 1 x 10^{26} ions/m^3). However, excess propagation losses come into play and reduce the amplifier length to ~ 32 cm and the gain to ~ 5 dB.

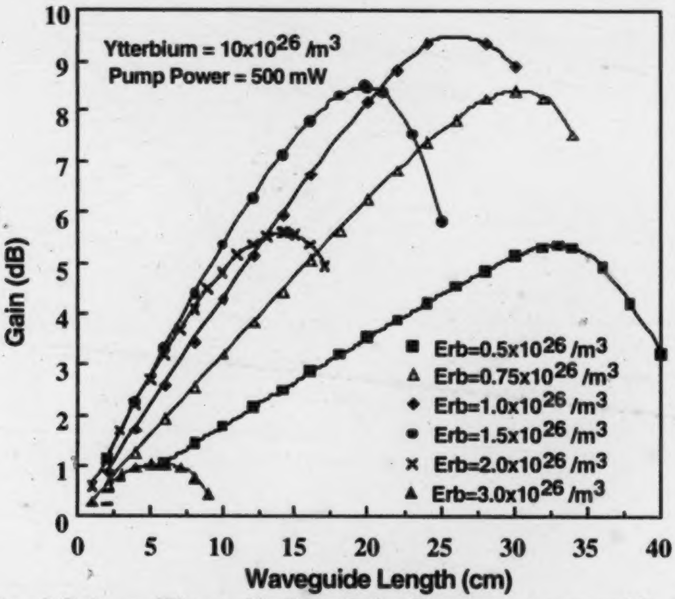

Figure 7.9 Signal Gain vs. Waveguide Length for Evanescent waveguide A : $P_p(0) = 500$ mW; $N_{Yb} = 10 \times 10^{26}$ ions/m^3; N_{Erb}=varies.

For device A, the dependence on ytterbium concentration is examined in Figure 7.10, assuming optimum erbium concentration and pump power of 500 mW.

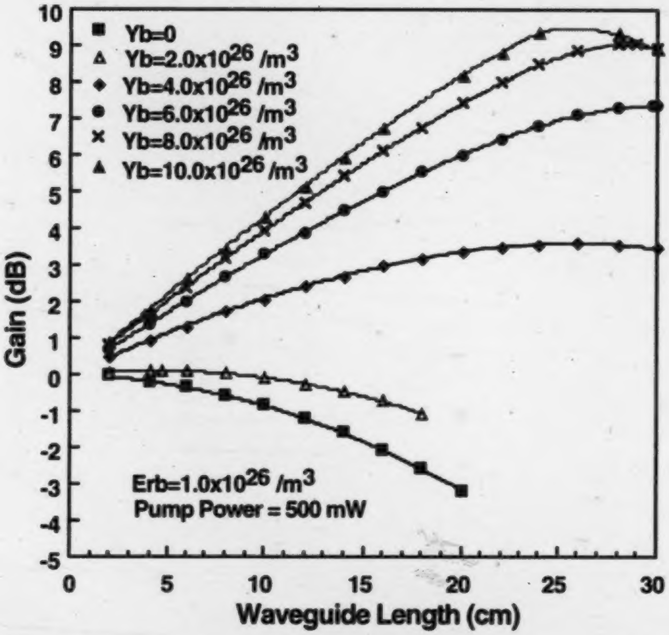

Figure 7.10 Signal Gain vs. Waveguide Length for Evanescent waveguide A : $P_p(0) = 500$ mW; $N_{Erb} = 1 \times 10^{26}$ ions/m^3; N_{Yb}=varies.

Figure 7.10 confirms that the presence of ytterbium provides the additional pumping necessary to overcome upconversion effects and achieve population inversion. The effect of ytterbium doping on net signal gain is less pronounced at higher concentrations. This is explained as follows : as inversion of the erbium population begins to maximize through ytterbium-to-erbium energy transfer, additional donor ytterbium ions have fewer available erbium acceptor ions to transfer energy to.

For evanescent waveguide B, increased mode overlap with the rare-earth-doped substrate is predicted to improve performance across the board (Figure 7.11). In fact, net signal gain is predicted even in the absence of ytterbium (Figure 7.12). Significant gain (>15 dB) is predicted even for erbium levels as high as 2 x 10^{26} ions/m^3, although the optimum concentration remains at ~1 x 10^{26} ions/m^3. Figure 7.13 compares the gain performance of the two devices as a function of input pump power. In stark contrast to the planar waveguides analysed before, the optimum lengths for evanescently-pumped waveguide amplifiers typically exceed 10 cm, even for low pump powers.

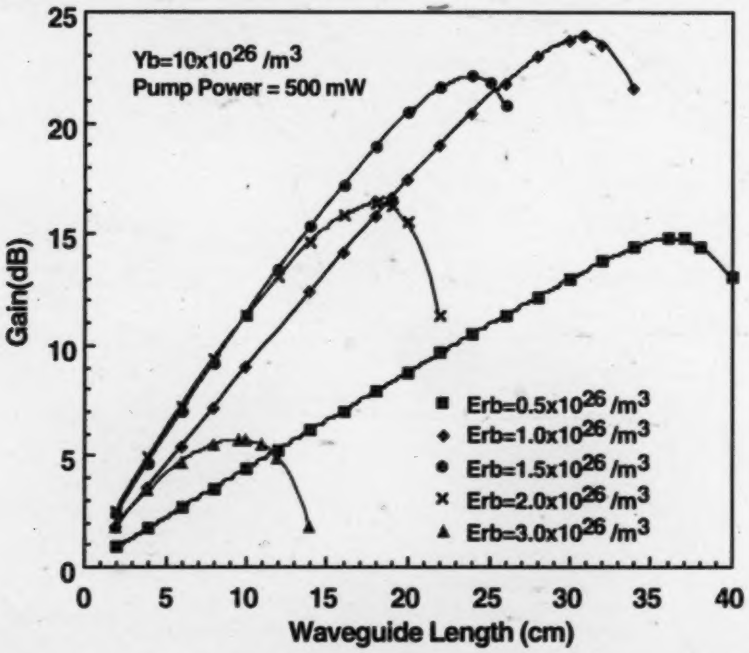

Figure 7.11 Signal Gain vs. Waveguide Length for Evanescent waveguide B : $P_p(0)$ = 500 mW; N_{Yb}= 1x 10^{26} ions/m^3; N_{Erb}=varies.

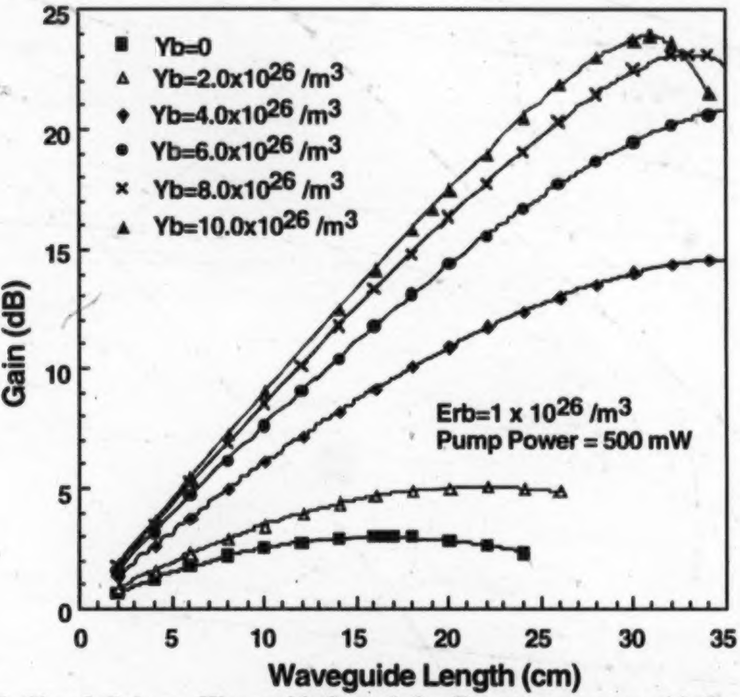

Figure 7.12 Signal Gain vs. Waveguide Length for Evanescent waveguide B : $P_p(0)$ = 500 mW; N_{Erb}= 1x 10^{26} ions/m^3; N_{Yb}=varies.

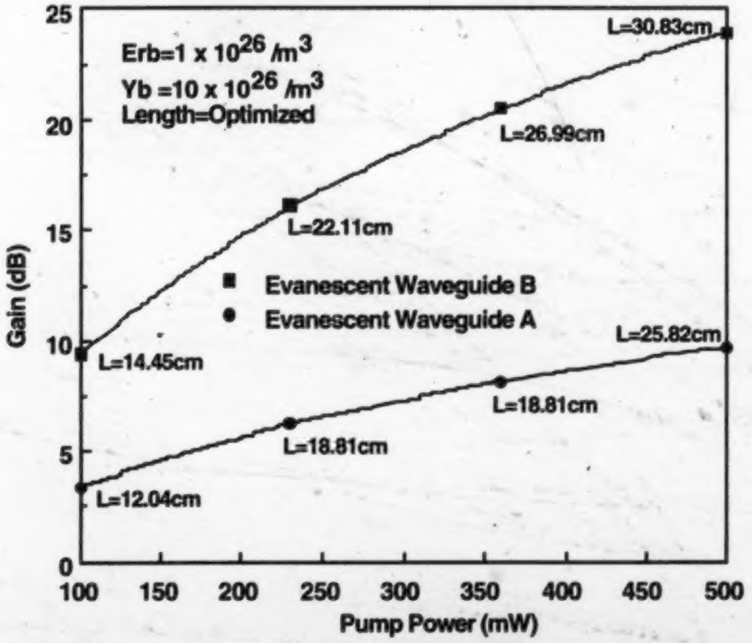

Figure 7.13 Signal Gain vs. Pump Power - Comparison of Evanescent waveguides A & B : $P_p(0)$ = 500 mW; N_{Erb}= 1x 10^{26} ions/m^3; N_{Yb}=10x 10^{26} ions/m^3

Dispensed polymer waveguides on top of glasses with high erbium concentrations have the potential to be used as amplifiers. In composite waveguides of this kind, where evanescent fields are used to excite the erbium ions, weak overlap between pump and signal mode-fields within the active substrate is inevitable. Hence, the total pump power required to attain threshold pump intensity and sustain population inversion will be high. Although the gain coefficients and efficiencies of these evanescently-pumped waveguides will not rival those of planar waveguides with tight mode-field confinement, the ease of fabrication may be an attractive trade-off.

Chapter 8 : Er/Yb-Doped Waveguide Amplifier Fabricated by Dry, Field-Assisted, Silver-Sodium Ion-Exchange

8.1 Introduction

Fabrication of optical waveguides through ion-exchange has been the subject of extensive research in the last few decades [75-80]. In certain glasses containing network modifiers, the refractive index can be altered through selective replacement of monovalent sodium ions (Na^+) with silver ions (Ag^+). Owing to their larger ionic radii, silver ions densify the glass and increase its refractive index. Molten salts ($AgNO_3$) are commonly used as the source for silver ions. Ion-exchange occurs inside a furnace since mobility of ions in glass increases exponentially with temperature. With molten salts, ion-exchange has been shown to occur purely due to thermal diffusion [78]. However, the depth of diffusion is limited to a few micrometers and the maximum index change Δn to ~0.001. This is sufficient to form singlemode waveguides. For multimode waveguides, the process is aided by the application of an electric field across the glass. This increases the flow of ionic current as mobile silver and sodium ions move towards the cathode. Field-assisted ion-exchange results in deeper waveguides with Δn approaching 0.1 [81].

In this chapter, thin films of metallic silver were used as the source for the exchange instead of molten $AgNO_3$. When metallic silver films are used, silver ions can be generated only through an electrochemical oxidation reaction : $Ag(s) \rightarrow Ag^+ + e$. Hence, the application of an electric field is not optional. Field-assisted ion-exchange using silver films has been successfully used to produce low-loss optical waveguides [82-86]. Models which relate the change in refractive index to silver concentration, diffusion coefficients, etc. are widely available in the literature [87,88]. Therefore, the work described in this chapter did not focus on diffusion chemistry. Rather, the impact of various fabrication parameters (temperature, electric-field, volume of diffusant) on optical properties of glass were investigated. Later, ion-exchanged multimode and singlemode channel waveguides were formed on rare-earth-doped glasses and their optical properties were characterized.

8.2 Bulk Ag^+/Na^+ Ion-Exchange in TRL-A

The experimental set-up used for the ion-exchange process is shown in Figure 8.1. In the absence of a vertically-accessible crucible furnace, a hot plate with coarse temperature control had to suffice.

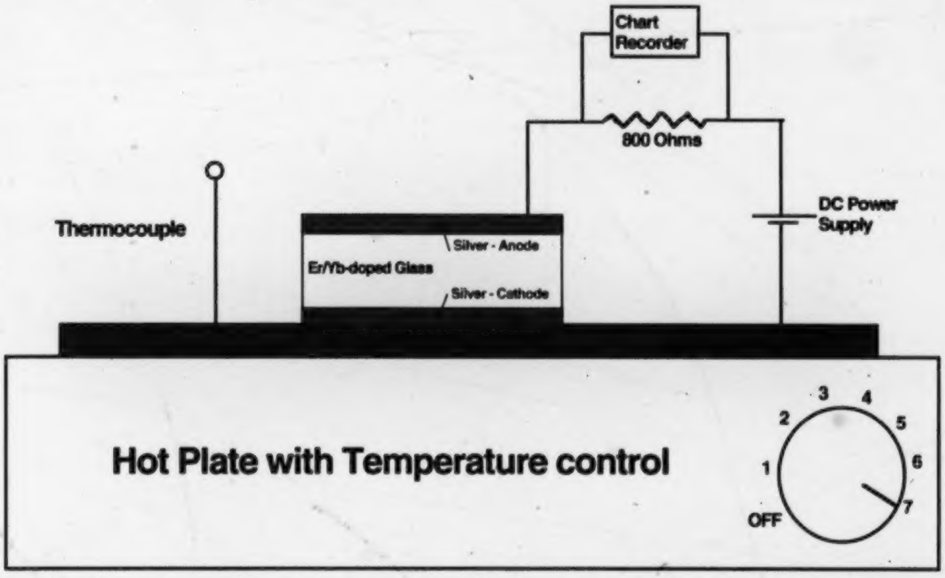
Chart Recorder
800 Ohms
DC Power Supply
Thermocouple
Silver - Anode
Er/Yb-doped Glass
Silver - Cathode
Hot Plate with Temperature control
OFF
1
2
3
4
5
6
7

Figure 8.1 Experimental set-up for field-assisted silver-film ion-exchange into glass.

Silver-sodium ion-exchange was first tested on TRL-A (n=1.61 @ 632 nm), which was originally used as a sputter target (Chapter 4) and known to contain moderate amounts of sodium. A 2 μm-thick silver film was deposited on top and bottom of a 1 cm x 2 cm x 0.7 mm sample of TRL-A. The silver on the top surface (anode) was to be driven into the glass. The silver on the bottom (cathode) was to act as an electrical contact and a sink for sodium ions exiting the glass. The anode silver was not patterned into narrow strips in order to allow ion-exchange across the entire upper surface of the glass. This was expected to facilitate prism-coupler measurements which would help determine the change in refractive index induced by the ion-exchange. The silver-coated glass piece was placed on an aluminum plate atop the ceramic surface of the hot plate. A thermocouple was used to gauge the temperature of the aluminum plate. Metal-tipped DC probes were used to make contact with the anode and cathode. An 800 Ohm resistor was placed between the positive terminal of a DC power supply (maximum 300 Volts) and the anode. The voltage across this resistor was recorded to monitor current flowing through the glass during ion-exchange. The temperature of the hot plate was set to 320°C. With the application of an electric field (143 V/mm), a strong current was observed to flow through the glass. The voltage that was recorded across the resistor over time is shown in Figure 8.2.

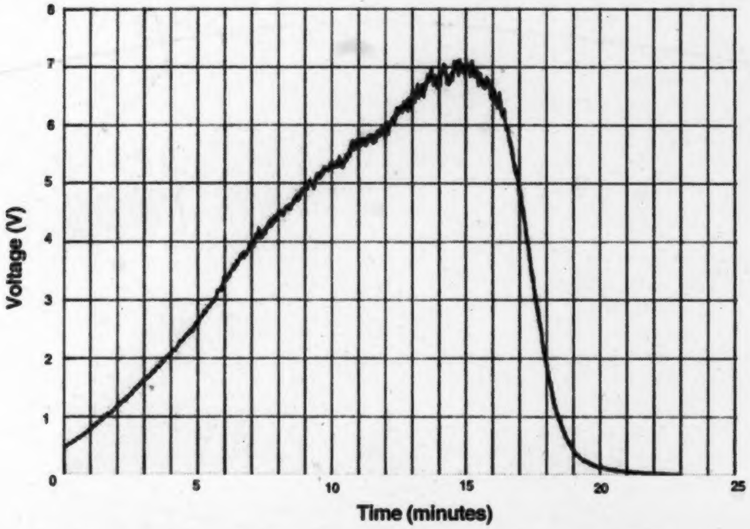

Figure 8.2 Current flow (Voltage/800 Ohms) through TRL-A upon the application of a 143 V/mm electric field at 320°C.

The steady increase in current flow with time indicates that the glass had not reached thermal equilibrium. The sharp drop in current after 15 minutes is due to the depletion of the silver source at the anode. Current flow was negligible (<1 μA) after 23 minutes, and the electric-field was turned off after 25 minutes. The sample was removed immediately from the hot plate to arrest thermal migration and re-distribution of silver ions introduced into the glass. In Figure 8.2, the area under the curve (current-duration product) is a function of the amount of silver available for exchange at the anode. For different electric fields and diffusion temperatures, the form of Figure 8.2 will vary but the area under the curve will remain approximately constant if the thickness of the silver film is constant [81].

After the ion-exchange, numerous bubbles were observed at the cathode, indicating an outflow of sodium ions from the glass. The glass was immersed in pottasium iodide (KI) for several minutes to strip silver residue. The glass was then cut and polished. The cross-section of the glass was inspected inside a Scanning Electron Microscope (SEM). The intensity of back-scattered electrons was photographed (Figure 8.3). Since silver is more reflective than other elements in the glass, the back-scattered image from ion-exchanged regions of the glass is brighter.

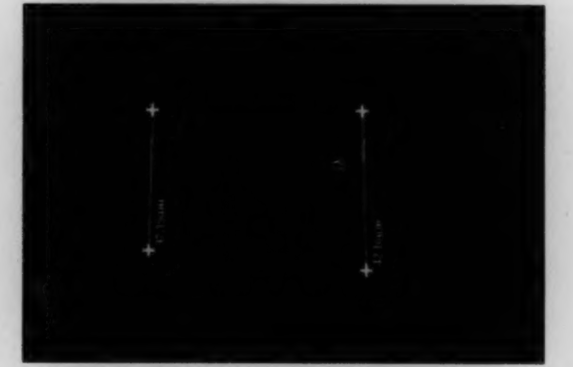

Figure 8.3 SEM photograph showing cross-section of TRL-A after ion-exchange. The diffusion depth can be approximated by the intensity of back-scattered electrons, which is brighter wherever highly reflective silver ions are present.

A prism-coupler, illustrated pictorially in Figure 8.4, was used to couple He-Ne light (λ=632 nm) into the ion-exchanged glass. Total internal reflection at the base of the prism results in the formation of a standing wave whose evanescent field extends across the

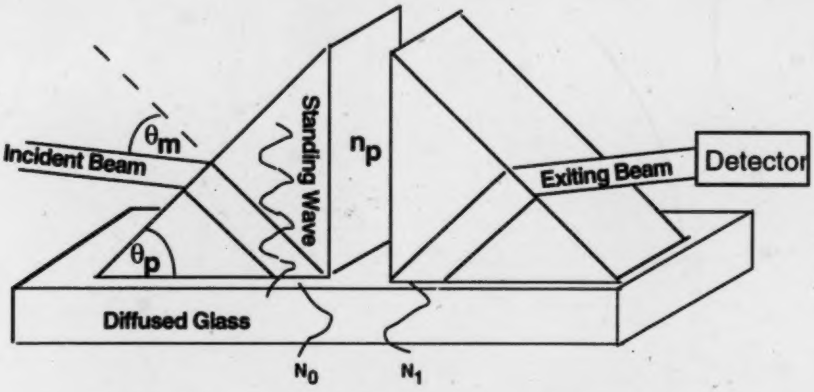

Figure 8.4 Pictorial illustration of prism-coupler.

prism-air gap and into the glass. If the phase velocity (z-component) of the standing wave in the prism matches that of a guided mode in the glass, light is coupled into the glass. By the same principle, light is coupled out of the glass by an identical prism and detected. The effective propagation constant N_m of each mode in the glass is given by :

$$N_m = n_p \operatorname{Sin}\left[\operatorname{Sin}^{-1}\left(\frac{\operatorname{Sin}\theta_m}{n_p}\right) + \theta_p\right]$$

where θ_m is measured by the prism-coupler and and θ_p and n_p are the base angle and refractive index of the prism [81] . By rotating the incident angle θ_m of the He-Ne beam, the prism-coupler was able to excite seven TE modes in the TRL-A sample and identify their propagation constants (Figure 8.5). Given the depth of diffusion apparent in the SEM photograph, the existence of multiple modes was expected. In fact, it is likely that higher order modes were either not excited or successfully resolved by the prism-coupler.

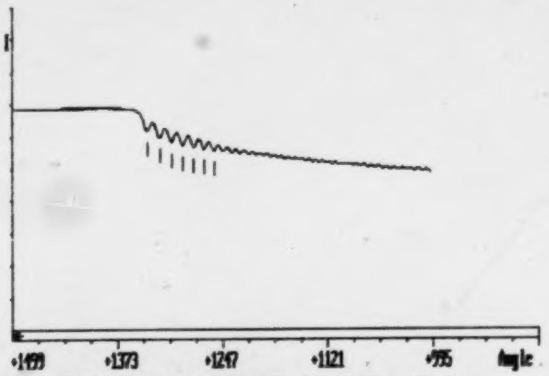

```
Prism= 1042.8            Substrate N= 1.61   Data= 1499 to 999
Wavelength= 632.8        Prism N= 1.9643
  +1338 (1.7095)   +1323 (1.7077)   +1309 (1.7059)   +1296 (1.7043)
  +1283 (1.7027)   +1270 (1.7011)   +1258 (1.6996)
```

Figure 8.5 Prism-coupler analysis of TRL-A after ion-exchange. Seven TE modes with N_m ranging from 1.7095 to 1.6996 were found at λ=633 nm.

Using an inverse WKB algorithm [89,90], the prism-coupler software was able to reconstruct the refractive index profile of the glass as a function of depth based on the propagation constants of the various modes. According to this analysis (Figure 8.6), the refractive index at the surface had increased from 1.61 to 1.71 (a Δn of 0.1) as a result of the silver-sodium ion-exchange.

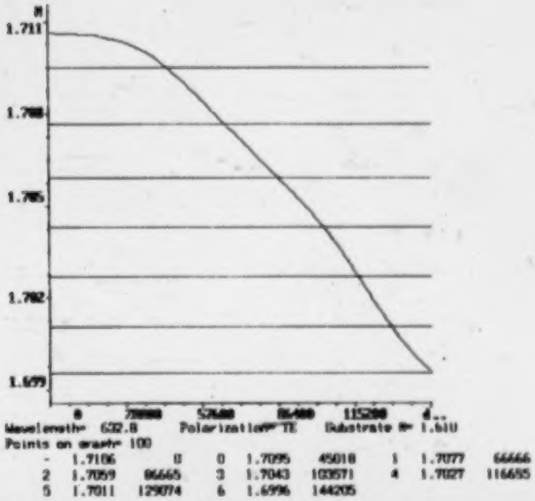

```
Wavelength= 632.8     Polarization= TE    Substrate n= 1.610
Points on graph= 100
   -  1.7106       0     0  1.7095   45018    1  1.7077   66666
   2  1.7059   86665     3  1.7043  103571    4  1.7027  116655
   5  1.7011  129074     6  1.6996  144205
```

Figure 8.6 Refractive index (@λ=633 nm) as a function of depth (in Angstroms) after silver ion-exchange into TRL-A.

Since modal information was incomplete, the refractive index could not be profiled all the way down to the substrate index. Although propagation losses were not measured, the attenuation of He-Ne light over two centimeters of this multimode slab waveguide seemed negligible to the naked eye.

These results were encouraging in terms of producing rare-earth-doped waveguide amplifiers through silver-film ion-exchange. As seen in Chapters 3 and 6, singlemode waveguides offer tight mode-field confinement and high pump/signal overlap. To reduce the number of modes and the dimensions of the slab waveguide, the process parameters had to be altered to reduce Δn and the depth of ion-exchange. Hence, more work was needed to characterize the role of the electric field, diffusion temperture and the thickness of the silver source at the anode. A new sodium silicate glass (IOG-10), doped with erbium and ytterbium, was obtained for this purpose.

8.3 Bulk Ag^+/Na^+ Ion-Exchange in IOG-10

IOG-10 was specified to contain 1 wt% erbium and 3 wt% ytterbium. The low index (n=1.526 @ λ=632 nm) glass was sliced and polished to a thickness of ~ 0.7 mm. The glass was diced into ten 1 cm x 2 cm pieces. As before, 2 μm thick silver films were deposited on the back of all ten pieces to form the cathode. The silver film thickness at the anode was reduced to 0.2 μm (on three pieces) and 0.5 μm (on two pieces).

Electric fields of 7, 28 and 57 V/mm were applied across samples 1, 2 and 3 (0.2 μm silver anode) with the temperature held at 320°C. Table 8.1 summarizes the different ion-exchange conditions and observations. For low electric field strengths, the process duration was found to be quite lengthy. Current flow was recorded as a function of time (as in Figure 8.2) for all three cases. Variations in the current -duration product are most likely due to errors in measurement and/or estimation.

Sample	Electric Field	Duration	Current * Duration
1	7 V/mm	~44 minutes	172 mA*s
2	28 V/mm	~1 minute	198 mA*s
3	57 V/mm	~1 minute	210 mA*s

Table 8.1 Bulk ion-exchange of 0.2 μm silver film into 1 cm x 2 cm x 0.7 mm IOG-10 glass samples. Samples 1, 2 and 3 were diffused under identical temperature settings (320°C) but different electric field strengths.

An SEM photograph (Figure 8.7) of sample 2 suggested that silver ions had penetrated at least 5 μm below the surface. Back-scatter images for samples 1 and 3 were similar.

Figure 8.7 SEM photograph : Cross-section of sample 2 after ion-exhange.

Prism-coupler measurements were more useful in identifying differences between the three diffused samples. Six TE modes were identified in Samples 1 and 3 at λ=633 nm; five modes were identified in Sample 2. Only one mode was identified at λ=1550 nm in all samples. The reconstruction of their refractive index profiles is shown in Figure 8.8.

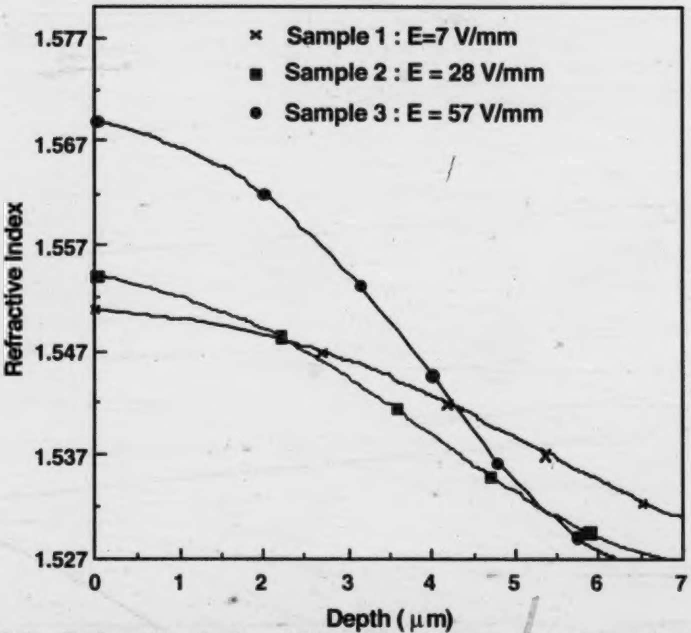

Figure 8.8 Refractive index (@λ=633nm) as a function of depth for Samples 1, 2 and 3. Diffusion Temp = 320°C; Anode = 0.2 μm silver.

From Figure 8.8, it is evident that the maximum change in refractive index (Δn) increases with applied electric field. The Δn for samples 1, 2 and 3 was 0.0232, 0.0264 and 0.0412, respectively. Also noteworthy is the fact that the exchange depth is a stronger function of process duration than electric field strength. The diffusion depths for samples 2 and 3 are comparable (~ 6 μm), coinciding with their short process durations (1 minute). However, silver ions had penetrated deeper into sample 1 (~8 μm) over an extended period of time, in spite of a weak electric field. Index profiles and diffusion depths have implications relating to signal and pump mode shapes, and these will be examined later.

Next, the impact of diffusion temperature and source volume at the anode was investigated. An electric field of 58 V/mm was applied samples 4 and 5, which had 0.5 μm of silver at the anode. The ion-exchange conditions are summarized in Table 8.2. The current-duration product was high due to the increased volume of silver at the anode. SEM analysis suggested silver ions had diffused at least 12 μm into sample 4 (Figure 8.9) and 14 μm into sample 5.

Sample	Tempertaure	Duration	Current * Duration
4	220°C	13 minutes	1120 mA*s
5	320°C	8 minutes	1240 mA*s

Table 8.2 Bulk ion-exchange of 0.5 μm silver film into 1 cm x 2 cm x 0.7 mm IOG-10 glass samples. Two samples diffused under identical electric field strengths (E=58 V/mm) but different temperature settings.

Figure 8.9 SEM photograph showing cross-section of Sample 4 after ion-exchange. The diffusion depth is ~ 12 μm.

The reconstructed refractive index profile (Figure 8.10) shows no significant difference between samples 4 and 5 (Δn ~ 0.0583 and 0.0611, respectively).

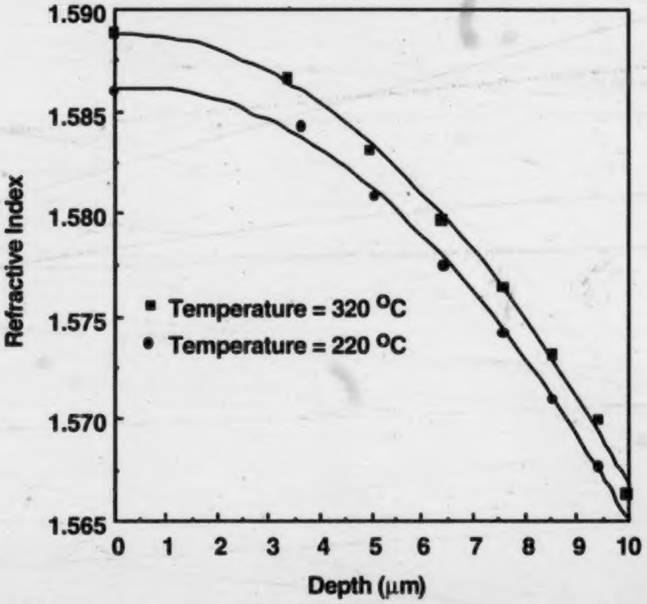

Figure 8.10 Refractive index (@λ=633nm) as a function of depth after ion-exchange. Samples 4 and 5 - E = 58 V/mm; Anode = 0.5 μm silver.

It is reasonable to conclude from Figure 8.10 that, all other factors being equal, temperature plays a relatively minor role in determining the refractive index profile of ion-exchanged waveguides. The same cannot be said of the amount of source material at the anode. This is illustrated by comparing samples 3 and 5, which were diffused under identical temperature and electric field settings but had 0.2 μm and 0.5 μm thick silver films at the anode, respectively. The diffusion depth and Δn for samples 3 and 5 were 6 μm/0.0412 and 16 μm/0.0611, respectively.

Signal and pump modal characteristics corresponding to two different ion-exchange processes were modelled using FWAVE. Samples 2 and 5 were chosen since they represent opposite extremes of Δn and diffusion depth. In diffused waveguides, the refractive index is a continuously varying function of depth (graded-index). However, mode-solver routines like FWAVE analyse stacks of dielectric layers with discrete refractive indices. Therefore, the refractive index profiles for sample 2 and 5 were discretized at 0.25 μm intervals using polynomial expressions derived for the curve fit. The validity of this approximation improves when the size of the interval is much smaller than one wavelength. However, the approximation had to be coarse since the number of dielectric layers analysed by FWAVE was limited to 60. Therefore, the following mode profiles serve only to highlight differences between the two samples, if any.

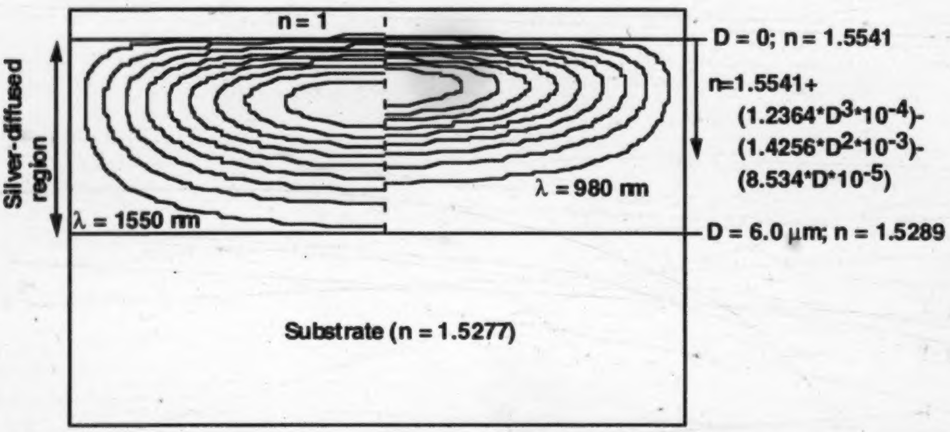

Figure 8.10 Contour plots showing fundamental signal (left) and pump (right) TE mode in graded-index sample 2.

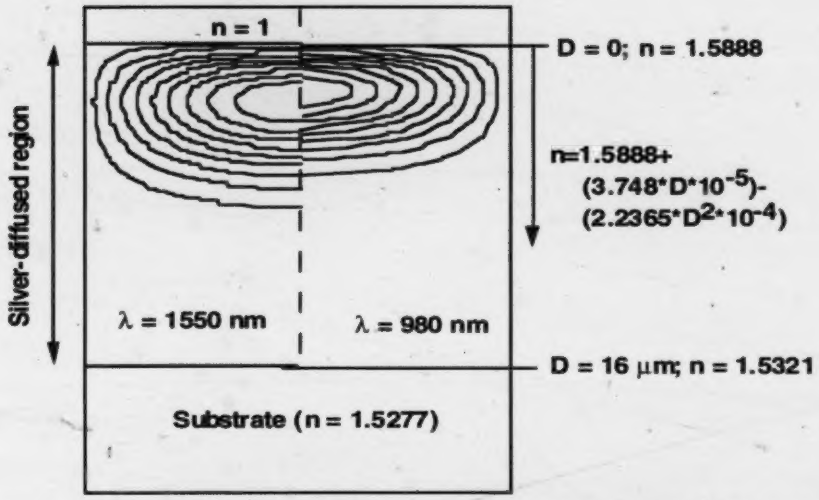

Figure 8.11 Contour plots showing fundamental signal (left) and pump (right) TE mode in graded-index sample 5.

Samples 2 and 5 differ by a factor of two or more in terms of waveguide dimensions, Δn and number of guided modes. However, differences in the fundamental mode structures are not as pronounced. From Figures 8.10 and 8.11, pump/signal mode-field widths (distance between 13.5% contour lines along the axis of diffusion) for samples 2 and 5 are estimated to be ~ 4.2 μm/5.4 μm and 6.0 μm/7.6 μm, respectively. Coupling and propagation losses for sample 5 were expected to be low given its wide mode-field diameter and large physical dimension. Hence, the ion-exchange parameters used for sample 5 served as the template for the first attempt at fabricating multimode channel waveguides.

8.4 Fabrication of Ion-Exchanged Multimode Channel Waveguides

Channel waveguides are formed on glass by confining the ion-exchange to a narrow width. Since a masking layer is required to prevent ion-exchange in other regions of the glass, a metal film (usually chrome) is first deposited uniformly atop the glass. Narrow openings (5-10 μm wide) are exposed on the chrome using photolithography and etching. Silver is then deposited on top of the patterned chrome (Figure 8.12, top). Since chrome acts as a barrier, ion-exchange occurs only in those regions where glass is in direct contact with silver ions (Figure 8.12, middle). After the ion-exchange is completed, the metal films are stripped and the edges of the glass are sawn and polished to form channel waveguides (Figure 8.12, bottom).

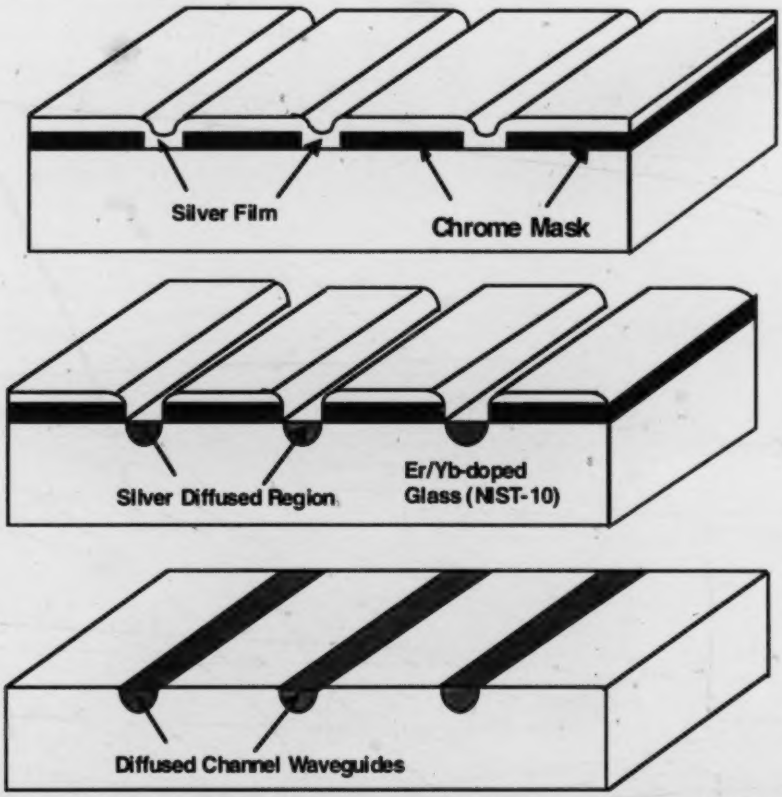

Figure 8.12 - Steps involved in fabricating ion-exchanged channel waveguides. Top : Narrow openings are exposed on the chrome mask and silver is deposited. Middle : Ion-exchange occurs wherever chrome is absent. Bottom : Metal films are stripped, revealing channel waveguides.

The sequence of steps described above was applied to a 1 cm x 2 cm x 0.7 mm sample of IOG-10. A 0.2 µm thick chrome film was found to be an adequate mask. The chrome was patterned to expose several 5 µm wide openings. A 0.5 µm thick silver film was deposited on top of the patterned chrome. Ion-exchange was performed at 320°C in the presence of a 58 V/mm electric field. Current flow through the glass as a function of time is plotted in Figure 8.13. The low current-duration product (~125 mA*s) is due to the fact that ion-exchange was now confined to occur over a smaller surface area.

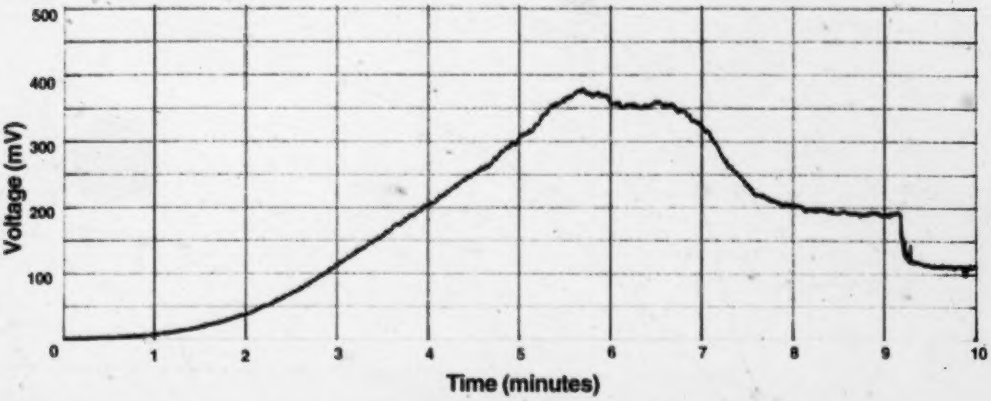

Figure 8.13 Current flow (Voltage/800 Ohms) through IOG-10 during ion-exchange. E = 58 V/mm; Temp = 320°C; Anode = 0.5 μm silver.

The glass was stripped of all metal films and cleaned. In the ion-exchanged regions, the glass had expanded due to stress [81]. Profilometer scans revealed protrusions up to 80 nm above the glass surface (Figure 8.14). This was not noticed in Sections 8.2-8.3 because the ion-exchange had not been laterally confined.

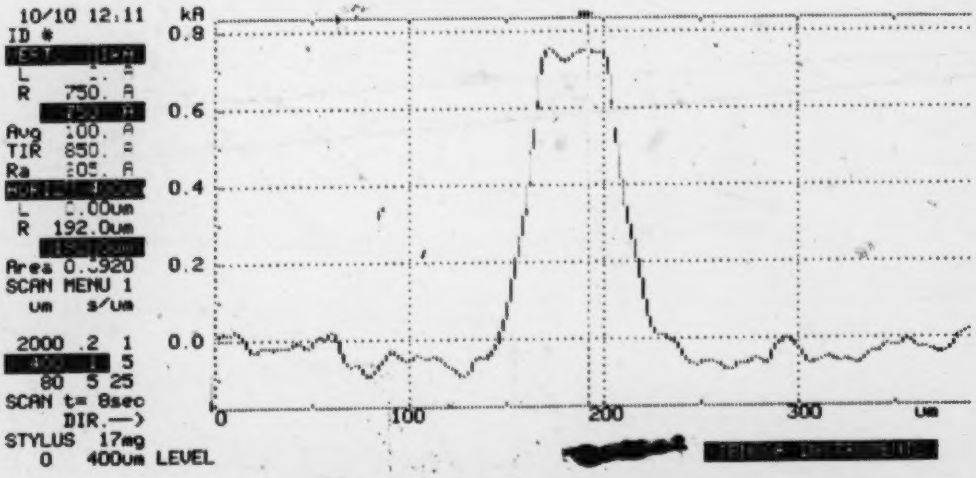

Figure 8.14 Profilometer scan reveals surface expansion in diffused regions of the glass due to stress.

After polishing the end-facets, the glass was inspected using an optical microscope. The ion-exchanged regions were clearly distinguishable due to the high reflectivity of silver (Figure 8.15). The channels were roughly 10 μm deep. However, the lateral width of the channels was conspicuously wider than the openings etched on chrome.

Figure 8.15 Cross-section of ion-exchanged multimode channel waveguide in IOG-10 glass, observed through an optical microscope.

This isotropic diffusion profile is due to the electric-field pattern established in the glass. Figure 8.16 illustrates a typical electric-field pattern in a triplate transmission line with a narrow source and broad sink [81]. According to a model developed to study field-assisted ion-exchange, silver ions tend to diffuse over a width comprising the mask opening plus twice the diffusion depth [91]. The dimensions of the fabricated channel were consistent with this prediction.

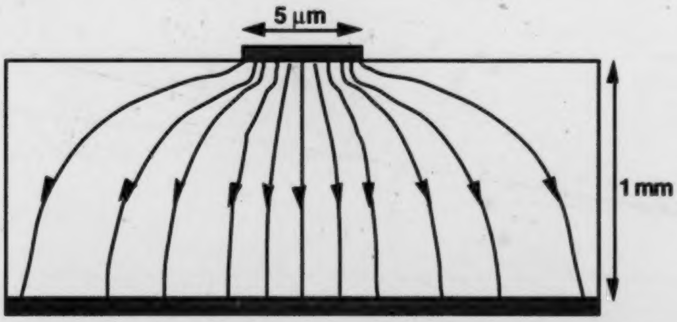

Figure 8.16 Electric-field lines connecting a narrow anode source to a wide cathode sink.

It has been reported that electric field lines can be laterally compressed by spacing the anode mask openings 10 μm apart [92]. Figure 8.17 illustrates the intended effect, which researchers have used to reduce channel waveguide widths by a factor of two [92]. Due to time constraints, a new photomask with the appropriate anode configuration could not be designed and ordered for these experiments. However, this is an essential task for future research in this area.

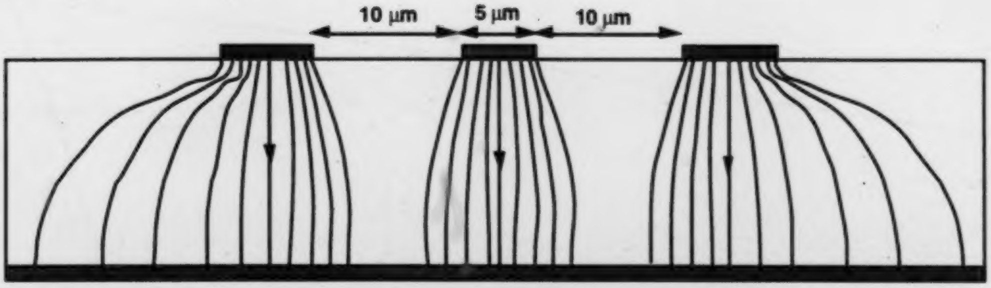

Figure 8.17 Lateral compression of electric field lines due to closely spaced mask openings.

8.5 Optical Properties of Ion-Exchanged Multimode Channel Waveguides

Optical properties of the IOG-10 glass were recorded prior to ion-exchange. From spectrophotometer absorbance data, the peak pump absorption wavelength was estimated to be ~975 nm. The losses at 976.3 nm and 1533 nm due to erbium/ytterbium absorption in the bulk glass were 5.1 dB/cm and 1.52 dB/cm, respectively. Using equipment and techniques described in previous chapters, the ion-exchanged multimode channel waveguide of Figure 8.15 was first tested for its luminescence properties. Spontaneous emission was observed in the 1520-1550 wavelength band when 66 mW of light from a 976.3 nm laser diode was launched into the waveguide. From intensity decay measurements (Figures 8.18), the metastable state lifetime was estimated to be ~ 8 ms.

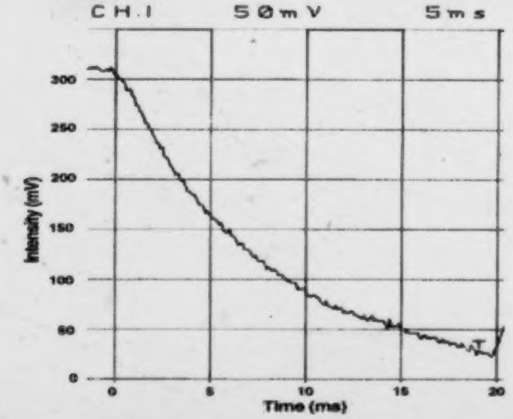

Figure 8.18 Decay of luminescence intensity as a function of time in ion-exchanged channel waveguide. Chopping frequency was 25 Hz.

Quantitatively, the 700 nW of spontaneous emission measured at the waveguide output was the highest recorded during the course of this thesis. The emission spectrum had a single shark peak at 1533 nm.

Using a singlemode fiber WSC, a 1533 nm signal source was launched into an ion-exchanged waveguide which was 1.5 centimeters long. A multimode fiber was used to collect light exiting the waveguide. A net fiber-to-fiber signal throughput loss of 3.84 dB was measured for this device. From bulk absorption data, the erbium-induced loss over 1.5 cm is ~ 2.3 dB, which leaves coupling and propagation losses to account for the remaining 1.5 dB. Signal transparency (or 0 dB gain) was achieved when 66 mW of 976.3 nm pump light was launched into the waveguide along with the signal (Figure 8.19). The 3.75 dB of measured signal enhancement compensates for the net loss in the device within experimental error. The onset of saturation indicates that maximum signal enhancement has been achieved for this device.

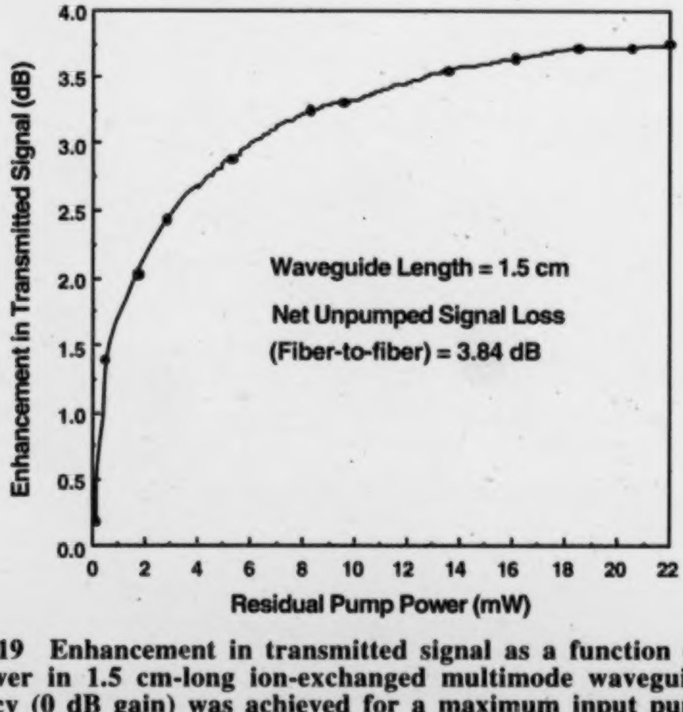

Figure 8.19 Enhancement in transmitted signal as a function of residual pump power in 1.5 cm-long ion-exchanged multimode waveguide. Signal transparency (0 dB gain) was achieved for a maximum input pump power of 66 mW. The input signal power was -13 dBm.

Pump transmission through the device saturates for high input powers (Figure 8.20), confirming the absence of ground-state erbium ions along the entire length of the device.

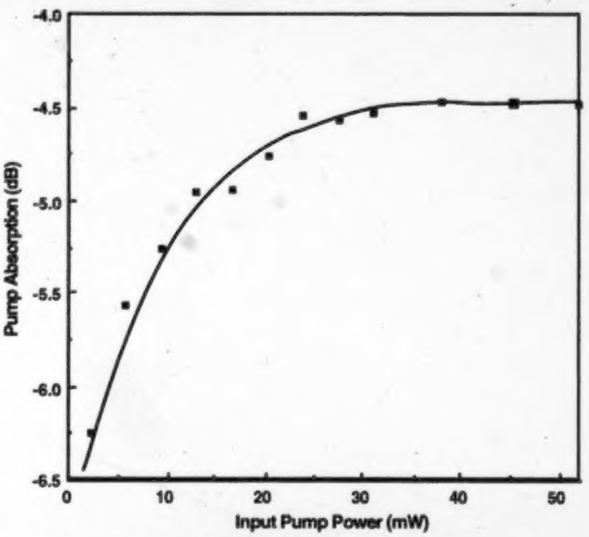

Figure 8.20 Pump loss as a function of input pump power in ion-exchanged multimode waveguide.

Figure 8.21 plots signal enhancement as a function of input signal power with the input pump power constant at 66 mW. For input signal powers greater than -10 dBm, enhancement in transmission was reduced significantly due to signal saturation (Chapter 3).

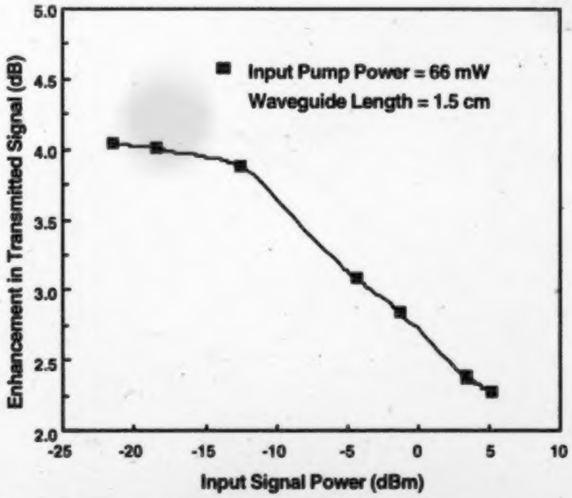

Figure 8.21 Enhancement in transmitted signal as a function of input signal power in ion-exchanged multimode waveguide. The input pump (976.3 nm) power was 66 mW.

The device was pumped with a different laser diode (λ=983.8 nm) in order to investigate the importance of pump wavelength. According to spectrophotometer data, absorption in the bulk glass at 983.8 nm was weaker than at 976.3 nm by a factor of two. A comparison of signal transmission enhancement at these two pump wavelengths (Figure 8.22) confirms that more power would be required at 983.8 nm to achieve an equivalent result.

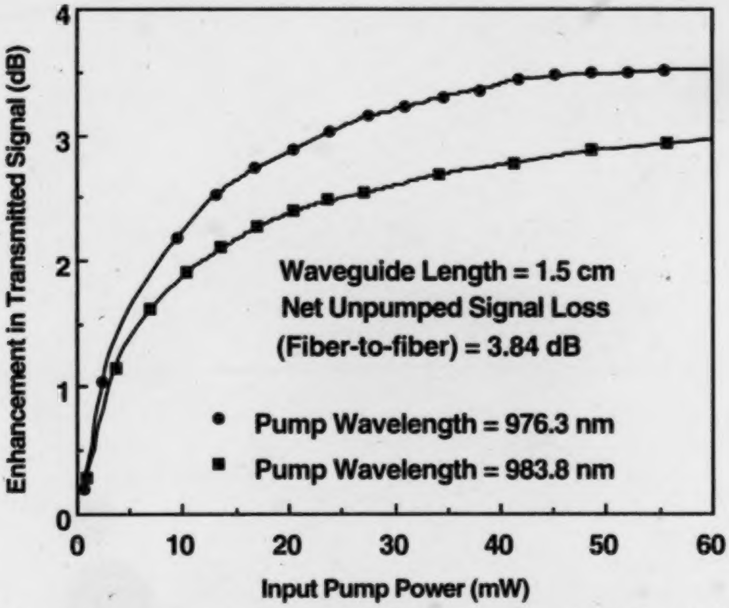

Figure 8.22 Enhancement in transmitted signal as a function of input pump power for two different pump wavelengths.

From Figures 8.19 and 8.22, it was evident that the waveguide was short of optimum length and that longer devices would have to be fabricated. However, a shorter device was expected to provide additional information on waveguide losses. Therefore, after recording the various optical properties described in the previous pages, the 1.5 cm-long device was sawn to produce a shorter waveguide ~ 0.5 cm long. A net fiber-to-fiber signal throughput loss of 1.42 dB was measured in the shorter device. By interpolating between the two distances (and factoring in the 1.52 dB/cm erbium-induced loss at 1533 nm), the coupling and excess propagation loss in this device were estimated to be ~ 0.3 dB and 0.72 dB/cm respectively. Figure 8.23 plots enhancement in transmitted signal as a function of input pump (976.3 nm) power for the 0.5 cm-long waveguide. Signal transparency was achieved with only 25 mW of input pump power but the net gain was negligible.

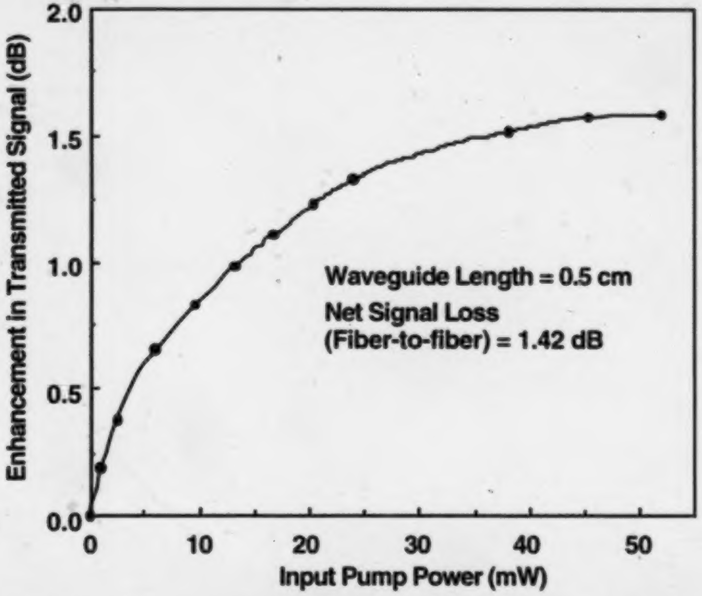

Figure 8.23 Enhancement in transmitted signal as a function of input pump power in 0.5 cm-long ion-exchanged multimode waveguide. Signal transparency (0 dB gain) was achieved for an input pump power of 25 mW. The input signal power was -15 dBm.

The first attempt at fabricating ion-exchanged multimode channel waveguides produced two positive results : 1) signal transparency upon pumping. 2) low coupling loss. On the negative side, the excess propagation loss of 0.72 dB/cm was higher than expected for ion-exchanged multimode waveguides. Also, the unexpectedly large width of the channels prevented tight mode-field confinement. In addition to making the waveguide longer, an attempt was made to address these issues.

8.6 Fabrication and Testing of Ion-Exchanged Singlemode Channel Waveguide Amplifier

In the next iteration in fabrication, the silver film thickness at the anode was reduced to 0.2 μm. This was intended to reduce diffusion depth, width and the silver ion content in the glass (which contributes to excess propagation loss). Further, a reduction in the number of modes at 976 nm and 1533 nm was deemed necessary to improve pump/signal confinement and overlap.

In a graded-index waveguide, the maximum refractive index difference Δn has to be lowered in order to reduce the number of guided modes. The correlation between Δn and electric-field strength was established in Section 8.3. Sample 1 had the lowest Δn (0.0232) among the ion-exchaged slab waveguides discussed in Section 8.3. Prism-coupler measurements at λ=1550 nm suggested that sample 1 was singlemoded at that wavelength (Figure 8.24). Therefore, the ion-exchange parameters used for sample 1 (please refer to Table 8.1) seemed best suited to meet the stated requirements.

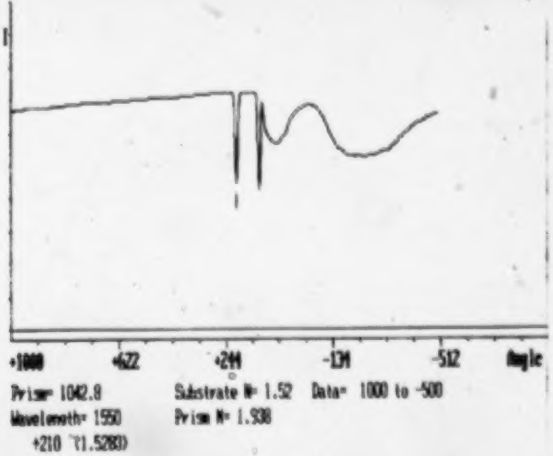

Figure 8.24 Prism-coupler analysis of ion-exchanged slab waveguide sample 1 (from Section 8.3). One TE mode was found at λ=1550 nm.

A 5 cm-long sample of the IOG-10 glass was coated with chrome. During photolithography, 5 μm-wide features could not be patterned due to a defect in the photomask at that location. Therefore, the channels which were formed on the chrome were 9 μm wide. With 0.2 μm of silver at the anode and 2.0 μm of silver at the cathode, ion-exchange was performed at 320°C with an applied electric field of 5 V/mm. The process was stopped after three minutes when current flow ceased. The glass was then sawn and polished to a length of 4.2 cm. The resulting channel waveguide is shown in Figure 8.25.

Figure 8.25 Cross-section of ion-exchanged singlemode channel waveguide.

The diffusion depth (~ 5.5 μm) was consistent with results obtained for the slab waveguide (Figure 8.8). Due to lateral diffusion, the channel was again much wider (~22 μm) than the mask opening. An added wrinkle on this instance was the "saddle-like" cross-sectional profile of the channel. According to the literature, this phenomenon is due to the fact that the electric-field is stronger near potential discontinuities (such as the edges of the metal mask). This phenomenon is said to manifest itself strongly when the mask aperture is larger than the diffusion depth, as was the case here [91].

Net throughput signal (λ=1533 nm) loss of ~ 7.1 dB was measured in this device. Signal transparency was achieved with 48 mW of input pump power (Figure 8.26). A net signal gain of ~ 0.6 dB was observed with 63 mW of pump power.

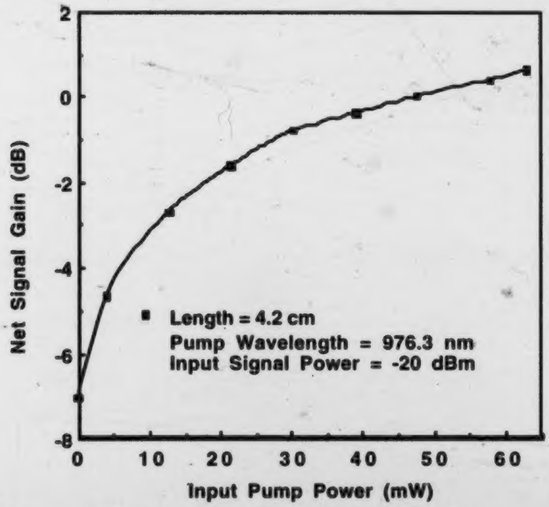

Figure 8.26 Net signal gain as a function of input pump power in a 4.2 cm-long ion-exchanged singlemode waveguide. Signal transparency (0 dB gain) occurs for an input pump power of ~48 mW. The pump was a 976.3 nm laser diode introduced into one end of the waveguide.

Since the gain in Figure 8.26 appeared to be increasing as a function of input pump power, a counter-propagating pump source (λ = 983.8 nm) was introduced at the output of the waveguide. Some changes were required in the experimental set-up to accomodate the dual-pump arrangement. Instead of the multimode pick-up fiber, a fiber WSC was used at the waveguide output to simultaneously launch the counter-propagating pump source into the waveguide and extract the signal. The 1533 nm signal exiting the waveguide, amplified spontaneous emission and a small fraction of co-propagating pump all appear at the signal port of the second WSC. In order to distinguish the signal from ASE and scattered pump, the 1533 nm signal was modulated and observed on an oscilloscope. Signal enhancement upon pumping was measured by the change in peak-to-peak voltage of the modulated signal. Signal enhancement of 10.6 dB, corresponding to a net signal gain of ~ 3.5 dB, was observed with 120 mW of pump power launched into the waveguide (Figure 8.27).

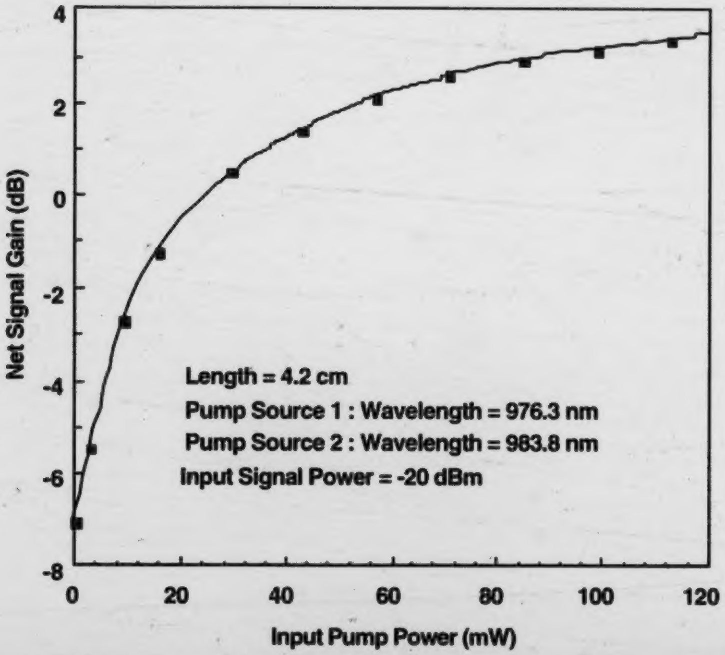

Figure 8.27 Net signal gain as a function of pump power in a dual-pumped, 4.2 cm-long ion-exchanged singlemode waveguide. Signal transparency occurs for a combined input pump power of ~30 mW. The co-propagating pump was a 976.3 nm laser diode and the counter-propagating pump was a 983.8 nm laser diode.

The bi-directional pumping scheme is more efficient in avoiding signal reabsorption at one end of the waveguide. Therefore, the threshold pump power required for signal transparency was reduced to ~ 30 mW (15 mW from each end). To put this result in perspective, it is included in Table 8.3, along with the results reported by all the major research groups investigating erbium-doped planar waveguide amplifiers to date.

PROCESS	Er_2O_3	Amplifier Length (cm) x Height (μm) x Width (μm)	Gain (dB)	Pump Power(mW)
FLAME HYDROLYSIS	0.45 wt%	48 x 7 x 8	27	284
MOLTEN SILVER ION-EXCHANGE	3.0 wt%	4.5 x 5.0 x 6.5	16.5	100
SPUTTERING	2.8 wt%	4.5 x 1.3 x 5	15	280
POTTASIUM ION-EXCHANGE	1.65 wt%	0.6 x NA x NA	7.3	50
THALLIUM ION-EXCHANGE	3.0 wt%	3.8 x 6 x 5	7.0	100
PECVD	0.48 wt%	7.5 x 8 x 11	5	420
SPUTTERING	> 2 wt%	1 x 1 x 5	4	60
SILVER-FILM ION-EXCHANGE	1 wt%	4.2 x 5.5 x 22	3.5	120
ER-INDIFFUSION INTO $Ti:LINBO_3$	NA	1.7 x NA x 8	2.7	80
ION-IMPLANTATION	2.7×10^{20} ions/cm^3	4 x NA x NA	2.3	10

NA = Information was Not Available in the published manuscript.

Table 8.3 - The amplifier reported in this thesis is listed along with the best reported results from several research groups involved in erbium-doped planar waveguide amplifiers (as of March 1998).

The pumping efficiency (0.03 dB/mW) reported in this chapter can be improved through better lateral light confinement, which would reduce the threshold pump power required to sustain population inversion. This can be achieved either by compressing the electric field lines during diffusion or by a passive index-loading rib on the surface. Increasing the erbium content in the glass would then improve the gain coefficient over the same distance.

Conclusions

This thesis has explored modeling and fabrication issues related to erbium/ytterbium-doped waveguide amplifiers for application in integrated optics. According to simulations, high erbium dopant levels (2-3 wt%) are required to achieve amplification over distances of less than 10 cm. For such high concentrations, interaction between adjacent erbium ions reduces population inversion and thus, stimulated emission. Ytterbium co-doping was shown to mitigate this effect by strongly absorbing pump photons and populating the metastable state of erbium through energy transfer. Simulation results also suggest that rare-earth-doped optical waveguides with narrow cores offer the best performance due to strong light confinement within the active layer. Optical waveguide formation on rare-earth-doped thin-films and bulk glasses were investigated.

The complex chemistry of rare-earth-doped thin-film glasses makes them intractable to conventional micromachining processes. Strip-loaded waveguides, formed by etching ribs on a passive glass layer deposited on top of a planar rare-earth-doped film, offer an attractive alternative. In this configuration, the stoichiometry of the active film can be independently optimized to host large amounts of rare-earth-dopants while the passive layer can be chosen independently to suit micromachining requirements.

Silver-film ion-exchange in rare-earth-doped glass is a simple and effective method of fabricating low-loss, singlemode amplifiers. Net signal amplification of 3.5 dB was achieved over a short length of erbium/ytterbium-doped waveguide using 120 mW of pump power. There have been fewer than a dozen successful demonstrations of such planar erbium-doped waveguide amplifiers this decade.

To the best of my knowledge, the work described in Chapter 5 represents the first reported instance of transforming planar rectangular glass films into hollow, circular microchannels. Smooth hollow channels 1cm in length and 10μm in diameter were formed as a result of selective inflation of molten glass. This concept of "controlled glass-blowing" can potentially be put to good use in microfluidic applications.

References

[1] B. Saleh and M. Teich, Photonics, J. Wiley & Sons, 1991.

[2] D. Marcuse, Theory of Dielectric Optical Waveguides, Academic Press, 1974.

[3] A. Yariv, Quantum Electronics, J. Wiley & Sons, 1988.

[4] E. C. Jordan and K. G. Balman, Electromagnetic Waves and Radiating Systems, Prentice-Hall Inc., 1968.

[5] C. R. Pollock, Fundamentals of Optoelectronics, Irwin, 1995.

[6] C.L. Chen, Elements of Optoelectronics and Fiber Optics, Irwin, 1996.

[7] J. Wilson and J.F.B. Hawkes, Optoelectronics : An Introduction, Prentice-Hall Inc., 1996.

[8] J. Gowar, Optical Communication Systems, Prentice-Hall Inc., 1996.

[9] J. M. Senior, Optical Fiber Communications, Prentice-Hall Inc., 1996.

[10] M. Born and E. Wolf, Principles of Optics, Pergamon Press, 1980.

[11] D. Marcuse, "Solution of the Vector Wave Equation for General Dielectric Waveguides by the Galerkin Method", IEEE Journal of Quantum Electronics, Vol. 28, 1992, pp. 459-465.

[12] B. A. Rahman and J. Davies, "Finite-element analysis of optical and microwave waveguide problems", IEEE Transactions on Microwave Theory and techniques, Vol. MIT_32, 1984, pp. 20-28.

[13] R. L. Gallawa, I. C. Goyal, Y. Tu, and A. K. Ghatak, "Optical Waveguide Modes: An Approximate Solution Using Galerkin's Method with Hermite-Gauss Basis Functions", IEEE Journal of Quantum Electronics, Vol. 27, No. 3, March 1991, pp. 518-522.

[14] T. Rasmussen, J. H. Povlsen, A. Bjarklev, O. Lumholt, B. Pedersen, and K. Rottwitt, "Detailed Comparison of Two Approximate Methods for the Solution of the Scalar Wave Equation for a Rectangular Optical Waveguide", Journal of Lightwave Technology, Vol. 11, No. 3, March 1993, pp. 429-433.

[15]. C. Yeh, K. Ha, S. B. Dong, and W. P. Brown, "Single-mode Optical Waveguides", Applied Optics, Vol. 18, No. 10, May 1979, pp. 1490-1504.

[16] M. R. S. Taylor, FWAVE III : A program for solving the fields of electromagnetic waveguides, Version 1.3.3 β, 1989-1993.

[17] R. S. Boikees and E. Edelson, Chemical Principles, Harper and Row, 1985.

[18] E. Desurvire, Erbium-Doped Fiber Amplifiers, J. Wiley & Sons, 1994.

[19] W. J. Miniscalco, "Erbium-doped glasses for fiber amplifiers at 1500 nm", Journal of Lightwave Technology, Vol. 9, No. 2, pp. 234-250, 1991.

[20] M . Federighi and F. Di Pasquale, "The Effect of Pair-Induced Energy Transfer on the Performance of Silica Waveguide Amplifiers with High Er^{3+}/Yb^{3+} Concentrations", IEEE Photonics Technology Letters, Vol. 7, No. 3, March 1995, pp. 303-305.

[21] P. Blixt, J. Nilsson, T. Carlnas, and B. Jaskorzynska, "Concentration-dependent Upconversion in Er^{3+}-doped Fiber Amplifiers : Experiments and Modeling", IEEE Photonics Technology Letters, Vol. 3, No. 11, Nov. 1991, pp. 996-998.

[22] E. Delevaque, T. Georges, M. Monerie, P. Lamouler, and J.-F. Bayon, "Modeling of Pair-Induced Quenching in Erbium-Doped Silicate Fibers", IEEE Photonics Technology Letters, Vol. 5, No. 1, Jan. 1993, pp. 73-75.

[23] M. Shimizu, M. Yamada, M. Horiguchi, and E. Sugita, "Concentration Effect on Optical Amplification Characteristics of Er-Doped Silica Single-Mode Fibers", IEEE Photonics Technology Letters, Vol. 2, No. 1, Jan. 1990, pp. 43-45.

[24] G. N. van den Hoven, E. Snoeks, A. Polman, C. van Dam, J. W. M.van Uffelen, and M. K. Smit, "Upconversion in Er-implanted Al_2O_3 Waveguides", Journal of Applied Physics, 79 (3), Feb. 1996, pp. 1256-1266.

[25] F. Di Pasquale and M. Federighi, "Modeling of Uniform and Pair-Induced Upconversion Mechanisms in High-Concentration Erbium-Doped Silica Waveguides", Journal of Lightwave Technology, Vol. 13, No. 9, Sept. 1995, pp. 1858-1864.

[26] F. Di Pasquale and M. Federighi, "Improved Gain Characteristics in High-Concentration Er^{3+}/Yb^{3+} Codoped Glass Waveguide Amplifiers", IEEE Journal of Quantum Electronics, Vol. 30, No. 9, Sept. 1994, pp. 2127-2131.

[27] F. Di Pasquale, M. Zoboli, M. Federighi, and I. Masarek, "Finite-Element Modeling of Silica Waveguide Amplifiers with High Erbium Conecntration", Vol. 30, No. 5, May 1994, pp. 1277-1282.

[28] K. Winick and G. L. Vossler, "Erbium:ytterbium Planar Waveguide Laser in Ion-Exchanged Glass", Proceedings of SPIE : Rare-Earth-Doped Devices, San Jose, Feb. 10-11 1997, pp. 121-134.

[29] F. Di Pasquale and M. Zoboli, "Analysis of Erbium-Doped Waveguide Amplifiers by a Full-Vectorial Finite-Element Method", Journal of Lightwave Technology, Vol. 11, No. 10, Oct. 1993, pp. 1565-1573.

[30] J. E. Freeman, "Theory, Design, and Characterization of Erbium-Doped Fiber Amplifiers", M.Sc Thesis, University of Alberta, 1991.

[31] T. Kitagawa, K. Hattori, K. Shuto, M. Yasu, M. Kobayashi, and M. Horiguchi, "Amplification in Erbium-Doped Silica-Based Planar Lightwave Circuits", Electronics Letters, Vol. 28, No. 19, pp. 1818-1819, 1992.

[32] P. Camy, J.E. Roman, F. W. Willems, M. Hempstead, J. C. van der Plaats, C. Prel, A. Beguin, A.M.J. Koonen, J. S. Wilkinson, and C. Lerminiaux, "Ion-exchanged planar lossless splitter at 1.5 μm", Electronics Letters, Vol. 32, No. 4, Feb. 1996, pp. 32-34.

[33] P. Fournier, P. Meshkinfam, M. A. Fardad, M. P. Andrews and S. I. Najafi, "Potassium Ion-exchanged Er-Yb doped phosphate glass amplifier", Electronics Letters, Vol. 33, No. 4, Feb. 1997, pp. 293-295.

[34] D. Barbier, J. M. Delevaux, A. Kevorkian, P. Gastaldo, and J.M. Jouanno, "Yb/Er Integrated Optic amplifiers on phosphate glass in single and double pass configurations", OFC' 95, San Diego CA, 1995, post-deadline paper PD3-1.

[35] D. L. Veasey, J. M. Gary, and J. Amin, "Rigorous Modeling of Er and Er/Yb-doped Waveguide Lasers", Proceedings of SPIE : Rare-Earth-Doped Devices, San Jose, Feb. 10-11 1997, pp. 109-120.

[36] B. Chapman, Glow Discharge Processes, J. Wiley and Sons, 1980, Chapter 6.

[37] D. L. Smith, Thin-Film Deposition : Principles and Practice, McGraw-Hill, 1995.

[38] S. V. Nguyen, "Plasma assisted chemical vapor deposited thin films for microelectronic applications", Journal of Vacuum Science Technology, B 4 (5), Sep/Oct 1986, pp. 1159-1167.

[39] M. Brett, Thin-Film Deposition, Graduate Course EE 642, Dept. of Electrical Engineering, University of Alberta, Edmonton, Alberta, 1993.

[40] D. S. Walker, W. M. Reichert and C. J. Berry, "Corning 7059, Silicon Oxynitride, and Silicon Dioxide Thin-Film Integrated Optical Waveguides:In Search of Low Loss, Nonfluorescent, Reusable Glass Waveguides", Applied Spectroscopy, Vol. 46, No. 9, 1992, pp. 1437-1441.

[41] K. Shuto, K. Hattori, T. Kitagawa, Y. Ohmori, and M. Horiguchi, "Erbium-Doped Phosphosilicate Amplifier Fabricated by PECVD", Electronics Letters, Vol. 29, No. 2, Jan. 1993, pp. 139-141.

[42] A. V. Chelnokov, J.-M. Lourtioz, Ph. Boucaud, H. Bernas, J. Chaumont, and T. Plowman, "Deep high-dose erbium implantation of low-loss silicon oxynitride waveguides", Electronics Letters, 1994.

[43] W.-T. Tsang, C.-C Tseng, and S. Wang, "Optical Waveguides Fabricated by Preferential Etching", Applied Optics, Vol. 14, No. 5, May 1975, pp. 1200-1206.

[44] E. Bassous, "Fabrication of Novel Three-Dimensional Microstructures by the Anisotropc Etching of (100) and (110) Silicon", IEEE Transactions on Electron Devices, Vol. ED-25, No. 10, Oct. 1978.

[45] V. A. Yunkin, D. Fischer, and E. Voges, "Highly anisotropic selective reactive ion etching of deep trenches in silicon", Microelectronic Engineering, 23, 1994, pp. 373-376.

[46] C. Dominguez and J. Munoz, "CHF_3 -reactive ion etching for waveguides", Sensors and Actuators A, 37-38, 1993, pp. 779-783.

[47] E. Cabruja and M Screiner, "Deep trenches in silicon using photoresist as a mask", Sensors and Actuators A, 37-38, 1993, pp. 766-771.

[48] J. R. Lothian, F. Ren and S. J. Pearton, "Mask erosion during dry etching of deep features in III-V semiconductor structures", Semiconductor Science Technology, 7, 1992, pp. 1199-1209.

[49] J. Shmulovich, A. Wong, Y.H. Wong, P. C. Becker, A.J. Bruce and R. Adar, "Er^{3+} Glass Waveguide Amplifier at 1.5 µm on Silicon", Electronics Letters, Vol. 28, No. 13, June 1992, pp. 1181-82.

[50] R. N. Ghosh, J. Schmulovich, C.F. Kane, M.R.X. de Barros, G. Nykolak, A. J. Bruce, and P.C. Becker, "8-mW Threshold Er^{3+}-Doped Planar Waveguide Amplifier", IEEE Photonics Technology Letters, Vol. 8, No. 4, April 1996, pp. 518-520.

[51] Schott Glass Technologies Inc., 400 York Ave., Duryea, PA 18642-2036, USA.

[52] C. H. Henry, R. F. Kazarinov, H. J. Lee, K. J. Orlowsky, and L.E. Katz, "Low loss Si_3n_4-SiO_2 Optical Waveguides on Si", Applied Optics, Vol. 26, No. 13, July 1987, pp. 2621-2624.

[53] S. Dutta and H.E. Jackson, "Extremely Los-loss Glass Thin-film Optical Waveguides Utilizing Surface Coating and Laser Annealing", Journal of Applied Physics, 52(6), June 1981, pp. 3873-3875.

[54] N. Nourshargh, E.M. Starr, N.I. Fox, and S. G. Jones, "Simple Technique for Measuring Attenuation of Integrated Optical Waveguides", Electronics Letters, 1985.

[55] A. Tz. Andreev, K.P.Panajotov, B.S.Zafirova, and J.B. Kopriarova, "Single-mode fiber to planar waveguide coupling", SPIE Vol. 1973/77.

[56] Norland Products inc., Joyce Kilmer Ave., New Brunswick, NJ 08902, USA.

[57] Dr. M. Brett, Dept. of Electrical Engineering, University of Alberta, Edmonton, Canada. Private communiation.

[58] U.S. Patent No. 4693739

[59] U.S. Patent No. 3365315

[60] J.N. McMullin, R. Narendra, C.R. James, "Hollow metallic waveguides in silicon V-grooves", Photonics Technology Letters, Vol. 5, No. 9, 1080-1082, September 1993.

[61] J.A. Harrington, "Selected papers on infrared fibre optics", SPIE Optical Engineering Press, Bellingham, WA, 1990, MS-9.

[62] M. C. Tracy, R. S. Greenaway, A. Das, P. H. Kays, A. J. Barnes, "A Silicon Micromachined Device for Use in Blood Deformbility Studies", IEEE Trans. Biomedical Eng., vol. 42, no. 8, 751-760, 1995.

[63] W. Kaplan, H. Elderstig and C. Vieider, "A novel fabrication method of capillary tubes on quartz for chemical analysis applications", Proc. MEMS '94, 63-68, 1994

[64] T. Nguyen, R. Kiehnscherf, "Low-cost silicon sensors for mass flow measurement of liquids and gases", Sensors and Actuators A, vol. 49, 17-20, 1995.

[65] G. Stemme, "Micro Fluid Sensors and Actuators", IEEE Proc. 6th Int'l Symposium on Micro Machine and Human Science, 45-52, 1995.

[66] H. Weisberg, H. Bau, J. N. Zemel, "Analysis of microchannels for integrated cooling", Int'l. J. Heat and Mass Transfer, vol. 35, no. 10, 2465-2474, 1992.

[67] T. L. Hoopman, "Microchanneled structures". In Microstructures, Sensors and Actuators, (Edited by D. Cho, R. Warrington, C. Blechinger, A. Pisano, W. Trimmer and L. Trefethan), DSC-Vol. 19, 171-174, ASME, New York (1990).

[68] R. T. Chen, H. Lu, D. Robinson, Z. Sun. T. Jannson, D. V. Plant, and H. R. Fetterman, "60 GHz board-to-board optical interconnection using polymer optical busses in conjunction with microprism couplers", Applied Physics Letters, vol. 60, no. 5, pp. 536-538, 1992.

[69] R. T. Chen, "Graded index linear and curved polymer channel waveguide arrays for massively parallel optical interconnects", Applied Physics Letters, vol. 61, no. 19, pp. 2278-2280, 1992.

[70] D. Gerold and R. T. Chen, "Vacuum-tuned graded-index polymer waveguides on silicon substrates", Applied Optics, vol. 35, no. 3, pp. 400-403, 1996.

[71] D. W. Boertjes, J. N. McMullin and B. P. Keyworth, "Graded-Effective Index Planar Polymer Waveguides", accepted for publication by IEEE Journal of Lightwave Technology.

[72] Kigre Inc., 100 Marshall Road, Hilton Head, S. C., 29926.

[73] B. P. Keyworth, J. N. McMullin, R. Narendra, and R. I. MacDonald, "Computer-controlled pressure-dispensed multimode polymer waveguides", IEEE Transactions CPMT

- Part B, vol. 18, no. 3, pp. 572-577, 1995.

[74] B. P. Keyworth, D. J. Corazza, J. N. McMullin and L. Mabbott, "Single-step fabrication of refractive microlens arrays", accepted for publication by Applied Optics.

[75] G. H. Chartier and P. Jaussaud, "Optical Waveguides Fabricated by Electric-Field Controlled Ion Exchange in Glass", Electronics Letters, Vol. 14, 1978, pp. 132-134.

[76] T. Findakly, "Glass Waveguides by Ion Exchange : A Review", Optical Engineering, March/April 1985, Vol. 24, No. 2, pp. 244-250.

[77] R. V. Ramaswamy and R. Srivastava, "Ion-Exchanged Glass Waveguides : A Review", Journal of Lightwave Technology, Vol. 6, No. 6, June 1988, pp. 984-1001.

[78] T.G. Giallorenzi, E.J. West, R. Kirk, R. Ginther, and R.A. Andrews, "Optical Wavegudies Formed by Thermal Migration of Ions in Glass", Applied Optics, Vol. 12, No. 6, June 1973, pp. 1240-1245.

[79] J. Viljanen and M. Leppihalme, "Fabrication of Optical Strip Waveguides with Nearly Circular Cross-Section by Silver Ion Migration Technique", Journal of Applied Physics, 51 (7), July 1980, pp. 3562-3565.

[80] K. Forrest, S.J. Pagano, and W. Viehmann, "Channel Waveguides in Glass via Silver-Sodium Field-Assisted Ion Exchange", Journal of Lightwave Technology, Vol. LT-4, No. 2, February 1986, pp. 140-150.

[81] S. I. Najafi, Introduction to Glass Integrated Optics, Artech House Inc., 1992.

[82] Dr. R. I. MacDonald, private communication.

[83] S. Honkanen and A. Tervonen, "Experimental Analysis of Ag^+-Na^+ exchange in glass with Ag film sources for planar optical waveguide fabrication", Journal of Applied Physics, 63 (3), Febraury 1988, pp. 634-638.

[84] H. Zhenguang, R. Srivastava and R. V. Ramaswamy, "Single-mode buried channel waveguide by single-step electromigration technique using silver film", Applied Physics Letters, 53 (18), Oct. 1988, pp. 1681-1683.

[85] S. Tammela, H. Pohjonen, S. Honkanen, and A. Tervonen, "Fabrication of large multimode glass waveguides by dry silver ion exchange in vacuum", SPE Vol. 1583, Integrated Optical Circuits, 1991, pp. 37-42.

[86] S. Honkanen, P. Poyhonen, M. Tahkokorpi, A. Tervonen, and S. Tammela, "Single-mode Glass Waveguides and Components by One-Step Dry Ion Exchange Technique", EFOC/LAN 90, Munich, Germany, June 27-29, 1990, pp. 135-137.

[87] R. V. Ramaswamy and S. I. Najafi, "Planar, Buried, Ion-Exchanged Glass Waveguides: Diffusion Characteristics", IEEE Journal of Quantum Electronics, Vol. QE-

22, No. 6, June 1986, pp. 883-891.

[88] S. I. Najafi, P.G. Suchoski, and R.V. Ramaswamy, "Silver Film-Diffused Glass Waveguides : Diffusion Process and Optical Properties", IEEE Journal of Quantum Electronics, Vol. QE-22, No. 12, December 1986, pp. 2213-2218.

[89] K. S Chiang, "Construction of Refractive-Index Profiles of Planar Dielectric Waveguides from the Distribution of Effective Indexes", Journal of Lightwave Technology, Vol. LT-3, No. 2, April 1985, pp. 385-391.

[90] J. M. White and P.F. Heidrich, "Optical Waveguide Refractive Index Profiles Determined from Measurement of Mode Indices : A Simple Analysis", Applied Optics, Vol. 15, No. 1, Jan. 1976, pp. 151-155.

[91] J. Albert and J.W.Y. Lit, "Full Modeling of Field-Assisted Ion Exchange for Graded Index Buried Channel Optical Waveguides", Applied Optics, Vol. 29, No. 18, June 1990, pp. 2798-2804.

[92] S. Honkanen, A. Tervonen, H. von Bagh, A. Salin, and M. Leppihalme, "Fabrication of Ion-Exchanged Channel Waveguides Directly Into Integrated Circuit Mask Plates", Applied Physics Letters, 51(5), August 1987, pp. 296-298.

[93] B. G. Pantchev, "One-Step Field-Assisted Ion Exchange For Fabrication of Buried Multimode Strip Waveguides", Electronics Letters, vol. 23, 1987, pp. 1188-1190.

Appendix A : Newton-Raphson Method to Solve Rate Equations

The rate equations (Eqn. 3.3-3.8) can be put in the following form using simple algebra:

$$f_1 = \frac{A_{21}N_2 + W_{21}N_2 + C_{UP2}N_2^2 + C_{UP3}N_3^2}{W_{12} + R_{13} + C_{14}N_4 + C_{CR}N_6} - N_1 \qquad \text{(A.1)}$$

$$f_2 = N_{erb} - N_1 - N_2 - N_3 - N_4 \qquad \text{(A.2)}$$

$$f_3 = \frac{A_{21}N_2 + W_{21}N_2 + 2C_{UP2}N_2^2 - 2C_{14}N_1N_4 - W_{12}N_1}{A_{32}} - N_3 \qquad \text{(A.3)}$$

$$f_4 = \frac{A_{32}N_3 - R_{13}N_1 + 2C_{UP3}N_3^2 - C_{CR}N_1N_6}{A_{43}} - N_4 \qquad \text{(A.4)}$$

$$f_5 = \frac{A_{65}N_6 + W_{65}N_6 + C_{CR}N_1N_6}{W_{56}} - N_5 \qquad \text{(A.5)}$$

$$f_6 = N_{yb} - N_5 - N_6 \qquad \text{(A.6)}$$

Assuming an approximate solution vector $(\overline{N_1}, \overline{N_2}, \ldots, \overline{N_6})$, each of the functions $f_1, f_2, \ldots, f_6$ can be expanded in a Taylor series as follows:

$$\begin{aligned} f_1(N_1, N_2, \ldots N_6) \cong {} & f_1(\overline{N_1}, \overline{N_2}, \ldots, \overline{N_6}) + \left(\frac{\partial f_1}{\partial N_1}\right)_{\overline{N_1}} \left(N_1 - \overline{N_1}\right) + \ldots \\ & + \left(\frac{\partial f_6}{\partial N_6}\right)_{\overline{N_6}} \left(N_6 - \overline{N_6}\right) \end{aligned} \qquad \text{(A.7)}$$

where the functions and partial derivatives on the right-hand side are evaluated using the initial approximation. Although the exact solutions are unknown, the initial approximation can be improved by an iterative procedure. For the exact solution vector $(N_1, N_1, \ldots N_6)$, the left-hand side of Eqn. A7 goes to zero. The following system of linear equations is thus generated by expanding A.1-A.6 along the lines of A.7:

$$\begin{bmatrix} \frac{\partial f_1}{\partial N_1} & \frac{\partial f_1}{\partial N_2} & \cdots & \frac{\partial f_1}{\partial N_6} \\ \frac{\partial f_2}{\partial N_1} & \frac{\partial f_2}{\partial N_2} & \cdots & \frac{\partial f_2}{\partial N_6} \\ \vdots & \vdots & & \vdots \\ \frac{\partial f_6}{\partial N_1} & \frac{\partial f_6}{\partial N_2} & \cdots & \frac{\partial f_6}{\partial N_6} \end{bmatrix} \begin{bmatrix} \Delta N_1 \\ \Delta N_2 \\ \vdots \\ \Delta N_6 \end{bmatrix} = \begin{bmatrix} -f_1 \\ -f_2 \\ \vdots \\ -f_6 \end{bmatrix} \tag{A.8}$$

where $\Delta N_i = \overline{\overline{N}}_i - \overline{N}_i$ and $\overline{\overline{N}}_i$ is the next approximation. The partial derivatives are:

$$\frac{\partial f_1}{\partial N_1} = \frac{\partial f_2}{\partial N_1} = \frac{\partial f_2}{\partial N_2} = \frac{\partial f_2}{\partial N_3} = \frac{\partial f_2}{\partial N_4} = \frac{\partial f_3}{\partial N_3} = \frac{\partial f_4}{\partial N_4} = \frac{\partial f_5}{\partial N_5} = \frac{\partial f_6}{\partial N_5} = \frac{\partial f_6}{\partial N_6} = -1$$

$$\frac{\partial f_1}{\partial N_5} = \frac{\partial f_2}{\partial N_5} = \frac{\partial f_2}{\partial N_6} = \frac{\partial f_3}{\partial N_5} = \frac{\partial f_3}{\partial N_6} = \frac{\partial f_4}{\partial N_2} = \frac{\partial f_4}{\partial N_5} = \frac{\partial f_5}{\partial N_2} = \frac{\partial f_5}{\partial N_3} = \frac{\partial f_5}{\partial N_4}$$

$$= \frac{\partial f_6}{\partial N_1} = \frac{\partial f_6}{\partial N_2} = \frac{\partial f_6}{\partial N_3} = \frac{\partial f_6}{\partial N_4} = 0$$

$$\frac{\partial f_1}{\partial N_2} = \frac{A_{21} + W_{21} + 2C_{UP2}N_2}{W_{12} + R_{13} + C_{14}N_4 + C_{CR}N_6}$$

$$\frac{\partial f_1}{\partial N_3} = \frac{2C_{UP3}N_3}{W_{12} + R_{13} + C_{14}N_4 + C_{CR}N_6}$$

$$\frac{\partial f_1}{\partial N_4} = \frac{-C_{14}\left[A_{21}N_2 + W_{21}N_2 + C_{UP2}N_2^2 + C_{UP3}N_3^2\right]}{\left[W_{12} + R_{13} + C_{14}N_4 + C_{CR}N_6\right]^2}$$

$$\frac{\partial f_1}{\partial N_6} = \frac{-C_{CR}\left[A_{21}N_2 + W_{21}N_2 + C_{UP2}N_2^2 + C_{UP3}N_3^2\right]}{\left[W_{12} + R_{13} + C_{14}N_4 + C_{CR}N_6\right]^2}$$

$$\frac{\partial f_3}{\partial N_1} = \frac{-W_{12} - 2C_{14}N_4}{A_{32}}$$

$$\frac{\partial f_3}{\partial N_2} = \frac{A_{21} + W_{21} + 4C_{UP2}N_2}{A_{32}}$$

$$\frac{\partial f_3}{\partial N_4} = \frac{-2C_{14}N_1}{A_{32}}$$

$$\frac{\partial f_4}{\partial N_1} = \frac{-R_{13} - 2C_{CR}N_6}{A_{43}}$$

$$\frac{\partial f_4}{\partial N_3} = \frac{A_{32} + 4C_{UP3}N_3}{A_{43}}$$

$$\frac{\partial f_4}{\partial N_6} = \frac{-C_{CR}N_1}{A_{43}}$$

$$\frac{\partial f_5}{\partial N_1} = \frac{C_{CR}N_6}{W_{56}}$$

$$\frac{\partial f_5}{\partial N_6} = \frac{A_{65} + W_{65} + C_{CR}N_1}{W_{56}}$$

Solving A.8 using Mathematica gives closed-form expressions for ΔN_i's that are needed to improve the initial guess. Since these expression are fairly lengthy, they are not reproduced here. After evaluating the ΔN_i's, the next approximation is made :

$$\overline{\overline{N_i}} = \overline{N_i} + \Delta N_i$$

This iterative process continues until $f_1, f_2, \ldots, f_6$ all fall below the specified convergence criterion ($\varepsilon = 10^{-12}$). The solutions were verified to be physically acceptable (i.e. negative population densities are clearly not physically acceptable). Since convergence characteristics are not clearly established for systems of non-linear equations, the algorithm was tested under different initial guesses and always found to converge to the same result.